NASA/TP-2003-211950

Vortex Flows at Supersonic Speeds

Richard M. Wood, Floyd J. Wilcox, Jr., Steven X. S. Bauer, and Jerry M. Allen
Langley Research Center, Hampton, Virginia

March 2003

The NASA STI Program Office . . . in Profile

Since its founding, NASA has been dedicated to the advancement of aeronautics and space science. The NASA Scientific and Technical Information (STI) Program Office plays a key part in helping NASA maintain this important role.

The NASA STI Program Office is operated by Langley Research Center, the lead center for NASA's scientific and technical information. The NASA STI Program Office provides access to the NASA STI Database, the largest collection of aeronautical and space science STI in the world. The Program Office is also NASA's institutional mechanism for disseminating the results of its research and development activities. These results are published by NASA in the NASA STI Report Series, which includes the following report types:

- TECHNICAL PUBLICATION. Reports of completed research or a major significant phase of research that present the results of NASA programs and include extensive data or theoretical analysis. Includes compilations of significant scientific and technical data and information deemed to be of continuing reference value. NASA counterpart of peer-reviewed formal professional papers, but having less stringent limitations on manuscript length and extent of graphic presentations.

- TECHNICAL MEMORANDUM. Scientific and technical findings that are preliminary or of specialized interest, e.g., quick release reports, working papers, and bibliographies that contain minimal annotation. Does not contain extensive analysis.

- CONTRACTOR REPORT. Scientific and technical findings by NASA-sponsored contractors and grantees.

- CONFERENCE PUBLICATION. Collected papers from scientific and technical conferences, symposia, seminars, or other meetings sponsored or co-sponsored by NASA.

- SPECIAL PUBLICATION. Scientific, technical, or historical information from NASA programs, projects, and missions, often concerned with subjects having substantial public interest.

TECHNICAL TRANSLATION. English-language translations of foreign scientific and technical material pertinent to NASA's mission.

Specialized services that complement the STI Program Office's diverse offerings include creating custom thesauri, building customized databases, organizing and publishing research results . . . even providing videos.

For more information about the NASA STI Program Office, see the following:

- Access the NASA STI Program Home Page at ***http://www.sti.nasa.gov***

- Email your question via the Internet to help@sti.nasa.gov

- Fax your question to the NASA STI Help Desk at (301) 621-0134

- Telephone the NASA STI Help Desk at (301) 621-0390

- Write to:
  NASA STI Help Desk
  NASA Center for AeroSpace Information
  7121 Standard Drive
  Hanover, MD 21076-1320

NASA/TP-2003-211950

Vortex Flows at Supersonic Speeds

Richard M. Wood, Floyd J. Wilcox, Jr., Steven X. S. Bauer, and Jerry M. Allen
Langley Research Center, Hampton, Virginia

National Aeronautics and
Space Administration

Langley Research Center
Hampton, Virginia 23681-2199

March 2003

Acknowledgments

The authors would like to thank Mr. Peter Covell and Dr. James Campbell of NASA LaRC for their contributions of photographic material used in this paper. Their assistance is greatly appreciated and is respectfully acknowledged.

The authors would also like to thank the research and technical staff assigned to and those who supported the research conducted at the NASA LaRC UPWT from 1970 to 1990. Their professionalism and support are greatly appreciated and are respectfully acknowledged.

Available from:

NASA Center for AeroSpace Information (CASI)
7121 Standard Drive
Hanover, MD 21076-1320
(301) 621-0390

National Technical Information Service (NTIS)
5285 Port Royal Road
Springfield, VA 22161-2171
(703) 605-6000

Contents

Abstract 1
Introduction 1
Nomenclature 2
Background and History 3
High-Speed Wing and Wing-Body Vortex Flows 4
Flow Classification 5
High-Speed Missile Vortex Flows 5
Other High-Speed Vortex Flows 6
Low-Speed Vortex Flows 6
Recent Supersonic Research at Langley Research Center 6
Resultant Vortex Structures 6
Flat Plates and Cavities 7
General Description of Cavity Flow Fields 7
Flow Visualization of Cavity Flow Fields 8
Surface Flows on Cavity Floor 8
Off-Surface Cavity Flow Fields 10
Bodies and Missiles 12
Axisymmetric Body 12
Nonaxisymmetric Body 13
Wings and Aircraft 14
Sharp Leading-Edge Wings 14
Interfering Vortex Structures 15
Blunt Leading-Edge Wings 15
Multibody Aircraft 16
Designed Vortex Structures 17
Fundamental Aerodynamic Characteristics of Delta Wings 17
Vortex Flow Characteristics of Delta Wings 18
Zero-Thick Wings 18
Thick Wings 19
Cambered Wings 20
Wing Design 22
Design Philosophy 22
Design Observations 23
Design Approach 23
Design Results 24
Concluding Remarks 24
References 25
Tables 34
Figures 39

Abstract

A review of research conducted at the National Aeronautics and Space Administration (NASA) Langley Research Center (LaRC) into high-speed vortex flows during the 1970s, 1980s, and 1990s is presented. The data are for flat plates, cavities, bodies, missiles, wings, and aircraft with Mach numbers of 1.5 to 4.6. Data are presented to show the types of vortex structures that occur at supersonic speeds and the impact of these flow structures on vehicle performance and control. The data show the presence of both small- and large-scale vortex structures for a variety of vehicles, from missiles to transports. For cavities, the data show very complex multiple vortex structures exist at all combinations of cavity depth-to-length ratios and Mach numbers. The data for missiles show the existence of very strong interference effects between body and/or fin vortices. Data are shown that highlight the effect of leading-edge sweep, leading-edge bluntness, wing thickness, location of maximum thickness, and camber on the aerodynamics of and flow over delta wings. Finally, a discussion of a design approach for wings that use vortex flows for improved aerodynamic performance at supersonic speeds is presented.

Introduction

After a half century of high-speed vortex flow research there still exists a need for a thorough understanding as well as an efficient prediction capability of three-dimensional separated flows (vortex) at supersonic speeds. The extensive amount of previous research has contributed greatly to understanding these complex flow structures; however, in order to support the design of future aerospace vehicles, which is the primary aim of aerodynamics according to Kucheman 1978 (ref. 1), design guidelines and tools must be available.

Research remains focused on the same three vehicle types as that which guided previous efforts in the 1960s and 1970s. These vehicles are supersonic cruise aircraft (ref. 2), missiles (ref. 3), and reentry/blunt bodies (ref. 3). In addition to the similarity in vehicle focus, there is also great similarity in the design approach used for each vehicle type. In fact, many of the present designs are derivatives of the preferred shapes from the 1960s and 1970s. Despite significant focus by the research community on the vortex flow for these vehicles, the design approach has remained focused on maximizing attached flow at all flight conditions. The design philosophy continues to only grudgingly accept separated flows (vortex), with an assumed penalty, at off-design conditions. It is clear from recent design efforts that we have yet to step out of the design assumptions and constraints of the 1960s in order to explore new design concepts that exploit vortex flows for improved aerodynamics.

Research into vortex flows at supersonic speeds began in the 1940s with the initial research effort being directed toward simple bodies and wings (refs. 4–29). This work was an effort to support the exploration of supersonic flight for rockets, missiles, and aircraft, such as the X-15 (ref. 30). In the late 1950s and early 1960s, the study of hypersonic reentry vehicles began to contribute to the body of knowledge in high-speed vortex flows (ref. 31); as a result, the envelope of research was extended well into the hypersonic regime. By the 1970s, there was a significant research effort within the United States aerospace community that focused toward aerothermodynamic issues, such as those related to the lee-side vortex flows on the Space Shuttle (refs. 30 and 31). Also, in the 1960s and 1970s, there was a renewed focus on leading-edge vortex shedding on slender vehicles configured for supersonic cruise flight. This research was conducted at a similar level of urgency in both the United States and Europe due to the desire to develop the first commercially viable supersonic civil transport

aircraft (ref. 30). The 1980s brought a refocus on the aerothermodynamics of hypersonic flight with the National Aero-Space Plane (NASP) Program (ref. 30). The late 1980s and the 1990s again brought focus on supersonic flight with the High-Speed Research (HSR) Program (ref. 2). In the 1990s, there was also a renewed interest in hypersonic lifting bodies as evident by the new series of X planes (ref. 31). In addition to these research activities, there has also been significant effort directed toward supersonic military aircraft and missiles. Examples of these vehicles include the century series fighters, SR-71, as well as all present day fighters and missiles (ref. 30).

This paper focuses on vortex structures as they relate to aerospace vehicle design. Specifically, this paper reviews the research conducted into high-speed vortex flows during the 1970s, 1980s, and 1990s at the National Aeronautics and Space Administration (NASA) Langley Research Center (LaRC). During this time period, there was a significant effort to improve the aerodynamics of a variety of vehicles: the research community at NASA LaRC explored the off-body flow field of aerospace vehicles at supersonic speeds. These investigations made extensive use of on-body and off-body flow visualization test techniques and as a result the majority of the data presented in this paper is primarily comprised of qualitative visualization information. This paper shows both published and unpublished experimental data for flat plates, cavities, bodies, missiles, wings, and aircraft. However, in order to place NASA LaRC's recent high-speed research into perspective, the first section of the paper provides a historical review of the extensive body of high-speed vortex flow research from the 1940s to the present. Also presented in this initial section is a brief review of the low-speed vortex flow research at NASA LaRC in the 1960s and 1970s (ref. 32).

Nomenclature

AR	wing aspect ratio, b^2/S
b	wing span, in.
c	wing reference chord, in.
C_D	drag coefficient, Drag/qS
C_L	lift coefficient, Lift/qS
$C_{L,\alpha}$	lift-curve slope at 0° angle of attack
C_l	rolling moment coefficient, Rolling moment/qSb
C_m	pitching moment coefficient, Pitching moment/qSc
C_N	normal force coefficient, Normal force/qS
C_{NF}	missile fin normal force coefficient
C_p	surface static pressure coefficient
CFD	computational fluid dynamics
DVS	design vortex structure
d	missile body diameter, in.
HSR	high-speed research
h	cavity reference height, in.
L	reference length or cavity length, in.
LaRC	Langley Research Center
L/D	lift-drag ratio
LE	leading edge
LEX	leading-edge extension
L/h	length-to-height ratio
M	Mach number
M_N	component of Mach number normal to wing leading edge, $M \cos \Lambda_{LE} (1 + \sin^2 \alpha \tan^2 \Lambda_{LE})^{1/2}$
M_∞	free-stream Mach number
NASA	National Aeronautics and Space Administration
NASP	National Aero-Space Plane
NFW	natural flow wing
psfa	pounds per square foot, absolute

R	Reynolds number
RVS	resultant vortex structure
rpm	revolutions per minute
S	reference area, in^2 (= wing planform area for wings and aircraft, = body cross sectional area for missiles)
trap	trapezoidal
UPWT	Unitary Plan Wind Tunnel
U_∞	free-stream velocity, ft/sec
w	cavity width, in.
x	axial distance, in.
y	span distance, in.
y_v	spanwise position of vortex core, in.
z	vertical distance, in.
α	angle of attack, deg
α_N	angle of attack normal to wing leading edge, $\tan^{-1}(\tan\alpha/\cos\Lambda_{LE})$
β	Mach number parameter, $(M^2 - 1)^{1/2}$
δ	fin deflection angle, positive leading edge up, deg
δ_F	wing leading-edge flap deflection, positive leading edge down, deg
δ_{ROLL}	differential canard deflection angle, (port canard deflection angle) - (starboard canard deflection angle), deg
η	local semispan position, y/(b/2)
η_V	vortex action line, $y_v/(b/2)$
Λ, Λ_{LE}	wing leading-edge sweep angle, deg
ϕ	roll angle, deg
°F	degree Fahrenheit

Background and History

Within nature many mechanisms exist that ensure our environment consists of smooth and continuous fields of fluid and energy. These naturally occurring flow-control mechanisms exist at all scales and in all fluid and energy media. An example of these mechanisms is an expansion fan in a high-speed fluid flow that is analogous to the diffraction of energy at a physical discontinuity for an electromagnetic energy wave. For fluids, one of the most dramatic and powerful mechanisms is the vortex. The vortex is also one of the most consistently occurring fluid flow features in nature.

A vortex is created whenever a moving fluid encounters an abrupt discontinuity or whenever a stationary fluid is abruptly impacted by a moving boundary. This discontinuity or boundary may take the form of a physical surface, interacting fluids, or an abrupt gradient (temperature, velocity, pressure, density, or other flow parameter) in the parent fluid. Whatever the cause, the resulting flow feature is a coherent, viscous structure within the parent body of fluid in which the fluid elements have angular velocities with orientations that vary over 360°. Though simple in definition, the vortex can be a contradiction in its existence. When a vortex is formed, it can be powerful, benign, stable, unstable, and forgiving. All vortex structures have the unique capability to add energy to the local flow; they can also serve as a dividing boundary between two regions of dissimilar structured flow. The vortex may be thought of as nature's flow-control device because of its ability to reduce or eliminate large flow fluctuations, flow gradients, and flow separations.

Vortices may be both naturally occurring or man-made. Naturally occurring vortex structures are observed within the universe in the form of a spiral galaxy (fig. 1), on other planets as evident by Jupiter's Great Red Spot (fig. 2), and in a variety of very large-scale atmospheric structures on Earth such as hurricanes and tornadoes (fig. 3). Naturally forming vortex structures also exist as small-scale fluid structures such as an eddy that

may occur near a rock in a brook or in the wake of an oar. Large eddies or whirlpools are seen in a fast moving river rapid and the famous "Maelstrom Whirlpool" off the Lofoten Islands, Norway. Nature has also managed to integrate vortex flows into the life of various living things. These vortex structures enhance the flight performance of birds and insects and the swimming performance of fish and mammals. However, the one common characteristic in each of these natural vortex structures is that they are all low-speed flows (i.e., velocities below the speed of sound).

Man-made vortex structures can exist as both low-speed and high-speed phenomena, where high speed is defined as velocities greater than the speed of sound. Man-made vortex structures may also be divided into two categories: (1) those resulting from man's interaction with the environment—we shall refer to these as a resultant vortex structure (RVS), and (2) those that are designed to perform a prescribed function by man—we shall refer to these as a design vortex structure (DVS). Common RVSs are the whirlpool in your sink and the tip vortex from the wing of an aircraft, as seen in figure 4 (ref. 33). These two RVSs can be contrasted with common DVSs such as the whirlpool in your toilet bowl and the new generation of cyclone-type vacuum cleaners on the market today. Engineers have used DVSs to perform a variety of functions from particle separation (ref. 34) to correcting aircraft flight stability and control issues for military fighter aircraft at low speed and high angles of attack (refs. 32, 35, and 36).

The previous discussion reviewed the diverse vortex structures used by man and those that occur in nature. One of the most diverse environments in which vortex structures are observed is within the aerospace community wherein a single aerospace vehicle may have low-speed, high-speed, resultant, and design vortex structures. A review of the literature shows that the diversity in observed vortex structures on aerospace vehicles is independent of vehicle flight speed. To focus the discussion, the remainder of this paper concentrates on man-made vortex structures occurring about aircraft at high speed (supersonic). Not discussed are hypersonic flows and associated aerothermodynamic effects. Also note that data and flow visualization images presented within the paper are all time averaged (i.e., steady state).

To assist the reader in interpreting the information presented, a cross-reference between the references cited in the paper and the associated figures is contained in table 1.

High-Speed Wing and Wing-Body Vortex Flows

Vortex flows at supersonic speeds have been studied for over half a century by many recognizable aerodynamicists including: Jones 1947a (ref. 4), 1947b (ref. 5); Stanbrook 1959 (ref. 37); Squire 1960 (ref. 38); Stanbrook and Squire 1964 (ref. 39); Kucheman 1962 (ref. 40), 1971 (ref. 41), 1965 (ref. 42), 1978 (ref. 1); von Karman 1962 (ref. 43); Squire 1967 (ref. 44), 1976 (ref. 45), 1963 (ref. 46), 1976 (ref. 47); Peake and Tobak 1982 (ref. 48), 1980 (ref. 49); Tobak and Peake 1982 (ref. 50). While most of the early investigations were motivated by the design of efficient supersonic vehicles (refs. 51–97), it is interesting to note that, with the exception of Maskell (ref. 25) and Kucheman (ref. 1), vortex flows were not viewed as desirable flow types but a resultant phenomenon that must be managed at off-design conditions. Both Kucheman and Maskell recognized that the separated vortex flow about a slender aircraft satisfies all of the necessary requirements and criteria for efficient aircraft design (ref. 1).

The historical body of data for wings and bodies is immense and covers a broad range of geometries and flow conditions. Summary discussions of most of these data are presented in references 35, 48, 49, and 98–101. A review of these data shows that all man-made vortex structures related to aircraft fall into two broad classes as discussed by Smith in 1975 (ref. 102). The first class is sharp-edge separations, such as that from a sharp forebody chine or sharp leading edge of a swept wing, as in figure 5. The second general class is associated with smooth-wall vortex

structure, such as that from an axisymmetric body at high angle of attack (fig. 6). The smooth-wall type also includes the vortex structures emanating from wing-body junctures and other smooth-wall protuberances. Note the separation patterns presented in figures 5 and 6 as reflecting the conical nature of vortex separation at supersonic speeds.

The sketch shown in figure 5 is for a thin, sharp-edged delta wing at angle of attack. A review of the sharp-edge separation sketch shows that the secondary vortex structures are smooth-wall separation types. As noted in the figure, the primary separation line is at the sharp leading edge of the wing with a primary reattachment line located along a straight line that emanates from the apex and lies inboard of the wing leading edge. Inboard of the primary reattachment line the flow direction on the surface is streamwise while outboard of the primary reattachment line the flow is spanwise. The spanwise flow is accelerated under the primary vortex and then undergoes an abrupt recompression and eventual smooth-wall type separation, then forms the secondary vortex. As shown in the figure, this smooth-wall separation point is labeled the secondary separation line. Outboard of the smooth-wall vortex is a secondary reattachment line. This pattern of smooth-wall vortex and flow reattachment has been observed to repeat itself outboard of the secondary vortex and result in a tertiary smooth-wall vortex.

The sketch in figure 6 is for a slender cone (smooth wall) at angle of attack and shows that a smooth-wall vortex is generated from a shock-boundary layer interaction. The sketch in figure 6 shows that all separations, including secondary and tertiary vortex flows, are of the smooth-wall type. For the situation depicted in figure 6, the smooth-wall vortex results from the flow on the windward side of the body expanding around the sides to the leeward side of the body and eventually recompressing and turning streamwise. As the angle of attack is increased, the recompression becomes more abrupt; a shock is formed and the flow separates and forms a vortex. This is the primary separation line. Inboard of the primary separation line is the primary reattachment line. The resultant surface flow directions and secondary separation characteristics are similar to the sharp-edge separation discussed previously. Additional detailed discussions and explanations of these two flow separation types are found in numerous reports (see refs. 49 and 50).

Flow Classification

An area of particular interest that has received much focus over the past 30 years is in the classification of vortex flows on the lee side of delta wings. Several of the first efforts were by Lee in 1955 (ref. 8), Squire (ref. 38), Sutton (ref. 103), and Hall and Rogers (ref. 20) in 1960. Squire's research in 1960 (ref. 38) is very noteworthy in that he was able to define the boundary between attached and separated flow as a function of Mach number and angle of attack (see fig. 7). Additional classification work has been reported by Squire, Jones, and Stanbrook in 1963 (ref. 47); Squire in 1976 (ref. 45); Szodruch in 1978 (ref. 104); and Szodruch and Peake in 1980 (ref. 105). With each subsequent effort, there were additional flow types defined as shown in figure 8. In the 1980s, the work of Miller and Wood in 1984 (ref. 106) and Wood in 1985 (refs. 107–109) and 1987 (ref. 110), as depicted in figure 9, connected and refined the various boundaries. In 1987, Ganzer (ref. 111)—and in 1989, Covell (ref. 112)—extended the flow classification boundaries of Miller and Wood on the lee side of delta wings to higher angles of attack and Mach numbers. Additional discussion and detail of the flow classification efforts at LaRC are presented later in this paper.

High-Speed Missile Vortex Flows

The high-speed vortex flow research related to missiles has been focused on developing an understanding of the interference effects between body and fins. This focus was driven by the need to eliminate uncertainty in the control laws and flight characteristics. Early missile research focused primarily on isolated axisymmetric

bodies, such as Allen in 1951 (ref. 21) and Rogers in 1952 (ref. 27), in which there were one or two pairs of vortex structures. In the 1960s and 1970s, nonaxisymmetric bodies with a limited number of fins were investigated (refs. 113, 114, and 115); these concepts would have three or four pairs of vortex structures. By the 1980s, vortex-flow research for missiles investigated both axisymmetric and nonaxisymmetric bodies with five to six pairs of vortex structures. Examples of these studies are the work of Allen in 1979 and 1983 (refs. 116 and 117).

Other High-Speed Vortex Flows

With the exception of a laminar boundary layer, vortex structures exist in most flow fields. This is especially true for aircraft at high speeds. A brief review of the literature shows that in addition to the investigation of large-scale vortex structures there has also been a wide variety of research into much smaller scale structures. An example of these efforts includes research of boundary layer instabilities (ref. 18), vortex generators (refs. 118, 119, and 120), and wing-body juncture flows (refs. 37 and 121). Research has also been conducted on vortex breakdown (ref. 122), vortex flow asymmetry (ref. 123), and vortex/shock interaction (refs. 124 and 125) at supersonic speeds.

Low-Speed Vortex Flows

Over the same time period the high-speed research was performed, there was an equal number of investigations into low-speed vortex flows. The main difference between the two research efforts is that a primary focus of the low-speed research has been in the use of vortex flows to improve aerodynamic performance (ref. 32). The low-speed community focused on the use of vortex flow to improve the low-speed aerodynamic efficiency of slender aircraft and lifting-body vehicles as well as to improve the maneuverability of fighters at high angles of attack (ref. 35). There have been a number of documents summarizing the low-speed vortex flow and separated-flow research efforts from the 1950s to 1980s (see refs. 49, 50, and 126–128).

Recent Supersonic Research at Langley Research Center

From 1970 to the 1990s, researchers at LaRC were actively involved in the experimental study of vortex structures at supersonic speeds as a means to improve vehicle performance and maneuverability (refs. 129–148). This section of the paper summarizes the body of work at LaRC with a view toward vehicle design and flow control. A review of the types of resultant and designed vortex structures at supersonic speeds will be presented as well as a discussion on the benefits of these flow structures to vehicle performance. The information presented will cover small- and large-scale structures for a variety of vehicles from missiles to transports. The paper presents an extensive amount of flow visualization data with some supporting pressure data and force and moment results. The data to be presented have been obtained in the LaRC Unitary Plan Wind Tunnel (UPWT), which is a continuous flow, variable pressure, supersonic wind tunnel. The tunnel contains two test sections that are approximately 4 ft square and 7 ft long. Each test section covers only part of the Mach number range of the tunnel. The nozzle ahead of each test section consists of an asymmetric sliding block that allows continuous Mach number variation during tunnel operations from 1.5 to 2.9 in the low Mach number test section (#1) and from 2.3 to 4.6 in the high Mach number test section (#2). A complete description of the facility can be found in reference 149.

Resultant Vortex Structures

The research emphasis at LaRC during this time period has been on developing a thorough understanding not only of the aerodynamics of high-speed vehicles but also of the associated flow features and mechanisms that produce the resultant aerodynamics (refs. 129–138). In the 1970s and 1980s, the only tool available for these studies was the wind tunnel. Through the use of various test techniques, the aerodynamicist could explore the aerodynamics and fluid dynamics of aerodynamic concepts and components. In the

1990s, computational methods have become contributors to the investigation of these flow fields (refs. 58, 64, 72, 76, 77, 95, 109, 122, and 123); however, the wind tunnel remains the primary exploratory tool.

Computational fluid dynamics (CFD) can be used to predict when a vortex will be generated and to track the vortex downstream (the velocity vector's direction, or spin, is maintained far downstream of the generation of the vortex); however, the vortex will dissipate very rapidly unless a great deal of care is used to adapt the volume grid to cluster points in the vicinity of the vortex. Therefore, CFD should be used as a qualitative tool for tracking vortices and can only be used as a quantitative tool near the vortex generation point.

The efforts to understand fluid dynamics as well as aerodynamics have been driven by the need for additional types of data to support the development of advanced computational tools. At times the efforts have been driven by the development of advanced computational tools in order to support specific design and analysis needs.

As mentioned previously, the flow about any vehicle will usually contain one or more resultant vortex structures that may or may not contribute to the resultant aerodynamics. However, through the routine use of various flow visualization techniques to explore the flow fields, an improved understanding of vortex flow physics and interfering flow fields has been developed. As a result, the aerodynamic community is better equipped to both routinely account for the effects of vortex flows in the analysis of aerodynamic data and include vortex flow effects in the design process.

To provide insight into the diversity of vortex structures that are present at high speed, reviews of typical resultant vortex structures about flat plates and cavities, bodies and missiles, and wings and aircraft are presented in the following sections. Flow visualization data will be the primary format, but where appropriate, pressure and force data are shown to reflect the impact of the vortex structure on the aerodynamic behavior of the vehicle.

Flat Plates and Cavities

Around 1980, LaRC began studying problems related to the carriage and release of weapons from aircraft at supersonic speeds. These studies were in support of the development of a supersonic cruise fighter aircraft. One of the early studies showed that the separation characteristics of a store exiting a cavity were primarily a result of the cavity flow field (ref. 139). Because of the significant influence of the cavity flow field on the store separation characteristics, a series of studies were initiated to document the flow field inside cavities in order to better understand store separation characteristics. The results of these studies showed that even simple rectangular box cavities located in a flat plate have complicated three-dimensional flow fields containing multiple vortices. The remainder of this section describes some of the studies conducted at LaRC to understand cavity flow fields at supersonic speeds.

General Description of Cavity Flow Fields. Before describing the nature of vortex flows in cavities, it is sometimes helpful to describe the general nature of cavity flow fields. Numerous studies have been performed and reported in the literature that define the basic differences between the flow fields of shallow and deep cavities at supersonic speeds (refs. 140–147). These flow fields have been termed closed- and open-cavity flow and correspond to flows in shallow and deep cavities, respectively. The type of flow field that exists has been shown to depend primarily on the cavity length-to-height ratio (L/h). The flow field of cavities with $L/h \gtrsim 13$ is generally referred to as closed-cavity flow and is characterized by a flow that separates and expands over the cavity leading edge, impinges and attaches to the cavity floor, then separates and exits at the rear of the cavity (see fig. 10). The corresponding pressure distribution shows a decrease in pressure at the forward section of the cavity as the flow separates and expands into the cavity, an increase in pressure as the flow impinges on the cavity floor, a pressure plateau as the flow passes along the

cavity floor, and an increase in pressure as the flow exits ahead of the rear face. For cavities with L/h $\lesssim$ 10, the flow field is generally referred to as open-cavity flow and is characterized by a flow that passes over the cavity without any appreciable expansion into the cavity (see fig. 10). Typical pressure distributions show a slight positive pressure coefficient over most of the cavity floor with a slight increase in pressure at the rear of the cavity caused by flow impingement at the top of the cavity rear face. Cavities with open flow typically have flow-induced pressure oscillations. This aeroacoustic effect can produce tones severe enough to cause damage to the aircraft structure, store structure, or electronic equipment.

Cavity flows that exist in the region between open- and closed-cavity flow (10 $\lesssim$ L/h $\lesssim$ 13) are generally referred to as transitional cavity flows. Transitional cavity flow can be divided into two separate types of flow: transitional closed and transitional open. If the L/h of a cavity with closed flow is decreased, eventually the impingement shock and exit shock will collapse and form a single shock wave. The corresponding pressure distribution shows a low-pressure region at the forward section of the cavity as the flow separates and expands into the cavity with a steady increase in pressure toward the rear of the cavity. This type of flow field is referred to as transitional closed flow (see fig. 10). As the L/h of the cavity is reduced still further, the high-pressure region at the rear of the cavity vents to the low-pressure region at the forward section of the cavity, then abruptly switches the flow field so that the single shock wave present for transitional closed flow vanishes, thereby indicating that the flow does not impinge on the cavity floor. For this case, the flow is turned through a series of expansion and compression waves and the flow field is referred to as transitional open-cavity flow (see fig. 10). The pressure distribution generally shows a slight negative pressure coefficient at the forward section of the cavity, which indicates that the flow is partially expanding into the cavity; the pressure then increases steadily toward the rear of the cavity but does not reach as high a peak at the rear of the cavity as the transitional closed-flow case. It should be emphasized that the L/h values used above to describe the various flow fields are only general guidelines for estimating the type of flow field that exists for a given cavity. Because pressure distributions in the cavity are used to define the cavity flow fields, they are one of the best methods for determining the type of flow field that exists in a given cavity.

Flow Visualization of Cavity Flow Fields. Various types of flow visualization have been used to document the surface flow and off-surface flow fields of cavities. These techniques include schlieren, vapor screen, oil flow, and colored water flow.

The results describing the surface flow fields of cavities using a colored-water technique and those describing the off-surface flow fields using a vapor-screen technique are discussed in this section.

Surface Flows on Cavity Floor. During one cavity flow-field test, water was injected through pressure measurement orifices located on the model surface in an attempt to visualize vortices that typically form above certain cavity configurations. Because of the low static pressure in the tunnel, it was anticipated that the water would vaporize as it exited the orifice and the resulting vapor would be entrained into the vortices and render them visible. This technique did not work, and the water instead flowed along the model surface. Although the water was difficult to discern against the model surface, it was obvious that the water was being entrained by the model surface flows and had a fast response to the cavity flow unsteadiness. This impetus led to the development of a technique that uses colored water as a medium to visualize surface flows over wind tunnel models (ref. 148).

The colored-water surface-flow visualization technique basically involves injecting colored water through the pressure measurement orifice tubes installed in a wind tunnel model. The colored water exits the orifices and flows along the model surface to form streaklines. The resulting flow patterns are then photographed. For the test

data presented, colored water was injected through pressure orifices located along the floor of the cavity and on the flat plate surface ahead of the cavity.

The wind tunnel model used in this investigation (fig. 11) consisted of a rectangular box cavity mounted in a flat plate. The rear face of the cavity was attached to a remotely controlled electrical drive mechanism that allowed the rear face to move and thus vary the length of the cavity while the tunnel was in operation. The cavity height (h) and width (w) were 0.5 in. and 2.5 in., respectively, and were held constant throughout the entire test while the cavity length (L) was varied from 12 in. to approximately 0.5 in. The cavity leading edge was 10.4 in. aft of the flat plate leading edge. The boundary layer on the plate was turbulent, having been tripped at the plate leading edge with sand grit. All of the tests were conducted with the cavity at an angle of attack and sideslip of 0°.

The test results presented in this section of the paper were conducted at the conditions shown in table 2 in the low Mach number test section of the UPWT (ref. 149). The model was vertically mounted in the wind tunnel to allow video and still photographic data to be obtained through the test section windows. Because the model was vertically mounted, gravity forces could influence the colored-water streaklines. However, results from the test showed that water injected on the flat plate surface flowed in essentially a straight line, thus indicating a negligible influence of gravity forces. The model was painted white for good contrast with the colored water and was illuminated with three flood lamps.

Shown in figure 12 is a series of photographs acquired as the cavity length was decreased at a Mach number of 1.50. Also included in figure 12 are sketches of the streaklines indicating the direction of flow. The free-stream flow is from left to right and the scale located on the flat plate above the cavity indicates the cavity length in inches. Colored water was injected from two orifices located on the flat plate ahead of the cavity and from three orifices located on the cavity floor approximately 3 in. aft of the forward face. For the cavity with L/h = 24.0 (closed flow), the streaklines on the flat plate surface curve into the forward section of the cavity and indicate that the flow is expanding into the low-pressure region. At the rear of the cavity, these streaklines curve away from the cavity as the flow exits from the high-pressure region. On the cavity floor, two vortices have formed ahead of the rear face as indicated by a merging of the center cavity floor streaklines with each of the two side cavity streaklines. Note, the water color for these streaklines (yellow—middle orifice, blue—outside orifices) was chosen so that as the streaklines merged to form vortices, a new color (green) was formed. The formation of new colors from the merging of flows greatly enhances the data analysis. The upper vortex has a counterclockwise rotation and the lower vortex has a clockwise rotation. As the cavity length is reduced from L/h = 24.0 to L/h ≈ 17, these vortices maintain the same rotation direction. At L/h ≈ 13, the vortices start to dissipate and begin to form in the opposite direction as indicated by the small amount of green water moving up the center of the cavity. The flow pattern on the floor of the cavity represents the starting point of these vortex structures. As the cavity length is reduced still further, but before the vortices can completely form in the opposite direction, the flow field rapidly switches from transitional closed to open flow (L/h ≈ 12); the streaklines on the cavity floor flow upstream and the streaklines on the flat plate surface do not curve into the cavity.

Shown in figure 13 is a set of photographs illustrating cavity surface flows at a Mach number of 2.16. The primary difference between the results at Mach 1.50 and 2.16 is in the details of the formation of the vortices at the rear of the cavity. For L/h = 24.0 (closed flow), the two vortices ahead of the rear face have the same rotation direction as the Mach 1.50 case. However, in contrast to the M_∞ = 1.50 case, some of the blue/green water has broken away from the vortices and entered the yellow colored water at the rear of the cavity, indicating that the vortices are starting to form in the opposite direction. As the cavity L/h is decreased to approximately 17, the

two vortices at the rear of the cavity have dissipated and two new vortices, that together span the entire cavity width, have formed. These two new vortices have rotation in the opposite direction to the original vortices. At an L/h of approximately 14, these two vortices cover nearly one half of the entire cavity floor. Decreasing the cavity length still further to an L/h of approximately 13, the flow rapidly switches from transitional closed to open flow and the blue and yellow water streaklines flow upstream. The flow reversal indicates that a large recirculation region exists inside the cavity for open flow.

Figure 14 shows a close-up of the rear portion of the cavity for L/h = 24.0 at both $M_\infty = 1.50$ and 2.16. These photographs illustrate the significant effect of Mach number on the cavity flow field. Yellow tinted water is being injected from an orifice located on the cavity floor 3.25 in. downstream of the cavity forward face and blue tinted water is being injected 0.50 in. forward of the rear cavity face. At both Mach numbers, the blue tinted water from the rearmost orifice flows upstream and merges with the yellow tinted centerline water flow before being entrained into the vortices at the edges of the cavity. The flow fields at these two conditions are very similar; the primary difference is the spreading of the centerline flow field at a cavity length between 9.5 and 10.0 in. At $M_\infty = 2.16$, the mixing of the yellow and blue water to form green occurs in a blunt curved area near the L = 9.75 in. point. In contrast, at $M_\infty = 1.50$, the mixing of the yellow and blue water occurs at a sharp point near L = 10.0 in. The spreading of the flow at M = 2.16 is the start of the vortices that eventually form in the opposite direction to the edge vortices as the cavity length is decreased.

Vortices can also form at the forward section of the cavity. Figure 15 shows colored-water surface flows at the forward section of the cavity at $M_\infty = 1.50$ for two different L/h values that are in the open-cavity flow region. For the L/h ≈ 10 case, blue tinted water was injected from an orifice on the cavity floor 1.75 in. aft of the forward face. The water flows upstream and forms two counterrotating vortices in the corners behind the cavity forward face. As the cavity length was decreased further to an L/h of approximately 2.2, the two counterrotating vortices have each split into two counterrotating vortices for a total of four vortices that span the cavity width. The blue tinted water for this case was injected 2 in. ahead of the cavity on the flat plate surface.

Figures 12–15 illustrate some of the complex vortical surface flows in cavities at supersonic speeds. Even though the exact cause or causes of these vortices are basically unknown, it is clear that their impact on cavity aerodynamics and store separation from the cavities can be significant.

Off-Surface Cavity Flow Fields. The vapor-screen technique has been used to visualize off-surface flows in cavities. This technique consists of injecting water into the tunnel circuit until a fog is formed in the test section. The fog is a result of the water vapor condensing as the static temperature of the air decreases in the expanding flow of the tunnel nozzle. A thin light sheet is passed across the test section illuminating the fog. Figure 16 shows a sketch of the vapor-screen apparatus as set up in the UPWT. Typically, the light sheet remains stationary while the model is traversed longitudinally through the light sheet. In recent years, a laser-based system generated the light sheet instead of a Mercury vapor lamp, which was used routinely in years past. Photographs of the fog and light sheet are recorded with a still camera located inside the test section or mounted on the tunnel access doors. A complete description of the vapor-screen technique used in the UPWT is presented in reference 150.

Two types of flow phenomena that can be visualized with the vapor-screen technique are shock waves and vortices. Shock waves are revealed by the variation of the illuminated light sheet intensity. Vortices are revealed by dark areas where no particulates exist to reflect light from the light sheet.

Shown in figure 17 are vapor-screen photographs illustrating both open- and closed-cavity flow (ref. 146). The model used for these

tests was a flat plate with a cavity mounted in the center of the plate and is similar to the plate used in the colored-water flow photographs shown in the previous section. The cavity was 12 in. long, 2.5 in. wide, and the height was 1.88 in. and 0.50 in. for the open- and closed-cavity flow cases, respectively. The photographs view the cavity from downstream of the model looking upstream. Four photographs are presented for each case at four longitudinal locations along the cavity length. For the open-cavity flow case (L/h = 6.4), no vortices or shock waves are visible along the entire length of the cavity. In contrast, at x = 6.0 in. for the closed-cavity flow case (L/h = 24.0), two well formed vortices have developed along the cavity edges. These vortices are a result of the flow expanding into the cavity at the cavity sharp leading edge and along the cavity sharp side edges just downstream of the forward cavity face. The colored-water flow photograph in figure 13 for L/h = 24.0 shows the red tinted water, which was injected on the flat plate surface ahead of the cavity, curving into the cavity, thus illustrating how the sharp-edge vortices actually develop. In addition to the edge vortices at x = 6.0 in., the impingement shock that forms as the flow impinges on the cavity floor can also be seen. At x = 12 in., which is at the cavity rear face, the two edge vortices are still present and both the impingement and exit shocks can be seen. Downstream of the cavity on the flat plate surface at x = 14 in., the edge vortices can still be seen although they are starting to dissipate. These vapor-screen photographs illustrate the complex three-dimensional flow field of cavities.

The vortices that form along the cavity sharp edges for closed flow, as shown in the vapor-screen photographs, can affect the pressure distributions on the cavity rear face. Shown in figure 18 are lateral pressure distributions across the rear face of a cavity at four L/h values (ref. 140). These data were obtained on the same flat plate used in the colored-water flow photographs. To vary the cavity L/h, the cavity length was varied while the cavity height remained constant. At an L/h of 24.0 and 16.0, the cavity flow field would have closed flow. The data for these two cases show significant lateral pressure gradients across the rear face. These pressure gradients are generally symmetrical about the cavity centerline with the peak pressures occurring off the cavity centerline. Reference 140 attributes these gradients to the impingement of the cavity-edge vortices on the rear face. In contrast, the data for L/h = 4.0 show a much reduced pressure level and smaller gradients than for the closed-flow cases. At L/h = 1.0, the lateral pressure gradients have essentially disappeared.

Vapor-screen photographs have also been obtained in a cavity with a generic ogive cylinder inside the cavity (ref. 151). The purpose of this test was to provide a database on a generic store separating from a generic weapons bay. Figure 19 shows a schematic of the model mounted in the UPWT test section. The cavity was located in a flat plate that was vertically mounted and spanned the entire test section from floor to ceiling. The cavity was 5.768 in. wide, 29.362 in. long, and 2.432 in. high. The store was mounted on the tunnel model support system, which has the capability to traverse the test section from side to side thereby moving the model into and out of the cavity. The store was 24.028 in. long and 1.20 in. in diameter with an ogive nose radius of 11.51 in. Figure 20 shows vapor-screen photographs of the cavity with and without doors at $M_\infty = 2.65$ with L/h = 12.07. For the case without doors, two well formed sharp-edge vortices can be seen at the cavity side edge. In addition, one of two smooth-wall vortices on the store can be seen. The vortices on the store are caused by the flow expanding into the cavity, which places the store in a localized upwash region. In other words, the store appears to be at an angle of attack. The second vapor-screen photograph shows the cavity with doors. The doors are opened parallel to the cavity sidewalls and are half as tall as the cavity width so that if they were closed the cavity would be covered. The results for this case are similar to the doors-off case except that the cavity side-edge vortices have been replaced by vortices emanating from the outer edges of the cavity door. The smooth-wall vortices on the store are also better defined than the no doors case. These vapor-screen photographs illustrate the resultant vortex

structures inside cavities that can have a significant influence on the separation characteristics of stores as they exit the cavity.

Bodies and Missiles

In this section of the paper, vortex patterns and their measured effects on the aerodynamics of bodies and missiles are examined. The vortex images shown here are from vapor-screen images taken at supersonic speeds from tests in the UPWT. The material presented starts with simple shapes and effects and transitions to more complex geometries and flow fields. All flow visualization data presented in this section have been obtained with the vapor-screen flow visualization technique discussed previously.

Axisymmetric Body. The vortex structures observed on bodies and missiles include both smooth-wall and sharp-edge separation on the bodies and sharp-edge separation on the missile fins. For the present discussion forward-body fins are labeled canards, mid-body fins are labeled wings, and aft-body fins are labeled tails.

Figure 21 shows a simple axisymmetric body with cruciform wings mounted in the UPWT high-speed test section. The flow-field images on this model were obtained in support of the study documented in reference 152. The model has been painted black to prevent reflection from the laser light sheet that was used to make the vortex images visible. Also shown in this figure are a ceiling-mounted still camera and a strut-mounted video camera that were used to record the vapor-screen images.

Tests on this model were performed with and without the wings attached. Figure 22 shows a composite of three vapor-screen images at different longitudinal stations on the body without wings. These data are for Mach 2.5 and 14° angle of attack. Two symmetric body (smooth-wall) vortices can be seen that originate on the nose and continue to grow down the length of the body. The feeding sheet, which permits these vortices to continue to grow, can also be seen.

Figure 23 shows this configuration with the wings attached at a roll angle of 0° (tails in + orientation) for the same test conditions as those of figure 22. Note that the horizontal wings break up the feeding sheet for the body vortices, which no longer continue to grow over the rest of the body. The horizontal wings themselves develop a vortex along the leading edge (sharp-edge separation) that becomes detached downstream of the wing trailing edge. Note that only the flow structures on the left-hand side of the model are visible because the vertical wings block the laser from illuminating the right-hand side of the model. The top and bottom (vertical) wings produce no vortices because they are not at incidence to the oncoming flow at this roll angle. The last image ($x/L = 0.96$) shows that at the base of the body there are two body vortices that appear smaller than those on the body alone. The reduced size of the body vortices is a result of their feeding sheet being cut by the wing. This image also shows two stronger sharp-edge vortices that originate from the horizontal wings.

Figure 24 shows data from a tail-body configuration similar to those shown in figure 23. The data illustrate the effects that the body vortices can have on the tail loads (ref. 153). This figure shows the measured normal force coefficient on a single tail as it is rolled from windward to leeward at three angles of attack. The Mach number is 2.0 and there are no tail deflections. The dotted circle highlights the region of force reversal due to these interfering vortex flows. Note that when the tail orientation approaches a roll angle of 180° at $\alpha = 20°$, the normal force on the tail becomes negative, that is, in the downward direction even though the configuration angle of attack is 20°. This force reversal effect occurs when the tail is rotated to a location that positions body vortices on the lower surface of the tail. This effect is not present in the $\alpha = 5°$ data because the body vortices are too weak at this angle of attack. Also, the effect is greatly reduced at $\alpha = 35°$ because the vortices have moved far enough away from the body that they have a smaller effect on the tails. These data emphasize the importance of designing the body

and tails to maximize positive vortex-interference effects.

Figure 25 shows a photograph of a variant of the Sidewinder missile model mounted in the UPWT low-speed test section. Data from this model are used to illustrate canard-tail vortex-interference effects that can occur even at low angles of attack. Figure 26 shows the rolling moment on this configuration for a −10° canard roll deflection (5° on each horizontal canard). Data are shown for several tail fin spans, including tail off. The Mach number is 2.5 and the configuration roll angle is 0° (ref. 154). For the tail-off case, the canard deflections produce a rolling moment coefficient on the entire configuration of about −1.1. For the tail-on case the data show that as tail span increases, the configuration rolling moment control authority decreases at low angles of attack and changes sign near $\alpha = 0°$ for the larger tails. (It should be noted that tail size C is close to the size of the current Sidewinder missile tail fins.) Thus, the canards produce both a downwash and an upwash as well as a vortex flow field that interacts with the tails at low angles of attack to produce a tail rolling moment opposite to that generated by the canards. For the larger tail sizes, the vortex-induced rolling moment negates the rolling moment input from the canards, and near $\alpha = 0°$, a small rolling moment in the opposite direction is produced.

The next three figures (figs. 27–29) show vapor-screen vortex images on a Sparrow missile model at Mach 2.36 with no wing or tail deflections. These images are taken from reference 116. Figure 27 shows the longitudinal vortex development on the configuration at $\alpha = 11.4°$ and a roll angle of 0°. This figure shows a vortex pattern similar to that seen on the missile model shown in figures 22 and 23. This pattern of vortex structure remains unchanged as the vortices flow aft over the tail fins. Figure 28 shows the effects of roll angle on this configuration. Vortices that were not present on the upper and lower (vertical) wings at a 0° roll angle show up as roll angle increases. The vortex pattern is asymmetric for $\phi = 22.5°$ but becomes symmetric again about the vertical plane at $\phi = 45°$. Now, however, vortices are visible from all four forward wings as well as from the body. Figure 29 shows the effects of angle of attack on the size of the vortices for this configuration at the base of the body at a roll angle of 0°. The vortices get larger with increasing angle of attack but move farther away from the body.

Figure 30 shows a cruciform canard-tail configuration somewhat similar to the Sidewinder missile variant shown earlier, except that the tail section of this configuration is mounted on bearings that are free to roll in response to the aerodynamic loads (ref. 155). Figure 31 shows the effects that the canard flow field has on this type of configuration. In this figure, the Mach number is 2.5, the roll angle of the fixed section of the model (ahead of the tail section) is 0°, and a roll deflection of 10° is input from the canards (5° on each horizontal canard). Three cases are shown: (1) the tail section is fixed in place in the + orientation (tails aligned with the canards), (2) the tail section is fixed in place in the x orientation (tails 45° offset from the canards), and (3) the tail section is free to roll. The canard flow field causes the free-to-roll tails to spin at about 1000 rpm at low angles of attack. This spin rate stays fairly constant with angle of attack until about $\alpha = 6°$, when it begins to decrease and stops at about $\alpha = 12°$. Note that for small angles of attack the configuration rolling moment for either of the fixed-tail configurations is very small, as was seen in the Sidewinder variant model shown earlier. For the free-to-roll tail configuration, however, the canard roll deflection remains effective and fairly constant with angle of attack. Note, moreover, that the rolling tail has very little effect on the configuration pitching moment. Thus, the free-to-roll tail produces the desired configuration rolling moment without reducing the longitudinal stability of the configuration.

Nonaxisymmetric Body. Figure 32 shows an elliptic body (with a major-to-minor axis ratio of 3) mounted in the UPWT high-speed test section (ref. 117). The data of figure 33 show vapor-screen vortex patterns obtained on this body along with sketches of the observed smooth-wall vortex structures at Mach 2.5, $\alpha = 20°$, and

roll angles of 0° and 45°. At $\phi = 0°$, the body vortices are symmetric and the feeding sheet forms at the side edge of the body. As shown on the right side of this figure, at $\phi = 45°$, the size of both vortices decreases with roll angle and the more windward feeding sheet moves close to the body surface. The more leeward vortex moves far away from the body. A review of the force data of reference 117 shows that these vortices increase the lifting efficiency of this elliptic body.

The elliptical configuration shown in figure 32 had a companion configuration with the same elliptical mid-body but transitioned from a blunt hemispherical nose into a circular base. Vapor-screen images of the vortex structures for this configuration are shown in figure 34. For a 0° roll angle, the smooth-wall vortices emanating from the side of the body are similar to those seen on the completely elliptical body with sharp nose. However, the data of figure 34 show the addition of a thin vertical smooth-wall separation (vortex) originating on the blunt nose and continuing down the leeward centerline of the body. At $\phi = 45°$, the side vortices shift in a similar way to that seen on the completely elliptical body but the thin vortex from the blunt nose remains perpendicular to the plane of the body. At the aft end of the body, the thin nose vortex actually attaches itself to the leeward side vortex feeding sheet.

Figure 35 shows vapor-screen photographs depicting vortex patterns on a chined forebody model at Mach 2.0 and 20° angle of attack. Also shown in the figure is a photograph of the model mounted in the UPWT low-speed test section (ref. 138). A review of the model photograph shows the existence of a metric break running circumferentially around the model at an x/L of 0.64. The portion of the model aft of the metric break was used to minimize base effects on the forebody flow field and forebody aerodynamics. The vortex structure shown in the figure is a result of a sharp-edge separation occurring at the chine. Note that the feeding sheet of the body vortices is seen to emanate from the chine edge of the body. It appears that the metric break disrupts the body vortex feeding sheet and a second smaller vortex begins to grow along the chine side edge downstream of the metric break.

Wings and Aircraft

A review of existing experimental data for wings and wing-body geometries, references 156–168, reveals that a wide array of vortex flow structures are present at both low- and high-lift conditions. To highlight the various types of vortex structures present on wings and wing-body geometries, as well as the effect of flow conditions, various data are presented in figures 36 through 45.

All of the data presented in figures 36 through 45 have been obtained in the UPWT over a Mach number range of 1.6 to 3.5. The observed structures are a combination of both sharp-edge flow separation type and smooth-wall flow separation type, see figures 5 and 6, respectively. The sharp-edge vortex types shown in the figures include leading-edge vortex formation from a sharp-edge wing, leading-edge extension (LEX) or strake, tip vortex formation from a wing or canard, and the vortex from a sharp wing-body juncture discontinuity. The various types of smooth-wall (shock-induced) separations, such as from the side of a slender body, on the lee side of a wing, and at a blended wing-body juncture region, contrast the sharp-edge separations.

Sharp Leading-Edge Wings. Presented in figures 36 and 37 are data obtained for variable leading-edge sweep (ogee) wings with sharp leading edges, references 158 and 165, respectively. Both of the concepts shown in figures 36 and 37 have been designed for efficient supersonic cruise and improved performance at lift coefficients above cruise. The data presented in figure 36 are for a highly cambered wing, with a leading-sweep angle that varies from 82.09° to 65.5°, at 5° angle of attack, and a Mach number of 2.4. The data presented in figure 37 are for a mildly cambered wing, with a leading-sweep angle that varies from 79.5° to 60°, a canard at 12° angle of attack, and a Mach number of 1.8.

As discussed in reference 158, the design objective for the wing shown in figure 36 was to employ wing camber to eliminate or delay wing leading-edge vortex formation to high-lift coefficients in order to improve high-lift performance.

Vapor-screen photographs of figure 36 show the simultaneous existence of both a smooth-wall vortex emanating from the very low sweep nose region of the highly cambered ogee wing and a sharp-edge leading-edge vortex. It may appear counterintuitive that a wing with a sharp leading-edge geometry will have a smooth-wall separation; however, the combination of very low sweep at the nose and a very high Mach number creates a flow condition rather similar to that which occurs for a blunt body. The flow at the apex remains attached as it expands around the sharp leading edge but then undergoes a rapid recompression that separates the flow. This sharp-edged vortex resides on the surface of the geometry and is also referred to as a leading-edge bubble.

A review of additional data from reference 158 shows similar vortex-flow features for a reference uncambered wing. The uncambered wing has the same vortex-flow structure as the cambered wing but has a 16-percent loss in aerodynamic performance compared with the cambered wing. The data of reference 158 show that these vortex structures are noninterfering phenomena that occur over a wide range of flow conditions. The similarity in vortex-flow characteristics for the cambered and uncambered wings supports the argument that the existence of vortex flow does not always degrade aerodynamic performance of cambered wings at supersonic speeds.

The design objective for the ogee wing shown in figure 37 was to employ the downwash from a canard to eliminate or delay wing leading-edge vortex formation in order to improve performance at cruise (C_L = 0.1). Similar to the observations from figure 36, the vapor-screen photographs of figure 37 also show the existence of two noninterfering vortex structures on the lee side of the wing. However, unlike the data of figure 36, these structures are both sharp-edge vortex structures that emanate from the canard tip and the wing leading edge. Despite the existence of these two vortex structures, the data of reference 165 show that the wing with canard has improved drag-due-to-lift characteristics at all lift conditions, in contrast to the wing without canard.

Shown in figure 38 are the lee-side vortex flow characteristics of another design study for a wing with canard (ref. 166). This study also attempted to use canard downwash to suppress vortex formation on the main wing in an effort to improve cruise performance (C_L = 0.1). The design study of reference 166 was performed on a 70°/20° sweep cranked arrow with a 55° swept canard for a Mach number of 1.8. Both the canard and wing had sharp leading edges. The photographs of figure 38 show the existence of two noninterfering vortex structures on the lee side of the wing. These structures are both sharp-edge vortex structures that emanate from the canard tip and the wing leading edge. Additional data of reference 166 show similar wing flow features were present on the wing without canard configuration. Despite the existence of these two vortex structures, the data of reference 166 show that the wing with canard has improved drag-due-to-lift characteristics at all lift conditions in contrast to the wing without canard.

Interfering Vortex Structures. Presented in figure 39 are data for a 70° swept delta wing with an 82.6° strake at an angle of attack of 10° and a Mach number of 3.5 (ref. 160). These data show the development of a smooth-wall vortex structure emanating from the forebody and a sharp-edge strake vortex structure. The data show the strake vortex structure completely enveloping the weaker forebody vortex prior to the start of the wing leading edge. The smooth-wall forebody vortex structure of figure 39 is relatively weak and thus it is easily dominated and consumed by the strake vortex structure. The significance of interacting vortex flows is a function of the downstream geometry of the subject vehicle; therefore, general conclusions cannot be drawn.

Blunt Leading-Edge Wings. Compared with the previously discussed vortex structures, the next three figures show relatively weak vortex structures that may exist on blunt leading-edge wings and wing-body geometries. The vortex structures presented in figures 40, 41, and 42 are primarily smooth-wall vortex flows resulting from wing lee-side shock-induced separation and wing-body juncture flows.

Depicted in figure 40 is a vapor-screen photograph for a cambered, blunt leading-edge 70°/66° cranked-arrow wing-body at an angle of attack of 10° and a Mach number of 1.8 (ref. 167). Also shown in the figure are the trimmed drag characteristics at Mach 1.8 for the cambered and a reference flat wing. The vapor-screen image for the cambered wing shows the presence of a shock-induced (smooth-wall) vortex structure residing at 50 percent of the local semispan. The drag data of figure 40 show that at this condition the cambered wing has improved performance compared with the uncambered wing. A review of additional aerodynamic and flow visualization data from reference 167 indicates that the separated vortex-flow structure on the wing does not degrade the aerodynamic performance.

Similar observations and conclusions, as those of figure 40, can be drawn from the information presented in figures 41 and 42 as well as the supporting data contained in references 157 and 161, respectively. Figure 41 shows results for a 55° swept delta wing-body with an uncambered blunt leading-edge wing at various lift coefficients and a Mach number of 2.16. At the higher lift coefficients, the data show the existence of a shock-induced vortex structure as well as a wing-body juncture vortex. The data of figure 42 also show that a shock-induced vortex structure is present for the 50° swept delta wing-body with an uncambered blunt leading-edge wing at 12° angle of attack at a Mach number of 1.6. Note, the wing-body juncture vortex structure observed in figure 41 is not present in figure 42 due to a combination of the lower Mach number and improved blending of the wing-body juncture. The aerodynamic data and additional flow visualization data of references 157 and 161 show that despite the existence of smooth-wall vortex structures both wings provide excellent aerodynamic performance.

Multibody Aircraft. The final two figures discussed in this section contain data taken from reference 162. These data are for a multibody concept employing a sharp leading-edge 65° delta wing outboard panel (fig. 43) and a multibody concept employing a 20° trapezoidal (trap) wing outboard panel with a sharp leading edge (fig. 44). The pair of axisymmetric bodies separates the outboard wing panels from a common 60° swept inboard wing panel with a sharp leading edge. The data of figures 43 and 44 are for an angle of attack of 16° at a Mach number of 2.16. The data presented in both figures show the existence of a very complex combination of shocks and flow separation. Sketches of the Schlieren shock patterns and oil-flow patterns are included in the figures to aid the reader in interpreting the complex flow features seen in the vapor-screen photographs. The flow separation structures of figures 43 and 44 consist of sharp-edge and smooth-wall vortex structures as well as nonvortex flow separation caused by shock-boundary layer interactions. The data of figure 43 show sharp-edge wing leading-edge vortex structures from both the inboard and outboard wing panels, a shock-induced vortex structure (which has merged with the inboard wing vortex), and a smooth-wall vortex structure emanating from each of the forebodies. The observed flow features for the 20° trap multibody concept (see fig. 44) are very similar to those observed for the 65° delta multibody concept (see fig. 43) with the exception of the outboard wing panel vortex structure. The data of figure 44 show the existence of a smooth-wall shock-induced vortex structure for the 20° swept wing. The data of figures 43 and 44 and additional results from reference 162 show that despite the numerous vortex structures that exist for these concepts, they have very good aerodynamic performance compared with existing single-body aircraft.

The data presented in figures 36 through 44 show that a wide variety of resultant vortex-flow structures can exist on vehicles at high speed. An assessment of these data with additional results from references 156, 159, 163, and 164 shows that despite the existence of vortex structures, aerodynamic performance is not degraded. Also note that the vortex structures discussed were observed to be steady and stable at all combinations of Mach number and angle of attack at which data were obtained.

Designed Vortex Structures

The design of efficient supersonic aircraft has historically focused on maintaining attached flow over the full vehicle under the assumption that attached flow (refs. 169–179) would produce optimum performance. The attached-flow design approach assumes that the flow will only separate at the trailing edge of the wing. However, it is well-known that for a vehicle in flight there are numerous vortex structures present. Examples of these structures are vortices that emanate from the wing tips, wing-body juncture, shock-boundary layer interaction, and vehicle base (rearward facing step). Each vortex structure listed is of the resultant type.

In the early 1980s, it was postulated that for slender geometries improved aerodynamic performance could be achieved at cruise through the use of a leading-edge vortex structure (refs. 176 and 179–181). It was further argued that the resulting geometry would be lighter and less complex than a highly twisted and cambered design. In an effort to address this goal, a parametric study was conducted on a family of delta wing models at Mach numbers from 1.6 to 4.6. The delta wing planform was selected because of the extensive historical data available for analysis and the ease in which simple and robust geometric and flow parameters can be used to extend these results to other geometries.

In this section, the effects that leading-edge sweep, leading-edge bluntness, wing thickness, location of maximum thickness, and camber have on the aerodynamics of and flow over delta wings are discussed and the methods for visualizing these flow fields are examined. The subsequent discussion first reviews and characterizes the aerodynamics (ref. 181) and then the flow fields for delta wings, such as separation bubble, classical vortex, and vortex with shock (refs. 106–112). This is ensued by a wing design discussion wherein the understanding of the character of the flow over such wings is highlighted.

Fundamental Aerodynamic Characteristics of Delta Wings

At supersonic speeds, the aerodynamics of delta wings has historically been correlated with parameters relating to the leading-edge flow condition and wing leading-edge sweep. These correlation parameters have typically been derived from linear theory and have not been based upon experimental observations.

To establish a point of reference for the subsequent discussion a brief review of several correlation parameters is presented. Figure 45 (ref. 181) graphically depicts the range of several of these parameters for the Mach number and wing leading-edge sweep discussed in this section. Figure 45(a) shows the variation in aspect ratio (A) of delta wings with the leading-sweep angle (Λ) and figure 45(b) illustrates the relationship between Mach number (M) and the leading-edge sweep parameter ($\beta \cot \Lambda$). Note that β is the supersonic Mach parameter $(M^2 - 1)^{1/2}$. A leading-edge sweep parameter value of 1.0 corresponds to a sonic leading-edge (LE) condition. Thus, a subsonic LE condition occurs for $\beta \cot \Lambda$ values < 1.0 and a supersonic LE condition for values > 1.0. A supersonic wing LE condition indicates that the flow normal to the wing leading edge is supersonic and based upon a two-dimensional airfoil analysis a large wave drag penalty would result. However, it is well-known that this wave drag penalty is never manifested on representative swept wings. This is because the notion of a subsonic and supersonic LE condition is not a description of the governing physics but a description of the relationship of the Mach angle to the wing leading-edge sweep angle. Despite the limitations and inherent restrictions of linear theory to model the aerodynamics of wings dominated by vortex flows, the parameters just discussed are still useful for the correlation of aerodynamic and flow-field observations at low angles of attack.

Presented in figure 46 (ref. 181) is the variation in lift-curve slope with $\beta \cot \Lambda$ for thin, thick,

sharp, and blunt delta wings. Presented in figure 46(a) are sketches of representative airfoils for the data presented in figures 46(b) and 46(c). The lift data of figure 46(b) are for sharp leading-edge wings that vary in thickness only. The data of figure 46(c) are for thin wings which vary in leading-edge bluntness only. The observed flow fields for the lift data presented in figures 46(b) and 46(c) vary from attached flow to sharp-edge vortex separation. Note that at supersonic speeds, the zero-lift lift-curve slope is typically maintained to lift coefficients greater than 0.30. Thus, the lift-curve slope is a direct indicator of the drag due to lift of these slender wings for low to moderate lift conditions. This linear behavior of wing supersonic lifting characteristics allows for an efficient assessment of the aerodynamics over a broad Mach and angle-of-attack range because the supersonic drag of a swept wing is inversely proportional to the lifting characteristics.

For reference purposes, linear theory estimates are presented in figures 46(b) and 46(c). These estimates are independent of wing thickness and leading-edge bluntness. Note that the data for all wings collapse to a narrow band at values of $\beta \cot \Lambda$ below 0.5. At these small values of $\beta \cot \Lambda$ (i.e., small disturbances) linear theory does an acceptable job of matching the experimental data. However, at higher values of $\beta \cot \Lambda$ linear theory overpredicts the lift-curve slope of thin, sharp leading-edge delta wings (see fig. 46(b)) but more closely matches the trends for blunt leading-edge (see fig. 46(c)) and thick delta wings (see fig. 46(b)). These data suggest that the aerodynamic performance of thin, slender wings at supersonic speeds and low $\beta \cot \Lambda$ is a function of Mach number and angle of attack but less sensitive to wing geometry and flow field.

Vortex Flow Characteristics of Delta Wings

As discussed previously, the supersonic flow over delta wings at angle of attack is dominated by nonlinear separated vortex flows. A review of existing data shows that the experimental studies of lee-side flow-field characteristics of delta wings have used the Mach number and angle of attack normal to the wing leading edge (ref. 38) as the primary correlation parameter. Unlike the $\beta \cot \Lambda$ parameter discussed above, the M_N and α_N parameters account for angle of attack as well as planform geometry in defining the flow conditions at the wing leading edge.

The next three sections discuss the flow over delta wings in supersonic flow fields. The first section describes the flow over zero-thickness wings. The two subsequent sections discuss the effect of thickness and camber on the flow structures over delta wings and how these can be used to design wings.

Zero-Thick Wings. The flow over flat, zero-thickness wings can be characterized as attached (both upper and lower surfaces) for an angle of attack of 0°. At angles of attack greater than 0°, these wings follow the classification pattern defined for lee-side flows in figure 47 (ref. 106). The flow structures represented in figure 47 are a combination of sharp-edge and smooth-wall vortex structures. Note the flow classification results depicted in figure 47 are the same as those presented in figure 9. The results from figure 9 are presented at this point in the paper to assist the reader.

The right side of the figure shows results for M_N greater than 1.0. For high values of M_N and low-lift (near $\alpha = 0°$) conditions (region 1), the value of the cross-flow velocity is low, thus subcritical with the primary flow in the streamwise direction. As lift increases, the flow turning angle about the leading edge increases, resulting in an increase in the magnitude of the inboard flow component. This inboard flow eventually recompresses and turns streamwise. As lift increases further, the cross-flow velocity increases to the point that a cross-flow shock occurs that turns the flow streamwise. The occurrence of a cross-flow shock is an indication of the existence of nonlinear supercritical-type cross flow. Further increases in lift result in shock-induced separation of the boundary layer and the formation of a smooth-wall separation (see region 2). Further increases in angle of attack show the shock-induced bubble/vortex migrating to the leading edge. With still further increases in angle of

attack this smooth-wall bubble/vortex structure transforms into a sharp-edge vortex as the feed sheet emanates from the sharp leading edge (see region 3). This structure eventually lifts off the surface and cross-flow shocks form (see region 4). These shocks may be located on the vortex upper surface, underneath the vortex, and horizontally between the two counterrotating pair of vortex structures. The vortex structure, which lies underneath the primary vortex structure, interacts with the boundary layer and results in a smooth-wall vortex (secondary) structure.

The left side of figure 47 shows results for M_N less than 1.0. For low values of M_N and low-lift (small angle of attack) conditions the flow that occurs on the lee side of a wing is a leading-edge separation characterized by a viscous, rotational mass of air that resides inboard of the wing leading edge. At low-lift conditions, a leading-edge bubble develops (see region 6). This bubble lifts off the wing surface and becomes a vortex with increasing angle of attack (see region 5). As angle of attack is increased further, a secondary vortex and then a vortex with a shock occur. The vortex body is connected to the wing surface via the feed sheet that is a viscous flow region emanating from the wing boundary layer near the wing leading edge. The shape and position of the viscous vortex system are dependent upon the flow field external to the vortex that interacts with the vortex system until an equilibrium condition is established. The vortex system acts as a physical boundary to the external flow field. The free-stream flow expands around the wing leading edge and follows the contour of the vortex system undergoing an expansion followed by a compression as the flow turns about the vortex. This "induced flow field," influenced by the viscous vortex system, is characterized by a stagnation point or reattachment line on the wing upper surface inboard of the vortex body. Inboard of this induced flow field is the potential flow field, where the flow is attached in the streamwise direction.

Example vapor-screen photographs for several types of complex vortex-flow structures depicted in figure 47 are discussed next. The specific M_N and α_N conditions for these data points are graphically depicted in figure 48 and the associated data for each of the conditions are presented in figures 49 and 50. Figure 49 contains a series of vapor-screen photographs on the zero-thickness, 75° delta wing model in the UPWT (ref. 112). The images in this figure represent conditions that are above and below $M_N = 1.0$, as depicted in figure 48. Three angles of attack are shown for Mach numbers 2.4, 3.4, and 4.6 (see figs. 49(a), 49(b), and 49(c), respectively). A review of the data of figure 49 shows a primary vortex only for the Mach 2.4, $\alpha = 8°$ and Mach 3.4, $\alpha = 8°$ conditions. At Mach 4.6 and $\alpha = 8°$ the data show the existence of a separation bubble with shock. The existence of primary vortex with shock, secondary vortex, and tertiary vortex structures is observed for Mach 2.4 and 3.4 at $\alpha = 16°$ and 24°. At Mach 4.6 and $\alpha = 16°$ and 24°, separation bubbles with shock that extend to the centerline of the model are observed. With the exception of Mach 2.4, $\alpha = 8°$ and Mach 3.4, $\alpha = 8°$, each image contains at least one cross-flow shock and for most of the images several cross-flow shock structures are present.

Figure 50 presents a series of vapor-screen photographs for a zero-thickness, 52.5° delta wing model in the UPWT (ref. 112). The images in this figure represent conditions that are above $M_N = 1.0$, as depicted in figure 48. Three angles of attack are shown for Mach numbers 2.4, 3.4, and 4.6 (see figs. 50(a), 50(b), and 50(c), respectively). The vapor-screen photographs of figure 50 show the existence of both smooth-wall separations (i.e., shock-boundary layer interaction) and sharp-edge separations. With the exception of the image for Mach 2.4 and $\alpha = 8°$, the data show the existence of leading-edge separation bubbles and/or vortices. These vortex structures are seen to increase in size and extend spanwise toward the centerline of the model with increases in angle of attack and Mach number. The flow fields shown contain at least one cross-flow shock structure and for most of the images several cross-flow shock structures are present.

Thick Wings. The effect of wing thickness on the wing leading-edge vortex position is shown in

figure 51 (ref. 181). The vortex action line shown in figure 51 is represented as a fraction of the local wing semispan. The vortex action line is the position at which the vortex-induced normal-force vector should be placed to give the same wing bending moment as that produced by the vortex pressure loading on the wing upper surface. The data clearly show an outboard movement of the vortex with the increasing of wing local surface slope at the leading edge. The thick-wing surface pressure data of figure 52 (ref. 181) also indicate that the wing upper leading-edge surface slope acts to delay the onset of flow separation at a higher angle of attack. At a constant angle of attack of 8°, the data of figures 51 and 52 show that increasing leading-edge surface slope results in a weaker vortex that is located farther outboard as compared with a lower leading-edge surface slope. The data indicate that wing leading-edge surface slope and not thickness is the dominant mechanism controlling vortex formation, strength, and position. Despite the noticeable effects on the lee-side flow characteristics among the three wings, a review of additional data contained in reference 181 shows that there were no noticeable changes on the total wing lifting characteristics.

A review of thick delta-wing lifting characteristics of figure 46 shows that for values of $\beta \cot \Lambda$ below 0.5, the lift-curve-slope data show insensitivity to thickness. The figure also shows that for values of $\beta \cot \Lambda$ above 0.5 there is an increase in the lift-curve slope over the flat, zero-thick delta data, but only a minor variation due to large changes in thickness. The data of figure 46 also indicate that the leading-edge radius affects the flow and resultant vortex formation the same as the leading-edge angle or thickness.

Figure 53 (ref. 138) shows oil-flow photographs on the lee side of three 60° delta wing models. The first is a flat-topped (zero-thick) wing, the second has a circular arc airfoil, and the third has a diamond airfoil. At 0° angle of attack, all three wings have attached flow. At 8° angle of attack, the circular arc and diamond airfoils have attached flow on the upper surface and the flat wing has a sharp-edge vortex separation. For the thick wings, there is a cross-flow component that flows inboard and normal to the leading-edge sweep. Inboard of the leading edge the cross flow is recompressed and turns streamwise. At 16°, all three wings have leading-edge separation (sharp-edge vortex). The location of the vortex action line for the flat wing occurs farther inboard than for the two thick wings, as was observed previously in figure 50.

Figure 54 (ref. 138) illustrates the effects leading-edge sweep and airfoil shape have on the lee-side flow characteristics of delta wings at M = 1.70 and 8° angle of attack. The six images in this figure include three 52.5° delta wing models and three 75° delta wing models, top and bottom rows, respectively. The figure also has three columns comparing a flat wing, a circular arc, and a diamond airfoil model (as was done in fig. 53). Once again, it is clearly evident that the flat wings have their vortex action lines occurring farther inboard than the thicker circular arc and diamond airfoil wings.

Finally, even at 0° angle of attack, a thick wing can have vortex flow. For example, figure 55 is an oil-flow photograph of a 75° delta with a diamond airfoil. The oil flow shows that the leading edge is attached; however, the flow downstream of the maximum thickness line has separated and has an oil-flow pattern similar to the oil-flow photographs seen for flat wings at angle of attack. Upon an initial review it is unclear if this separation is of the sharp-edge or smooth-wall type. However, a review of the predicted surface pressure coefficient plots shown at three x/L locations (0.6, 0.8, and 0.95) indicates that the flow expands over the ridge, then recompresses through a cross-flow shock. These pressure data clearly indicate that the separation mechanism is a smooth-wall type. The flow direction inboard of the shock is streamwise. This effect will also be seen in the next section when investigating the effects of camber.

Cambered Wings. After wing planform selection, the geometric parameter usually optimized during design of a supersonic aircraft is the camber and twist distribution. The next series of figures illustrate the effect of a camber (leading-edge

flap deflection) on the flow characteristics on the upper surface of a highly swept, sharp leading-edge delta wing at supersonic speeds. All of the data presented in this section were obtained on a 75° delta wing with deflectable leading-edge flaps. Photographs of the wind tunnel model installed in the UPWT are shown in figure 56 (ref. 110). The data obtained for this model are presented in figures 57 through 59. The data of figures 57 and 58 represent the two families of flow types found in the investigation documented in reference 110. The first family of data is termed "single-feature" flow type and is presented in figure 57. The second family of data is the "double-feature" flow type (see fig. 58). Single-feature flow types have only one major flow structure that emanates from either the leading edge or the flap hinge line. Double-feature flow types have two major flow structures: one emanating from the leading edge and one emanating from the flap hinge line. The data presented are vapor-screen images, surface pressure coefficient values, and flow-field sketches. To aid the reader in interpreting the complex flow features seen in the vapor-screen photographs of figures 57 and 58, sketches were created by tracing the negatives of the vapor-screen photographs.

Figure 57 (ref. 110) shows six sets of vapor-screen images, surface pressure coefficient values, and flow-field sketches of the 75° swept delta wings at various Mach numbers and angles of attack with a single flow feature.

The data are discussed from left to right and top to bottom, starting with the upper left figure. The effect of camber is modeled as a leading-edge flap deflection. The first image in figure 57 is for a 5° leading-edge flap, δ_F, setting at $M_\infty = 1.7$ and $\alpha = 0°$. The data show attached flow (i.e., no dark regions evident in the vapor-screen photograph and only a small negative pressure coefficient, C_p, located at the hinge line). The second image presented is for a change in α only to 6°. The data show a leading-edge bubble (i.e., a small dark region at the leading edge on the flap and a large region of negative C_p values that encompass the flap). The third image presented is for another change in α only to 12°. The data indicate the existence of a classical vortex with a feed sheet, secondary separation (bubble), and a shock located between the wing upper surface and the leading-edge vortex. The corresponding pressure distributions show that low pressures persist well inboard of the flap hinge line. The fourth image was taken for the same wing geometry but at a Mach number of 2.0 and an angle of attack of 16°. The data show a leading-edge vortex, a cross-flow shock (on top of the vortex), a secondary vortex on the hinge line, and a shock underneath the primary leading-edge vortex. The fifth image was obtained for a 10° leading-edge flap deflection angle at $M_\infty = 2.8$ and $\alpha = 0°$. The data show the existence of a hinge-line separation bubble (i.e., a small dark region on the wing inboard of the hinge line). The final image in this figure is a hinge-line vortex and was taken at $M_\infty = 2.4$ at an angle of attack of 6° for a 10° leading-edge flap deflection angle. The vapor-screen photograph indicates the hinge-line vortex by a circular dark region about halfway from the centerline to the hinge line. There is also evidence of a feed sheet on the photograph. The surface pressures indicate suction pressures inboard of the hinge line with negligible loads on the flap.

Figure 58 (ref. 110) shows six sets of double-feature flow types observed on the same 75° delta wing model. The first image is for a 5° leading-edge flap deflection at $M_\infty = 1.7$ and $\alpha = 5°$ and shows two separation bubbles, one located at the leading edge on the flap and the other at the hinge line. The surface C_p values show that the separation bubble located on the flap produces much lower values of C_p than the one at the hinge line. By increasing the flap angle to 10°, the Mach number to 2.4, and the angle of attack to 8°, the second image indicates that the hinge-line separation bubble has lifted off the surface to become a vortex. The third image provides roughly the same pressure loading on the upper surface; however, there exists a separation bubble at the leading edge with a cross-flow shock lying on top of it followed by a hinge-line separation bubble. This occurred at a Mach number of 2.8, an angle of attack of 6°, with a δ_F of 5°. The fourth image has higher pressure loading due to the fact that the hinge-line separation bubble has been replaced

with a vortex. In this case, the δ_F was set at 10°, the angle of attack was 10°, and the Mach number was 2.4. The fifth and sixth images were taken at a Mach number of 2.8. The first was at an angle of attack of 12° with $\delta_F = 10°$. A lambda shock is quite evident on the flap followed by a strong hinge-line vortex. The last image (angle of attack of 16° with a δ_F of 15°) has a shock located on the outboard flap followed again by a strong hinge-line vortex with shock.

It is clear from the data of figures 57 to 59 that, unlike the effect of thickness or leading-edge radius, the effect of camber does not result in a uniform progression in the location of the vortex or the strength of the vortex. However, once flow separation occurs at the wing leading edge ($\alpha > 10°$), the flow behaves similar to that for thin flat wings. Increasing wing camber (i.e., δ_F deflection) delays the formation of a wing leading-edge vortex. Figure 59 is a map of the lee-side flow type for variations in flap deflection angle and angle of attack. This result was derived from all of the data reported in reference 59. The data show that five distinct flow types exist on the lee side of the cambered delta wings at supersonic speeds. The data of figure 59 also show that there are both low-lift and high-lift (α varies between 0° and 8°) conditions in which a vortex resides on a deflected leading-edge flap at supersonic speeds, clearly suggesting that improved aerodynamic performance is available for wings with vortex flow.

Despite the differences in the vortex-flow structure over the upper surface of flat and cambered wings, the lift-curve slopes are very similar (ref. 181) suggesting a similarity in upper surface loading. A designer may take the similarity in loading into account when engineering a wing upper surface that will efficiently use this loading to create improved performance across the lift range.

Wing Design

In the previous sections of this paper, a variety of vortex-flow structures have been shown to exist on a wide variety of vehicles and simple shapes. In the previous section entitled "Designed Vortex Structures," data have been shown that indicate significant aerodynamic performance improvements are available by considering vortex flows as a primary design feature. This final section of the paper briefly discusses the idea of designing wings that use vortex flows for improved aerodynamic performance at supersonic speeds.

Design Philosophy

Until the middle 1990s, most supersonic wing design activities used linear-theory design methods. However, it has only been in the last few years that the trend has been to use Euler and Navier-Stokes methods for design. These methods are typically coupled with numerical optimization techniques and use highly constrained models to modify the geometry in the design process. Even though the design community is moving to the routine use of more advanced computational methods, the philosophy and understanding behind the design approach is primarily founded in linear thinking. Designs of supersonic aircraft continue to employ traditional linear-theory rules for planform, airfoil selection, camber shapes, and the integration of aircraft components (i.e., wing, body, tails, and nacelles). The location of maximum airfoil thickness (typically located at 40- to 50-percent chord) and the choice of sharp leading edges (especially when the leading-edge sweep implies a supersonic leading-edge condition) continue to be zero- or first-order design guidelines.

It is critical that nonphysical constraints or limitation of theory or tools not restrict the design of a vehicle. Aerodynamic design must be based upon physical observation and knowledge. A possible philosophy for design is that postulated by Kucheman (ref. 1):

> "Flow fields suitable for efficient aerodynamic design must be steady, stable and controllable, changing quantitatively with changes in attitude and Mach number while remaining qualitatively of the same type throughout the whole flight range."

In review of this philosophy, it is clear that vortex flow design easily satisfies the criteria; however, the authors prefer not to be bound by a single-feature flow type in the design process. Perhaps a natural extension to the Kucheman philosophy is reflected in the following quote offered by the authors:

> "The induced effect of flow fields suitable for efficient aerodynamic design must be steady, stable and controllable, changing quantitatively with changes in attitude and Mach number while remaining qualitatively of the same type throughout the whole flight range."

It is this philosophy upon which the subsequent discussion is based.

Design Observations

The supersonic aerodynamics of a sharp leading-edge swept wing dominated by vortex flow is nearly identical to that for a blunt leading-edge wing with fully attached flow and the same Mach and angle of attack (ref. 182). In a similar fashion, the transonic and subsonic aerodynamics of thin swept wings are also fairly insensitive to small geometric variations, such as wing leading-edge shape. These observations allow the designer to configure the geometric details of a wing based upon the loading and not the specific flow field.

To configure a wing for multiple design conditions (other than zero lift), it has been found that higher performance (lower drag and higher lift) can be achieved by adding bluntness/thickness to the wing leading edge and varying the maximum airfoil thickness location between 20- and 60-percent chord (ref. 182).

In figure 60, several useful (linear-theory based) design boundaries are outlined. The curves of interest to most designers are the linear theory 0-percent leading-edge thrust curve and the linear theory 100-percent leading-edge thrust curves. For zero-thickness flat wings, 0-percent leading-edge thrust defines the linear theory predicted drag performance of a wing with attached flow conditions. However, it is well-known that for a thin, sharp, leading-edge swept wing at angle of attack the flow will separate at the leading edge and form a vortex. The resulting performance level for this case is defined as 100-percent vortex lift. This curve accurately represents the performance level that is achieved by a thin uncambered (zero-thickness, flat) wing designed to use the leading-edge vortex. The third linear-theory based curve depicted in figure 60 is the 100-percent leading-edge thrust curve. This curve is the linear-theory "best" design. This curve also assumes an unachievable level of attached flow at the wing leading edge. Note, it is this curve that existing designs are measured against.

Also shown in figure 60 are new boundaries, which reflect nonlinear viscous effects that are known to be present. This boundary has been defined through a review and analysis of existing experimental data (refs. 181 and 182). A more detailed discussion of this curve is provided in reference 182 in which the natural flow wing (NFW) design philosophy is presented. This design concept uses the naturally occurring flow over a wing and shapes the underlying surface contours to take advantage of the surface pressures generated by those flow structures.

Design Approach

Figure 61 illustrates how the NFW approach can be applied to delta wings. A typical wing design will choose a maximum airfoil thickness location and apply this to the entire wing. This results in a wing that has a geometry conical about the wing tip (solid line on left-hand side of figure). However, as was seen in the previous sections of this paper, the flow field on the lee side of highly swept wings is actually conical about the apex of the wing. That is, the flow over a wing at moderate to high-lift conditions may be characterized by an expansion over the leading edge that is followed by a recompression to a more positive pressure as the flow moves inboard and aft. This recompression line lies along a ray that emanates from the wing apex. The shaded regions on the figure indicate the low-pressure (expanded flow) regions on the wing. If one

applies the surface pressures to the surface geometry, one can resolve a lift and drag component. Thus, four regions of drag can be obtained. Forward of the maximum thickness line, the surface has forward-facing slope. Near the leading edge where the flow is expanding, the pressures are low, thus, a low pressure acting on a forward-facing slope would provide a thrust or low drag. Therefore, region B in the figure would be a low-drag region. However, region A, where the flow has recompressed to higher pressures, would be a high-drag region because high pressures acting on a forward-facing slope will generate a positive drag value. Aft of the maximum thickness line, the slope of the surface is aft-facing. Thus, near the leading edge, in the expanded-flow region, the drag would again be high because low pressures acting on an aft-facing surface will produce positive drag values. And finally, in regions where the flow has recompressed and the slopes are aft-facing, one would expect to obtain low drag or thrust because high pressure acting on an aft-facing surface would generate low positive or even negative values of drag (i.e., thrust). Thus, a goal of the designer would be to reduce the sizes of regions A and C while maximizing the sizes of regions B and D. On the right side of figure 61 is a drawing of the natural flow airfoil maximum thickness line. The maximum thickness location approaches the apex and actually would fall downstream of the trailing edge at the tip (see fig. 62). With this approach, one would reduce the size of region A and completely eliminate region C.

Design Results

The NFW approach was applied to a 65° swept delta wing (ref. 182) and the resulting geometries that were tested in the UPWT are shown in figure 63. It should be noted that the natural flow wing is sharp and thin inboard, becoming thicker with a blunt leading edge outboard. It was noted in previous sections that a thin, sharp leading edge moved the vortex action line more inboard compared with a wing having increased bluntness or thickness. However, a more blunt leading edge provided for more attached flow and also leading-edge thrust. The sharp leading edge at the apex and the thin airfoil section at the centerline of the NFW design allows the vortex to set up stronger and maintain strength as if it were a wing that was sharp to the tip. The added bluntness and thickness outboard provides additional surface area and improved surface slopes to reduce drag. Figure 64 shows oil-flow photographs of the three wings tested in the study. The NFW design had an oil accumulation line that ran parallel with the leading edge. This coincides with the location of the airfoil maximum thickness location. The predicted and experimentally determined performance agreed very well and is shown in figure 65. The NFW design philosophy has recently been used in several advanced concepts, including the now defunct national High-Speed Research (HSR) Program (ref. 2).

Concluding Remarks

An overview of the high-speed vortex flow experimental research conducted at Langley Research Center (LaRC) during the 1970s, 1980s, and 1990s has been presented. Data have been shown for flat plates, cavities, bodies, missiles, wings, and aircraft for a Mach number range of 1.5 to 4.6. These data are presented and discussed in the context of the design of future vehicles. In order to provide perspective on these research results, a brief historical review of the extensive body of high-speed vortex flow research from the 1940s has also been presented.

Data presented show that a wide variety of sharp-edge and smooth-wall resultant vortex structures occurs on all vehicles at supersonic speeds. The data also show the presence of both small- and large-scale vortex structures for a variety of vehicles from missiles to transports. These vortex structures have historically been viewed as unfavorable flow features. In an effort to evaluate this viewpoint, the subject data have been analyzed to determine the impact of these various flow structures on vehicle performance and control. The preliminary analysis of these data indicated that these vortex structures are not detrimental and in fact have the potential to provide very significant positive-interference

benefits. The data for the resultant vortex structures indicated that all of the flows are steady, stable, and controllable, changing quantitatively with changes in attitude and Mach number while remaining qualitatively of the same type.

For cavities, the data show complex multiple-vortex structures at all combinations of cavity depth-to-length ratios and Mach number. The data showed that the cavity flow fields, vortex structures, and resultant aerodynamics are steady, stable, and remained qualitatively similar with changes in Mach number for both open- and closed-cavity flow.

The data presented have shown that missiles at high angles of attack can have multiple sets of counterrotating vortex structures that flow aft over the vehicle and interact with the downstream control surfaces. For missiles in roll, the complexity of the vortex dominated flow fields and resulting interference patterns increases dramatically. Data have been shown that demonstrate the capability of these interference effects to influence vehicle flight performance. Analysis presented indicates that significant improvements in the flight characteristics can be achieved through the management of these interference effects. The data also showed that these vortex dominated flow fields are controllable.

For wings and aircraft, the data highlight the effects that leading-edge sweep, leading-edge bluntness, wing thickness, location of maximum thickness, and camber have on vortex formation and the resultant aerodynamics. The data presented for the lee-side flow fields for delta wings showed that the vortex flow structures develop in a logical and continuous fashion with changes in wing geometry, Mach number, and angle of attack. Wing and wing-body aerodynamic data and flow field have been shown that indicate aerodynamic performance improvements are available by considering vortex flows as a primary design feature.

Finally, a design approach for wings/aircraft, which use vortex flows, to improve aerodynamic performance at supersonic speeds was presented and discussed. The subject design approach uses the observation that the loading on thin, swept wings at supersonic speeds is minimally affected by the lee-side flow-field characteristics. Data were presented that show the performance of a wing, with a lee-side vortex, produced with this design approach exceeds that which may be achieved by traditional design methods.

This paper has provided a brief overview of the high-speed vortex flow research at LaRC in the hope of stimulating the aerodynamic community to investigate the potential of vortex flows to improve the aerodynamic performance and control of future aircraft.

References

1. Kucheman, D.: *The Aerodynamic Design of Aircraft*. Pergamon Press, 1978.

2. *First NASA/Industry High-Speed Research Configuration Aerodynamics Workshop*. R. M. Wood, ed. NASA/CP-209690/PT1, 1999.

3. Barret, C.: *Lifting Body Stability and Control*. NASA TM-1999-209255, 1999.

4. Jones, R. T.: *Estimated Lift-Drag Ratios at Supersonic Speed*. NACA TN-1350, 1947a.

5. Jones, R. T.: *Effects of Sweep-Back on Boundary Layer and Separation*. NACA Report No. 884, 1947b.

6. Riebe, J. M.; and Fikes, J. E.: *Preliminary Aerodynamic Investigation of the Effect of Camber on a 60° Delta Wing With Round and Beveled Leading Edges*. NACA RM L9F10, 1949.

7. Vincenti, W. G.: *Comparison Between Theory and Experiment for Wings at Supersonic Speeds*. NACA Rep. 1033, 1949.

8. Lee, G. H.: Note on the Flow Around Delta Wings With Sharp Leading Edges. R.&M. No. 3070, British ARC, 1955.

9. Love, E. S.: *Investigations at Supersonic Speeds of 22 Triangular Wings Representing Two Airfoil Sections for Each of 11 Apex Angles*. NACA Rep. 1238, 1955.

10. Michael, W. H., Jr.: *Flow Studies on Drooped-Leading-Edge Delta Wings at Supersonic Speed*. NACA TN-3614, 1956.

11. Michael, W. H., Jr.: *Flow Studies on Flat Plate Delta Wings at Supersonic Speed*. NACA TN-3472, 1955.

12. Brown, C. E.; and Michael, W. H., Jr.: *On Slender Delta Wings With Leading Edge Separation*. NACA TN-3430, 1955.

13. Boatright, W. B.: *Experimental Study and Analysis of Loading and Pressure Distributions on Delta Wings Due to Thickness and to Angle of Attack at Supersonic Speeds*. NACA RM L56I14, 1956.

14. Sacks, A. H.: Vortex Interference Effects on the Aerodynamics of Slender Airplanes and Missiles. *Jour. Aero. Sci.*, vol. 24, no. 6, June 1957, pp. 393–412.

15. Smith, F. M.: *Experimental and Theoretical Aerodynamic Characteristics of Two Low-Aspect-Ratio Delta Wings at Angles of Attack to 50° at a Mach Number of 4.07*. NACA RM L57E02, 1957.

16. Nielsen, J. N.: *The Effects of Body Vortices and the Wing Shock-Expansion Field on the Pitch-Up Characteristics of Supersonic Airplanes*. NACA RM A57L23, 1958.

17. Boatright, W. B.: *An Analysis of Pressure Studies and Experimental and Theoretical Downwash and Sidewash Behind Five Pointed-Tip Wings at Supersonic Speeds*. NACA Rep. 1380, 1958.

18. Chapman, D. R.; Kuehn, D. M.; and Larson, H. K.: *Investigation of Separated Flows in Supersonic and Subsonic Streams With Emphasis on the Effect of Transition*. NACA Rep. 1356, 1958.

19. Mueller, J. N.; and Grimaud, J. E.: *Effects of Twist and Camber and Thickness on the Aerodynamic Characteristics of a 75° Swept Arrow Wing at a Mach Number of 2.91*. NACA TM X-138, 1959.

20. Hall, I. M.; and Rogers, E. W. W.: *The Flow Patterns on a Tapered Sweptback Wing at Mach Numbers Between 0.6 and 1.6*. R.&M. No. 3271, Part 1, British ARC, 1960.

21. Allen, H. J.; and Perkins, E. W.: *A Study of the Effects of Viscosity on Flow Over Slender Inclined Bodies of Revolution*. NACA Rep. 1048, 1951.

22. Boyd, V. W.; and Phelps, E. R.: *A Comparison of Experimental and Theoretical Loading Over Triangular Wings at Supersonic Speeds*. NACA TIB-2591, 1951.

23. Hatch, V. E.; and Hargrave, L. E.: *Effects of Reynolds Number on the Aerodynamic Characteristics of a Delta Wing at Mach Number 2.41*. NACA TIB-2919, 1951.

24. Maskell, E. C.: Flow Separation in Three-Dimensions. Aero. Rep. 1565, British RAE, 1955.

25. Maskell, E. C.; and Kucheman, D.: *Controlled Separation in Aerodynamic Design*. TM 463, British RAE, 1956.

26. Maskell, E. C.; and Weber, J.: On the Aerodynamic Design of Swept Wings. *Jour. of Royal Aero. Soc.*, vol. 63, Dec. 1959, pp. 709–721.

27. Rogers, E. W. E.; and Berry, C. J.: *Experiments at M = 1.41 on Elliptic Cones With Subsonic Leading Edges*. R.&M. No. 3042, British ARC, 1952.

28. Stewart, H. J.: The Lift of a Delta Wing at Supersonic Speeds. *Q. Appl. Math.*, vol. 4, no. 3, 1946, pp. 246–254.

29. Ellis, D. G.; and Stollery, J. L.: The Behaviour and Performance of Leading-Edge Vortex Flaps. *Proceedings of the 16th Congress of the International Council of the Aeronautical Sciences*. ICAS Paper 88-4.5.2, 1988.

30. Harris, R. V., Jr.: On the Threshold—Outlook for Supersonic and Hypersonic Aircraft. AIAA-89-2071, Aug. 1989.

31. Reed, R. D.: *Wingless Flight: The Lifting Body Story*. NASA SP-4220, 1997.

32. Lamar, J. E.; and Campbell, J. F.: Recent Studies at NASA-Langley of Vortical Flows Interacting With Neighboring Surfaces. AGARD CP-342, Paper 10, 1983.

33. Campbell, J. F.; and Chambers, J. R.: *Patterns in the Sky—Natural Visualization of Aircraft Flow Fields*. NASA SP-514, 1994.

34. Ogawa, A.: *Vortex Flow*. CRC Press, 1993.

35. *High Angle-of-Attack Aerodynamics*, Wendt, J. F., ed., AGARD LS-121, March 1982.

36. Rom, J.: *High Angle of Attack Aerodynamics—Subsonic, Transonic, and Supersonic Flows*. New York Springer-Verlag, 1992.

37. Stanbrook, A.: *Experimental Observation of Vortices in Wing-Body Junctions*. R.&M. No. 3114, British ARC, 1959.

38. Squire, L. C.: Flow Regimes Over Delta Wings at Supersonic and Hypersonic Speeds. *Aero. Quart.*, vol. 27, Feb. 1976, pp. 1–14.

39. Stanbrook, A.; and Squire, L. C.: Possible Types of Flow at Swept Leading Edges. *Aero. Quart.*, vol. 15, pt. 1, Feb. 1964, pp. 72–82.

40. Kucheman, D.: Aircraft Shapes and Theoretical Aerodynamics for Flight at Supersonic Speeds. Von Karman: Advances in Aeronautical Sciences, *Proceeding of the Second International Congress in the Aeronautical Sciences*, Zurich. 12–16 Sept., 1960, vol. 3, 1962, pp. 221–252.

41. Kucheman, D.: *On the Possibilities of Designing Wings That Combine Vortex Flows With Classical Aerofoil Flows*. Tech. Memo. Aero. 1363, British RAE, Oct. 1971.

42. Kucheman, D.; and Weber, J.: Vortex Motions. *ZAMM*, vol. 7, no. 8, 1965, pp. 457–474.

43. Von Karman, T.; Ballantyne, A. M.; Dexter, R. R.; Bock, G.; Dryden, H. L.; and Roy, M.: Advances in Aeronautical Sciences. *Proceedings of the Second International Congress in the Aeronautical Sciences, Zurich, 12–16 September, 1960*, vol. 3, 1962.

44. Squire, L. C.: *Camber Effects on the Non-Linear Lift of Slender Wings With Sharp Leading Edges*. CP No. 924, British ARC, 1967.

45. Squire, L. C.: Flow Regimes Over Delta Wings at Supersonic and Hypersonic Speeds. *Aero. Quart.*, vol. 27, pt. 1, Feb. 1976.

46. Squire, L. C.: *Pressure Distributions and Flow Patterns on Some Conical Shapes With Sharp Edges and Symmetrical Cross-Sections at M = 4.0*. R.&M. No. 3340, British ARC, 1963.

47. Squire, L. C.; Jones, J. G.; and Stanbrook, A.: *An Experimental Investigation of the Characteristics of Some Plane and Cambered 65° Delta Wings at Mach Numbers From 0.7 to 2.0*. R.&M. No. 3305, British ARC, 1963.

48. Peake, D. J.; and Tobak, M.: *Three-Dimensional Flows About Simple Components at Angle of Attack*. Paper No. 2, AGARD Lecture Series No. 121 on High Angle-of-Attack Aerodynamics. Mar. 1982.

49. Peake, D. J.; and Tobak, M.: *Three-Dimensional Interactions and Vortical Flows With Emphasis on High Speeds*. NASA TM-81169, 1980.

50. Tobak, M.; and Peake, D. J.: Topology of Three-Dimensional Separated Flows. *Ann. Rev. Fluid. Mech.*, vol. 14, 1982, pp. 61–85.

51. Bannink, W. J.; and Nebbeling, C.: Investigation of the Expansion Side of a Delta Wing at Supersonic Speeds. *AIAA J.*, vol. 11, no. 8, Aug. 1973, pp. 1151–1156.

52. Bashkin, V. A.: Experimental Study of Flow About Flat Delta Wings at M = 5 and Angles of Attack From 0 to 70°. *Izvestiya Akademiya Nauk SSSR Mekhanika Zhidkosti I Gaza*, vol. 23, 1967, pp. 102–108.

53. Brown, C. E.; McLean, F. E.; and Klunker, E. B.: Theoretical and Experimental Studies of Cambered and Twisted Wings Optimized for Flight at Supersonic Speeds. Von Karman: Advances in Aeronautical Sciences, *Proceedings of the Second International Congress in the Aeronautical Sciences, Zurich, 12–16 September, 1960*, vol. 3, 1962, pp. 415–431.

54. Carafoli, E.: Wing Theory in Supersonic Flow. *Pergamon Press Int. Series of Monographs in Aero. and Astro.*, vol. 7, 1969.

55. Cleary, J. W.: *Lee-Side Flow Phenomena on Space Shuttle Configurations at Hypersonic Speeds. Part 1: Flow Separation and Flow Field Viscous Phenomena of a Delta-Wing Shuttle Orbiter Configuration*. NASA TM X-2507/L-8136-Vol. 2, 1972.

56. Cross, E. J.; and Hankey, W. L.: Investigation of the Leeward Side of a Delta Wing at Hypersonic Speeds. *J. of Spacecr. and Rockets*, vol. 6, no. 2, Feb. 1969, pp. 185–190.

57. Danavant, J. C.; Narayan, K. Y.; and Walberg, G. D.: A Survey of Leeside Flow and Heat Transfer on Delta Planform Configurations. AIAA-76-118, Jan. 1976.

58. Degani, D.; and Schiff, L. B.: Computation of Supersonic Viscous Flows Around Pointed Bodies at Large Incidence. AIAA-83-0034, Jan. 1983.

59. Delery, J. M.: Physics of Vortical Flows. *J. of Aircr.*, vol. 29, no. 5, Sept.–Oct. 1992, pp. 856–876.

60. Delery, J.; Horowitz, E.; Leuchter, O.; and Solignac, J. L.: Fundamental Studies on Vortex Flows. *Rech. Aerosp.*, vol. 2, 1984.

61. Fellows, K. A.; and Carter, E. C.: *Results and Analysis of Pressure Measurements on Two Isolated Slender Wings and Slender Wing-Body Combinations at Supersonic Speeds, Part 1—Analysis*. CP No. 1131, British ARC, 1970.

62. Fournier, R. H.; and Spencer, B., Jr.: *Aerodynamic Characteristics at Mach Numbers From 1.50 to 4.63 of a Variable-Geometry Lifting Reentry Concept Employing Elevator and Body Base Flaps for Control*. NASA TM X-1351, 1967.

63. Ganzer, U.; Hoder, H.; and Szodruch, J.: On the Aerodynamics of Hypersonic Cruise Vehicles at Off-Design Conditions. 1978, Vol. I - Fuel Conservation, Hyp. Veh., Environ. Effects, Materials and Struc., Comp. Aero., Wind Tunnels, Flight Testing, Stability and Control. ICAS Proceedings. J. Singer and R. Staufenbiel, eds., 1978, pp. 152–161.

64. Goodsell, A. M.; and Melton, J. E.: *Transonic and Supersonic Euler Computations of Vortex Dominated Flow Fields About a Generic Fighter*. NASA TP 3156, 1991.

65. Gunko, I. U. P.; and Mazhul, I. I.: *Investigation of the Regimes of Flow Past the Upper Surface of Delta Wings With Shock Waves Separated From the Leading Edges*. Akademiia Nauk SSSR, 1979.

66. Hefner, J. N.: *Lee-Surface Heating and Flow Phenomena on Space Shuttle Orbiters at Large Angles of Attack and Hypersonic Speeds*. NASA TN D-7088, 1972.

67. Hemsch, M. J.: *Semi-Empirical Methods for Conventional and Unconventional Missiles*. AGARD Rep. No. 754, Paper 4, 1988.

68. Larsson, P. O.: *A Note on Supersonic and Transonic Flow Around Delta Wings*. Royal Institute of Technology, CN-154394, 1954.

69. Linde, M.: The Flow on the Lee-Side of a Delta Wing at Mach 7. *The Second Joint Europe/U.S. Short Course in Hypersonics*, 1989.

70. McRae, D. S.; Peake, D. J.; and Fisher, D. F.: A Computational and Experimental Study of High Reynolds Number Viscous/Inviscid Interaction About a Cone at High Angle of Attack. AIAA-80-1422, July 1980.

71. Morris, O. A.: *Aerodynamic Characteristics in Pitch at a Mach Number of 2.01 of Several Wing-Body Combinations With Wedge-Shaped Bodies Located Above and Below a 54.5° Swept Delta Wing*. NASA TN D-1823, 1963.

72. Murman, E. M.; Powell, K. G.; Miller, D. S.; and Wood, R. M.: Comparison of Computations and Experimental Data for Leading-Edge Vortices—Effects of Yaw and Vortex Flaps. AIAA-86-0439, Jan. 1986.

73. Narayan, K. Y.; and Hartman, K.: Transonic and Supersonic Flow Past a 65° Delta Wing With Round Leading Edges—Analysis of Experimental Data. DFVLR-FB 88-44, Oct. 1988.

74. Narayan, K. Y.: Lee-Side Flowfield and Heat Transfer of a Delta Wing at M = 10.0. *AIAA J.*, vol. 16, no. 2, p. 160.

75. Nastase, A.: Some Considerations on Leading-Edge Vortices on Wings in Supersonic Flow. *Fluid Dynamic Research 3*, 1988, pp. 387–391.

76. Newsome, R. W.; and Kandil, O. A.: Vortical Flow Aerodynamics-Physical Aspects and Numerical Simulation. AIAA-87-0205, Jan. 1987.

77. Newsome, R. W.; and Thomas, J. L.: *Computation of Leading-Edge Vortex Flows.* NASA CP-2416, 1985.

78. Oberkampf, W. L.; and Bartel, T. J.: Supersonic Flow Measurements in the Body Vortex Wake of an Ogive Nose Cylinder. AIAA-78-787, April 1978.

79. Pagan, D.; and Molton, P.: Basic Experiment on a Supersonic Vortex Flow Around a Missile Body. AIAA-91-0287, Jan. 1991.

80. Povinelli, L. A.; and Povinelli, F. P.: Vortex Enhancement of Jet Penetration in Supersonic Flow. AIAA-69-664, June 1969.

81. Rao, D. M.; and Whitehead, A. H.: Lee-Side Vortices on Delta Wings at Hypersonic Speeds. *AIAA J.*, vol. 10, Nov. 1972, pp. 1458–1465.

82. Reding, J. P.; and Ericsson, L. E.: Effects of Delta Dynamics. *J. of Spacecr. & Rockets*, vol. 10, no. 7, July 1973, pp. 421–428.

83. Richards, I. C.: Supersonic Flow Past a Slender Delta Wing. An Experimental Investigation Covering the Incidence Range $-5° < a < 50°$. *Aeronaut. Q.*, March 1976.

84. Schrader, K. F.; Reynolds, G. A.; and Novak, C. J.: Effects of Mach Number and Reynolds Number on Leading-Edge Vortices at High Angle-of-Attack. AIAA-88-0122, Jan. 1988.

85. Smith, J. H. B.: Improved Calculations of Leading Edge Separation From Slender, Thin, Delta Wings. *Proc. Roy. Soc. A*., vol. 306, 1968, pp. 67–90.

86. Smith, L. G.; and Maurice, M. S.: Laser Velocimetry Measurements of Supersonic Vortex Flows on Simple Razor-Edged Delta Wing. AIAA-91-1684, June 1991.

87. Snyder, M. H., Jr.: *On the Theory of the Delta Wing*. AR 66-4, Wichita State University, Sept. 1966.

88. Sorrells, R. B., III; and Landrum, E. J.: *Theoretical and Experimental Study of Twisted and Cambered Delta Wings Designed for a Mach Number of 3.5*. NASA TN D-8247, 1976.

89. Stallings, R. L.; and Lamb, M.: *Wing-Alone Characteristics for High Angles of Attack at Supersonic Speeds*. NASA TP-1889, 1981.

90. Stallings, R. L.; Lamb, M.; and Watson, C. B.: *Effect of Reynolds Number on Stability Characteristics of a Cruciform Wing-Body at Supersonic Speeds*. NASA TP-1683, 1980.

91. Stallings, R. L.: Low Aspect Ratio Wings at High Angles of Attack. Tactical Missile Aerodynamics. *AIAA Prog. In Astro. and Aero.*, vol. 104, 1986, pp. 89–128.

92. Szodruch, J.; and Ganzer, U.: *On the Lee-Side Flow Over Delta Wings at High Angle of Attack*. AGARD CP-247, 1978.

93. Szodruch, J.; and Squire, L. C.: Pressure Distribution on the Suction Surface of Some Delta Wings at M = 3.5. No. 35-008, British ARC, 1974.

94. Thomann, H.: *Measurement of Heat Transfer, Recovery Temperature and Pressure Distribution on Delta Wings at M = 3*. FFA Rep. 93, Sweden, 1962.

95. Thomas, J. L.; and Newsome, R. W.: Navier-Stokes Computations of Lee-Side Flows Over Delta Wings. AIAA-86-1049, May 1986.

96. Xing, W. F.; and Marenbach, G.: *Periodic Vortex Shedding in the Supersonic Wake of a Planar Plate*. NASA TM-77854, 1985.

97. Zubin, M. A.; and Osteapenko, N. A.: *The Experimental Investigation of Some Characteristics of the Supersonic Flow Around Delta Wings*. Akademiia Nauk SSSR, 1975.

98. *Aerodynamics of Vortical Type Flows in Three Dimensions*. Young, A. D., ed., AGARD CP-342, April 1983.

99. *Fifty Years of Aeronautical Research*. NASA EP-45, 1968.

100. *Introduction to Vortex Dynamics*. Von Karman Institute for Fluid Dynamics, Lecture Series 1986-08, Vol. 2, Wendt, J. F., ed., May 1986.

101. *Vortex Flow Aerodynamics—Vol. II*, Campbell, J. F., ed., NASA CP-2417, 1985.

102. Smith, J. H. B.: *A Review of Separation in Steady Three-Dimensional Flow*. AGARD CP-168, May 1975.

103. Sutton, E. P.: Some Observations of the Flow Over a Delta Winged Model With 55-deg Leading-Edge Sweep, at Mach Numbers Between 0.4 and 1.8. R.&M. No. 3190. British ARC, 1960.

104. Szodruch, J.: Reynolds Number Influence on Leeside Flowfields. *AIAA J.*, vol. 16, no. 12, 1978, pp. 1306–1309.

105. Szodruch, J. G.; and Peake, D. J.: *Leeward Flow Over Delta Wings at Supersonic Speeds*. NASA TM-81187, 1980.

106. Miller, D. S.; and Wood, R. M.: Leeside Flows Over Delta Wings at Supersonic Speeds. *J. Aircr.*, vol. 21, no. 9, Sept. 1984, pp. 680–686.

107. Wood, R. M.; and Miller, D. S.: Impact of Airfoil Profile on the Supersonic Aerodynamics of Delta Wings. AIAA-85-4073, Oct. 1985.

108. Wood, R. M.; and Miller, D. S.: Fundamental Aerodynamic Characteristics of Delta Wings With Leading Edge Vortex Flows. *J. Aircr.*, vol. 22, no. 6, June 1985, pp. 479–485.

109. Wood, R. M.; and Miller, D. S.: Assessment of Preliminary Prediction Techniques for Wing Leading-Edge Vortex Flows at Supersonic Speeds. *J. Aircr.*, vol. 22, no. 6, June 1985, pp. 473–478.

110. Wood, R. M.; and Watson, C. B.: *Study of Lee-Side Flows Over Conically Cambered Delta Wings at Supersonic Speeds*. NASA TP-2660, Parts 1 and 2, 1987.

111. Ganzer, U.; and Szodruch, J.: Vortex Formation Over Delta, Double-Delta and Wave Rider Configurations at Supersonic Speeds. AGARD, Aerodynamics of Hypersonic Lifting Vehicles. Nov. 1987.

112. Covell, P. F.; and Wesselman, G.: Flow Field Characteristics and Normal-Force Correlations for Delta Wings From Mach 2.4 to 4.6. AIAA-89-0026, Jan. 1989.

113. Rainbird, W. J.: *The External Flow Field About Yawed Circular Cones*. AGARD CP-30, 1968.

114. Rainbird, W. J.: Turbulent Boundary Layer Growth and Separation on a Yawed 12.5 Cone at Mach Numbers 1.8 and 4.25. *AIAA J.*, vol. 6, no. 12, Dec. 1968, pp. 2410–2416.

115. Graves, E. B.; and Fournier, R. H.: *Effect of Nose Bluntness and Afterbody Shape on Aerodynamic Characteristics of a Monoplanar Missile Concept With Bodies of Circular and Elliptical Cross Sections at a Mach Number of 2.50*. NASA TM-80055, 1979.

116. Allen, J. M.; and Dillenius, F. E.: Vortex Development on Slender Missiles at Supersonic Speeds. AIAA-79-0360, Jan. 1979.

117. Allen, J. M.; and Pittman, J. L.: Analysis of Surface Pressure Distributions on Two Elliptic Missile Configurations. AIAA-83-1841, July 1983.

118. Gartling, D. K.: Tests of Vortex Generators to Prevent Separation of Supersonic Flow in a Compression Corner. ARL-TR-70-44, U.S. Army, 1970.

119. Hazelwood, R.: *An Investigation of Cavity Vortex Generators in Supersonic Flow*. NASA CR-198202, 1996.

120. Samimy, M.; Reeder, M.; and Zaman, K.: Supersonic Jet Mixing Enhancement by Vortex Generations. AIAA-91-2263, June 1991.

121. Greene, G. C.; Lamar, J. E.; and Kubendran, L. R.: Aircraft Vortices: Juncture, Wing, and Wake. AIAA-88-3742, Jan. 1988.

122. Kandil, O. A.; Kandil, H. A.; and Liu, C. H.: Three-Dimensional Supersonic Vortex Breakdown. AIAA-93-0526, Jan. 1993.

123. Siclari, M. J.: Asymmetric Separated Flows at Supersonic Speeds. AIAA-90-0595, Jan. 1990.

124. Metwally, O. M.: The Interaction of a Supersonic Streamwise Vortex and a Normal Shock Wave. Thesis, Univ. of Cranfield, Aug. 1989.

125. Settles, G. S.; and Cattafesta, L.: *Supersonic Shock Wave/Vortex Interaction*. NASA CR-192917, 1993.

126. Campbell, J. F.; Osborn, R. F.; and Foughner, J. T., Jr.: *Vortex Flow Aerodynamics, Vol. II*. NASA CR-2417, 1985.

127. Marchman, J. F.; Plentovich, E. B.; and Manor, D.: Performance Improvement of Delta Wings at Subsonic Speeds Due to Vortex Flaps. AIAA-80-1802, Aug. 1980.

128. Erickson, G. E.; Schreiner, J. A.; and Rogers, L. W.: Multiple Vortex and Shock Interactions at Subsonic, Transonic, and Supersonic Speeds. AIAA-90-3023, Aug. 1990.

129. Erickson, G. E.; Schreiner, J. A.; and Rogers, L. W.: Canard-Wing Vortex Interactions at Subsonic Through Supersonic Speeds. AIAA-90-2814, Aug. 1990.

130. McGrath, B. E.: Computational Study of a Conical Wing Having Unit Aspect Ratio at Supersonic Speeds. AIAA-93-3505, Aug. 1993.

131. McMillin, S. N.: Navier Stokes Solutions for Leeside Flows Over Supersonic Delta Wings—A Validation Study. Thesis, George Washington Univ., July 1989.

132. McMillin, S. N.; Thomas, J. L.; and Murman, E. M.: Euler and Navier-Stokes Leeside Flows Over Supersonic Delta Wings. *J. Aircr.*, vol. 26, no. 5, May 1989, pp. 452–458.

133. Miller, D. S.; and Wood, R. M.: *Lee-Side Flow Over Delta Wings at Supersonic Speeds*. NASA TP-2430, 1985.

134. Powell, K. G.; Murman, E. M.; Wood, R. M.; and Miller, D. S.: A Comparison of Experimental and Numerical Results for Delta Wings With Vortex Flaps. AIAA-86-1840, June 1986.

135. Rose, O. J.; and Pittman, J. L.: An Euler Analysis of Leading Edge Vortex Flows on a Forebody-Strake at Supersonic Speeds. AIAA-89-0343, Jan. 1989.

136. Shrout, B. L.; and Robins, A. W.: *Longitudinal Aerodynamic Characteristics of an Elliptical Body With a Horizontal Tail at Mach Numbers From 2.3 to 4.63*. NASA TP-2024, 1982.

137. Wood, R. M.; Byrd, J. E.; Krieger, W. B.; and Forrest, D. K.: *Experimental Investigation of the Aerodynamic Characteristics of Eight Forebody Geometries at Supersonic Speeds*. NASA TM-4625, 1997.

138. Wood, R. M.; Byrd, J. E.; and Wesselman, G. F.: *Influence of Airfoil Geometry on Delta Wing Leading-Edge Vortices and Vortex-Induced Aerodynamics at Supersonic Speeds*. NASA TP-3105, 1992.

139. Stallings, R. L., Jr.: Store Separation From Cavities at Supersonic Flight Speeds. *J. Spacecr. & Rockets*, vol. 20, no. 2, Mar.–Apr. 1983, pp. 129–132.

140. Stallings, R. L., Jr.; and Wilcox, F. J., Jr.: *Experimental Cavity Pressure Distributions at Supersonic Speeds.* NASA TP-2683, 1987.

141. Charwat, A. F.; Roos, J. N.; Dewey, F. C., Jr.; and Hitz, J. A.: An Investigation of Separated Flows. Part I: The Pressure Field. *J. Aeronaut. Sci.*, vol. 28, no. 6, June 1961, pp. 457–470.

142. McDearman, R. W.: *Investigation of the Flow in a Rectangular Cavity in a Flat Plate at a Mach Number of 3.55*. NASA TN D-523, 1960.

143. Kaufman, L. G., II; Maciulaitis, A.; and Clark, R. L.: *Mach 0.6 to 3.0 Flows Over Rectangular Cavities*. AFWAL-TR-82-3112, U.S. Air Force, May 1983.

144. McGregor, O. W., Jr.: Aerodynamic Drag of Two-Dimensional Rectangular Notches in Transonic and Supersonic Turbulent Flow (With Emphasis on the Effect of Self-Induced Pressure Oscillations). Ph.D. Diss., Univ. of Illinois, Oct. 1969.

145. Nestler, D. E.: An Experimental Study of Cavity Flow on Sharp and Blunt Cones at Mach 8. AIAA-81-0335, Jan. 1981.

146. Blair, A. B., Jr.; and Stallings, R. L., Jr.: *Supersonic Axial-Force Characteristics of a Rectangular-Box Cavity With Various Length-to-Depth Ratios in a Flat Plate*. NASA TM-87659, 1986.

147. Wilcox, F. J., Jr.: Experimental Measurements of Internal Store Separation Characteristics at Supersonic Speeds. *The Store Carriage, International and Release Conference*, Royal Aero. Soc., Bath, United Kingdom, Apr. 4–6, 1990.

148. Wilcox, Floyd J., Jr.: Use of a Colored Water Flow Visualization Technique in a Supersonic Wind Tunnel to Investigate Cavity Flow Fields. *Flow Visualization VI—Proceedings of the Sixth International Symposium on Flow Visualization*. October 5–9, 1992, Yokohama, Japan; Springer-Verlag, Germany, 1992, pp. 41–45.

149. Jackson, Charlie M., Jr.; Corlett, William A.; and Monta, William J.: *Description and Calibration of the Langley Unitary Plan Wind Tunnel*. NASA TP-1905, 1981.

150. Morris, Odell A.; Corlett, William A.; Wassum, Donald L.; and Babb, C. Donald: *Vapor-Screen Technique for Flow Visualization in the Langley Unitary Plan Wind Tunnel*. NASA TM-86384, 1985.

151. Stallings, Robert L., Jr.; Wilcox, Floyd J., Jr.; and Forrest, Dana K.: *Measurements of Forces, Moments, and Pressures on a Generic Store Separating From a Box Cavity at Supersonic Speeds*. NASA TP-3110, 1991.

152. Birch, T.; Allen, J.; and Wilcox, F.: Force, Surface Pressure and Flowfield Measurements on Slender Missile Configurations at Supersonic Speeds. AIAA-2000-4207, Aug. 2000.

153. Allen, J. M.; Shaw, D. S.; and Sawyer, W. C.: Analysis of Selected Data From the Triservice Data Base. AIAA-89-0478, Jan. 1989.

154. Blair, A. B., Jr.; Allen, J. M.; and Hernandez, G.: *Effect of Tail-Fin Span on Stability and Control Characteristics of a Canard-Controlled Missile at Supersonic Mach Numbers*. NASA TP-2157, 1983.

155. Blair, A. B., Jr.: *Supersonic Aerodynamics Characteristics of a Maneuvering Canard-Controlled With Fixed and Free-Rolling Tail Fins*. SAE Paper 901993, Oct. 1990.

156. Covell, P. F.; Miller, D. S.; and Wood, R. M.: An Investigation of Leading-Edge Flap Performance on Delta and Double-Delta Wings at Supersonic Speeds. AIAA-86-0315, Jan. 1986.

157. Covell, P. F.; Wood, R. M.; and Miller, D. S.: *Investigation of Leading-Edge Flap Performance on Delta and Double-Delta Wings at Supersonic Speeds*. NASA TP-2656, 1987.

158. Darden, C. M.: *Effect of Leading-Edge Load Constraints on the Design and Performance of Supersonic Wings*. NASA TP-2446, 1985.

159. Darden, C. M.: *Effect of Milling Machine Roughness and Wing Dihedral on the Supersonic Aerodynamic Characteristics of a Highly Swept Wing*. NASA TP-2918, 1989.

160. Johnson, S. K: *Flow Field Study at Engine Inlet Stations of Two High-Speed Cruise Aircraft*. NASA TP-2861, 1989.

161. Hernandez, G.; Wood, R. M.; and Covell, P. F.: *Effect of Leading- and Trailing-Edge Flaps on Clipped Delta Wings With and Without Wing Camber at Supersonic Speeds*. NASA TM-4542, 1994.

162. McMillin, S. N.; Bauer, S. X. S.; and Howell, D. T.: *Effect of Planform and Body on Supersonic Aerodynamics of Multibody Configurations*. NASA TP 3212, 1992.

163. McMillin, S. N.; and Wood, R. M.: *Planform Effects on the Supersonic Aerodynamics of Multibody Configurations*. NASA TP-2762, 1987.

164. Robins, A. W.; Carlson, H. W.; and Mack, R. J.: *Supersonic Wings With Significant Leading-Edge Thrust at Cruise*. NASA TP-1632, 1980.

165. Robins, A. W.; Lamb, M.; and Miller, D. S.: *Aerodynamic Characteristics at Mach Numbers of 1.5, 1.8, and 2.0 of a Blended Wing-Body Configuration With and Without Integral Canards*. NASA TP-1427, 1979.

166. Shrout, B. L.: *Effect of a Canard and Wing Leading-Edge Flaps on the Longitudinal Aerodynamic Performance of a Cranked Wing at Supersonic Speeds*. NASA TM-89126, 1987.

167. Wood, R. M.; Miller, D. S.; Raney, D. L.; and Roesch, M. T.: *A Low Lift Wing Camber Design Approach for Fighter Aircraft*. NASA TP-2465, 1985.

168. Wood, R. M.; Rose, O. J.; and McMillin, S. N.: *Effect of Body Cross-Sectional Shape on the Supersonic Aerodynamics of Multibody Configurations*. NASA TP-2587, 1986.

169. Carlson, H. W.; and Mann, M. J.: *Survey and Analysis of Research on Supersonic Drag-Due-to-Lift Minimization With Recommendations for Wing Design*. NASA TP-3202, 1992.

170. Johnson, M. E.: *A Design and Analysis of Maneuver Wing Flaps at Supersonic Speeds With Attainable Leading-Edge Thrust Considerations*. NASA CR-3939, 1985.

171. Kulfan, R. M.: Real Flow Limitations in Supersonic Airplane Design. AIAA-78-147, Jan. 1978.

172. Mason, W. H.: *A Wing Concept for Supersonic Maneuvering*. NASA CR-3763, 1983.

173. Mason, W. H.; Siclari, M. J.; and Miller, D. S.: A Supersonic Maneuver Wing Designed for Nonlinear Attached Flow. AIAA-83-0425, Jan. 1983.

174. Maskell, E. C.: On the Principals of Aerodynamic Design. *Progress in Aero. Sci.*, vol. 1, no. 1, 1961, pp. 1–7.

175. Miller, D. S.; Landrum, E. J.; Townsend, J. C.; and Mason, W. H.: *Pressure and Force Data for a Flat Wing and a Warped Conical Wing Having a Shockless Recompression at Mach 1.62*. NASA TP-1759, 1981.

176. Miller, D. S.; and Wood, R. M.: Aerodynamic Design Considerations for Efficient High-Lift Supersonic Wings. AIAA-85-4076, Oct. 1985.

177. Nelson, C. P.: Effects of Wing Planform on HSCT Off-Design Aerodynamics. AIAA-92-2629-CP, 1992.

178. Seddon, J.; and Spence, A.: The Use of Known Flow Fields as an Approach to the Design of High Speed Aircraft. *AGARD Fluid Dyn. Spec. Meeting*, May 1968.

179. Covell, R. F.; Wood, R. M.; and Miller, D. S.: Investigation of the Vortex Flap Concept on a 75-deg. Sweep Delta Wing at Supersonic Speeds. AIAA-87-2475, Aug. 1987.

180. Kulfan, R. M.: Wing Geometry Effects on Leading Edge Vortices. AIAA-79-1872, Aug. 1979.

181. Wood, R. M.: *Supersonic Aerodynamics of Delta Wings*. NASA TP-2771, 1988.

182. Wood, R. M.; and Bauer, S. X. S.: *The Natural Flow Wing-Design Concept*. NASA TP-3193, 1992.

Table 1. Cross-Reference Between References, Figures, and Research Area

No.	Reference (name)	Figure(s)	Wings and aircraft	Missiles	Cavities	Other
1	Kucheman		X			
2	NASA		X			
3	Barret		X			
4	Jones		X			
5	Jones		X			
6	Riebe		X			
7	Vincenti		X			
8	Lee		X			
9	Love		X			
10	Michael		X			
11	Michael		X			
12	Brown		X			
13	Boatright		X			
14	Sacks		X	X		
15	Smith		X			
16	Nielsen		X			
17	Boatright		X			
18	Chapman		X			
19	Mueller		X			
20	Hall		X			
21	Allen			X		
22	Boyd		X			
23	Hatch		X			
24	Maskell		X			
25	Maskell		X			
26	Maskell		X			
27	Rogers			X		
28	Stewart		X			
29	Stollery		X			
30	Harris		X			
31	Reed		X			
32	Lamar		X			
33	Campbell		X			
34	Ogawa		X			
35	AGARD		X			
36	Rom		X			
37	Stanbrook		X			
38	Stanbrook	7	X			
39	Stanbrook		X			
40	Kucheman		X			
41	Kucheman		X			

Table 1. Continued

No.	Reference (name)	Figure(s)	Wings and aircraft	Missiles	Cavities	Other
42	Kucheman		X			
43	Von Karman		X			
44	Squire		X			
45	Squire		X			
46	Squire		X			
47	Squire		X			
48	Peake		X	X		
49	Peake		X	X		
50	Tobak		X			
51	Bannink		X			
52	Bashkin		X			
53	Brown		X			
54	Carafoli		X			
55	Cleary		X			
56	Cross		X			
57	Danavant		X			
58	Degani			X		
59	Delery		X			
60	Delery		X			
61	Fellows		X	X		
62	Fournier		X			
63	Ganzer		X			
64	Goodsell		X			
65	Gunko		X			
66	Hefner		X			
67	Hemsch			X		
68	Larsson		X			
69	Linde		X			
70	McRae		X	X		
71	Morris		X	X		
72	Murman		X			
73	Narayan		X			
74	Narayan		X			
75	Nastase		X			
76	Newsome		X			
77	Newsome		X			
78	Oberkampf			X		
79	Pagan			X		
80	Povinelli					X
81	Rao		X			
82	Reding		X			

Table 1. Continued

No.	Reference (name)	Figure(s)	Wings and aircraft	Missiles	Cavities	Other
83	Richards		X			
84	Schrader		X			
85	Smith		X			
86	Smith		X			
87	Snyder		X			
88	Sorrells		X			
89	Stallings		X			
90	Stallings		X	X		
91	Stallings			X		
92	Szodruch		X			
93	Szodruch		X			
94	Thomann		X			
95	Thomas		X			
96	Xing		X			
97	Zubin		X			
98	AGARD		X	X		
99	Degani		X			
100	Von Karman Institute					X
101	NASA		X			
102	AGARD		X	X		
103	Sutton		X			
104	Szodruch		X			
105	Szodruch	8	X			
106	Miller	9	X			
107	Wood		X			
108	Wood		X			
109	Wood		X			
110	Wood	56,57,58,59	X			
111	Ganzer		X			
112	Covell	49,50,51	X			
113	Rainbird			X		
114	Rainbird			X		
115	Graves			X		
116	Allen	28,29		X		
117	Allen	32,33,34		X		
118	Gartling					X
119	Hazelwood					X
120	Samimy					X
121	Greene		X			X
122	Kandil		X			X
123	Siclari			X		

Table 1. Continued

No.	Reference (name)	Figure(s)	Wings and aircraft	Missiles	Cavities	Other
124	Metwally					X
125	Settles					X
126	Campbell		X			
127	Marchman		X			
128	Erickson		X			
129	Erickson		X			
130	McGrath		X			
131	McMillin		X			
132	McMillin		X			
133	Miller	47	X			
134	Powell		X			
135	Rose		X	X		
136	Shrout		X	X		
137	Wood		X			
138	Wood	35,53,54,55	X		X	
139	Stallings				X	
140	Stallings	17			X	
141	Charwat				X	
142	McDearman				X	
143	Kaufman				X	
144	McGregor				X	
145	Nestler				X	
146	Blair	18			X	
147	Wilcox	10			X	
148	Wilcox	11,12,13,14,15			X	
149	Jackson					
150	Morris	16				
151	Stallings	19,20			X	
152	Birch	21,22,23		X		
153	Allen	24		X		
154	Blair	25,26,27		X		
155	Blair	30,31		X		
156	Covell		X			
157	Covell	41	X			
158	Darden	36	X			
159	Darden		X			
160	Johnson	39	X			
161	Hernandez	42	X			
162	McMillin		X			
163	McMillin	43,44	X			
164	Robins		X			

Table 1. Concluded

No.	Reference (name)	Figure(s)	Wings and aircraft	Missiles	Cavities	Other
165	Robins		X			
166	Shrout		X			
167	Wood		X			
168	Wood		X			
169	Carlson		X			
170	Johnson		X			
171	Kulfan		X			
172	Mason		X			
173	Mason		X			
174	Maskell		X			
175	Miller		X			
176	Miller		X			
177	Nelson		X			
178	Seddon		X			
179	Covell		X			
180	Kulfan		X			
181	Wood	45,46,51,52	X			
182	Wood	60,61,62,63,64,65	X			

Table 2. Colored Water Flow Test Conditions

Mach number	Reynolds number, 1/ft	Total pressure, psfa	Total temperature, °F
1.50	2.0×10^6	1051	125
2.16	2.0×10^6	1349	125

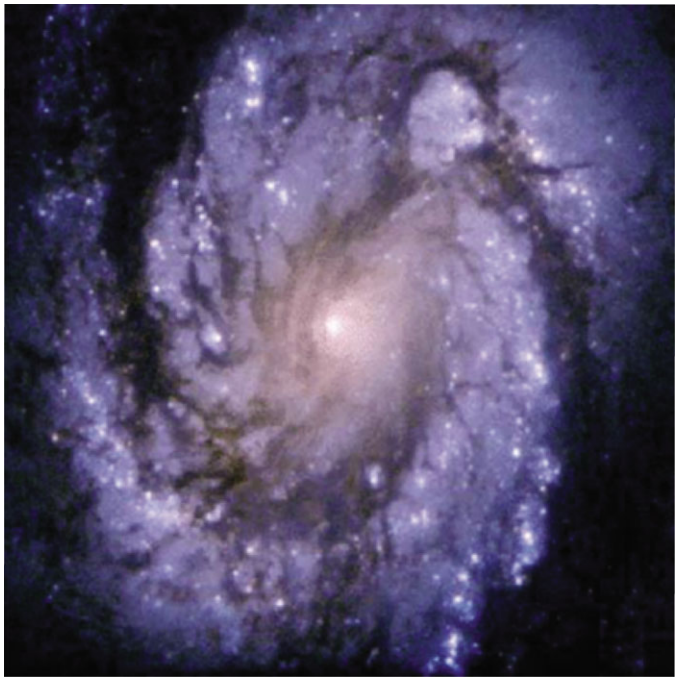

Figure 1. Photograph of galaxy M100.
(http://nssdc.gsfc.nasa.gov/photo_gallery/photogallery-astro-galaxy.html#galaxies)

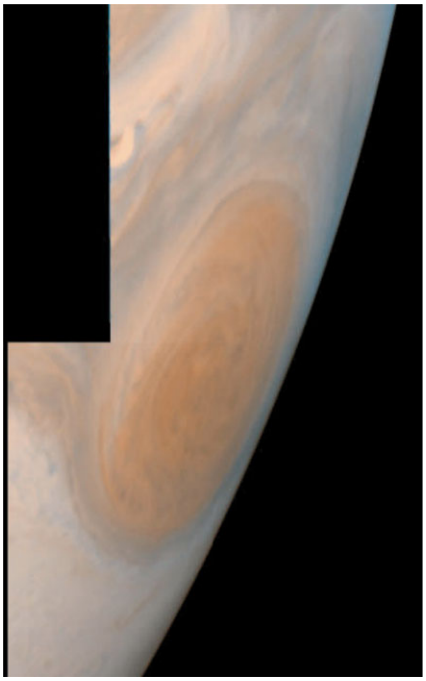

Figure 2. Photograph of Great Red Spot on Jupiter.
(http://nssdc.gsfc.nasa.gov/photo_gallery/photogallery-jupiter.html#spot)

Figure 3. Photograph of tornado. (http//www.photolib.noaa.gov/historic/nws/)

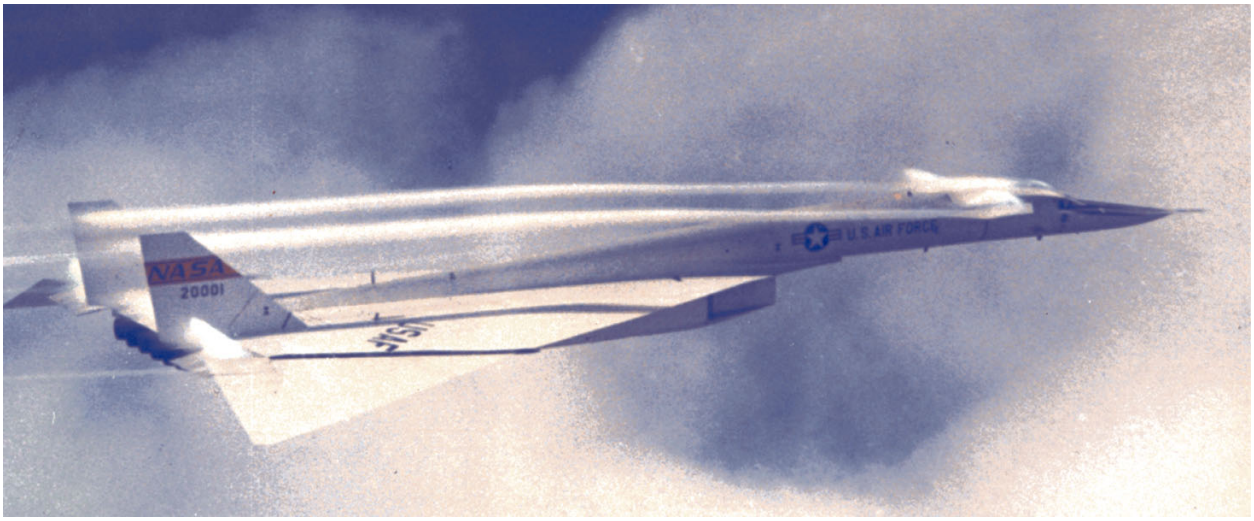

Figure 4. Photograph of XB-70 in supersonic flight.

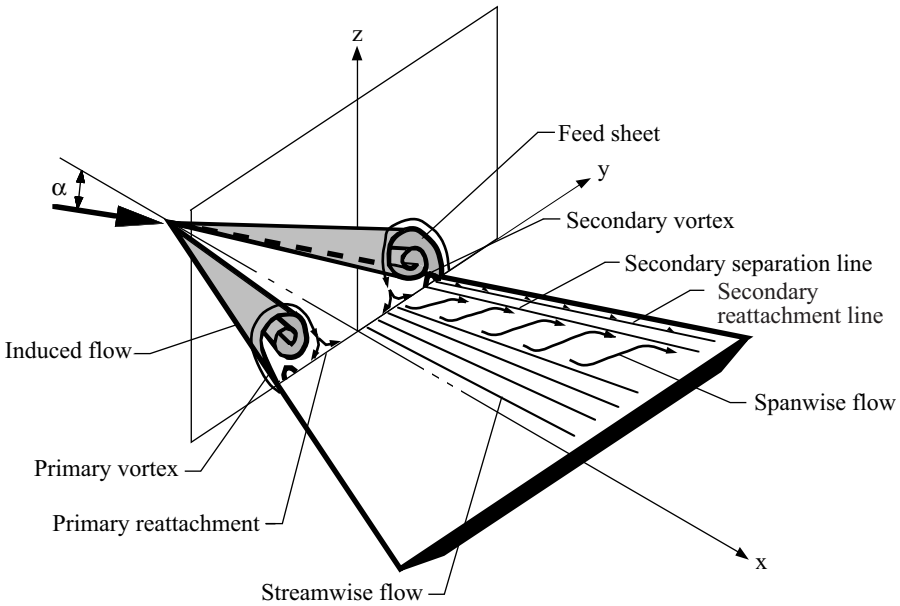

Figure 5. Sketch of sharp leading-edge, wing-vortex flow on delta wing at angle of attack.

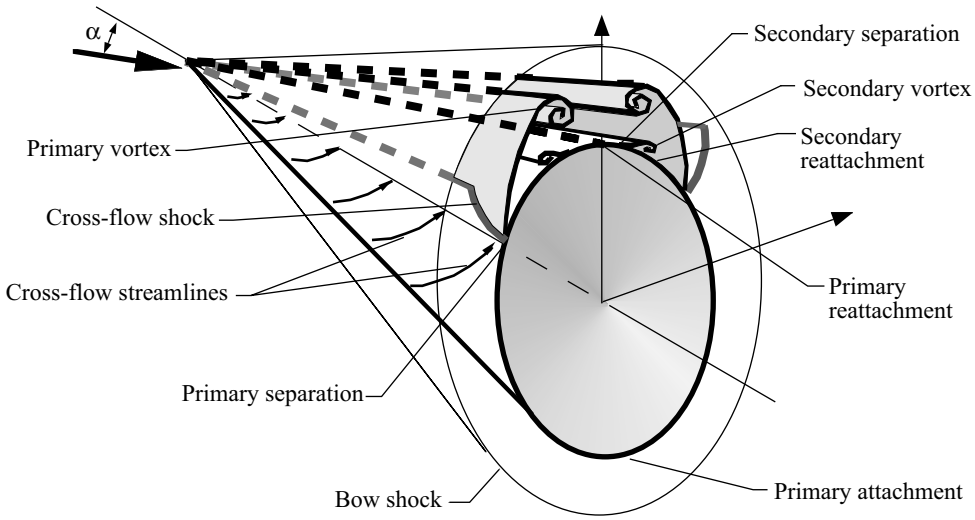

Figure 6. Sketch of smooth-wall vortex flow on conical forebody at angle of attack.

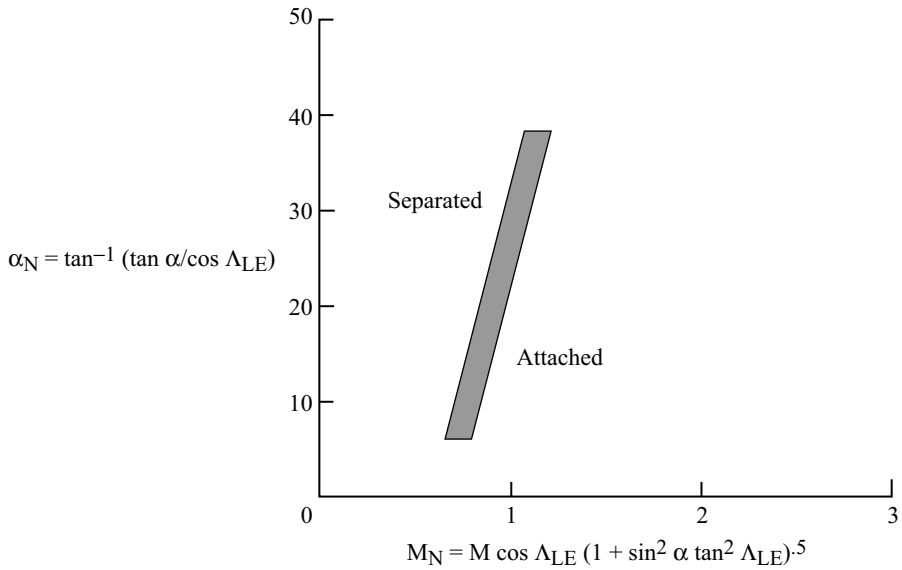

Figure 7. Stanbrook-Squire lee-side vortex flow classification for delta wings.

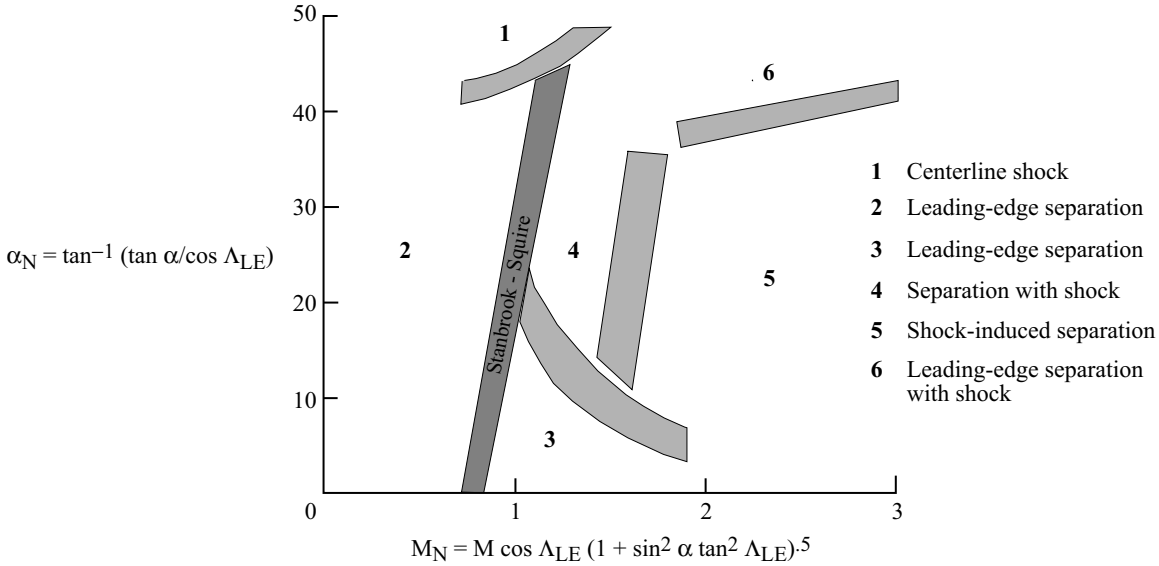

Figure 8. Stanbrooke-Peake lee-side vortex flow classification for delta wings.

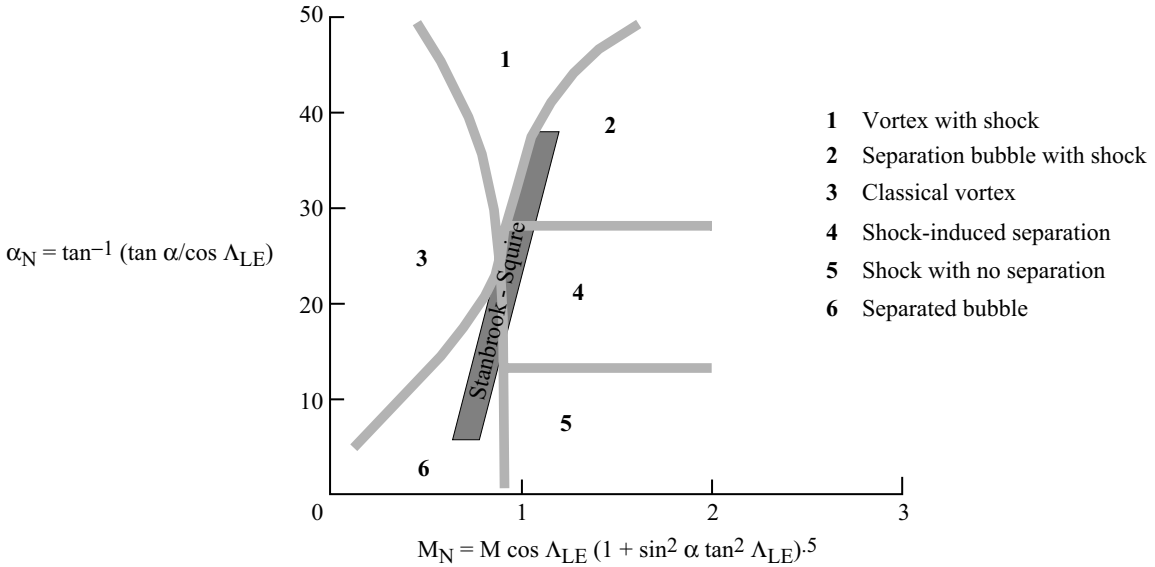

Figure 9. Miller-Wood lee-side vortex flow classification for delta wings.

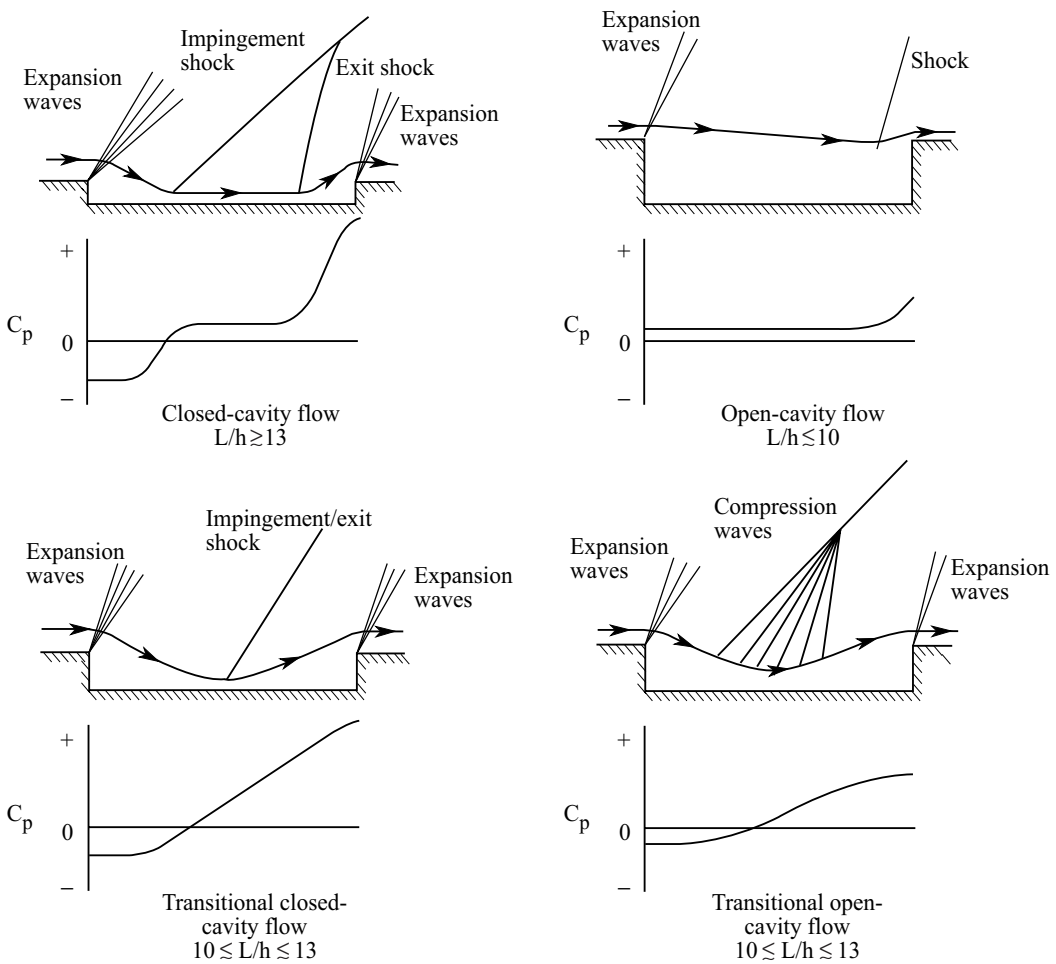

Figure 10. Flow-field sketches and typical pressure distributions of rectangular box cavities at supersonic speeds (ref. 147).

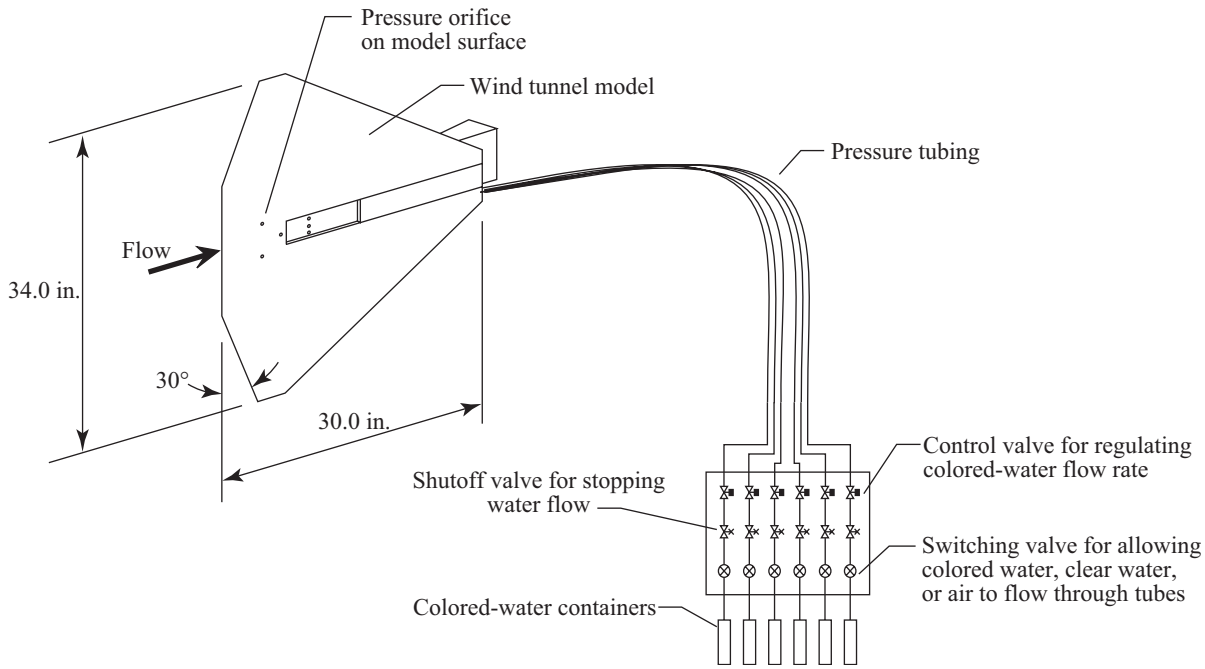

(a) Schematic of colored-water flow apparatus.

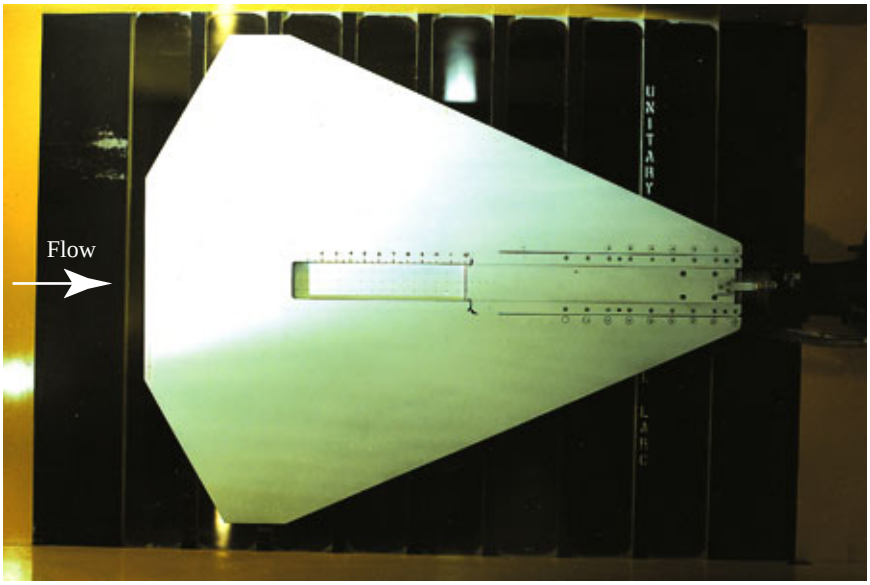

(b) Photograph of flat plate model mounted in wind tunnel.

Figure 11. Colored-water flow experimental apparatus (ref. 148).

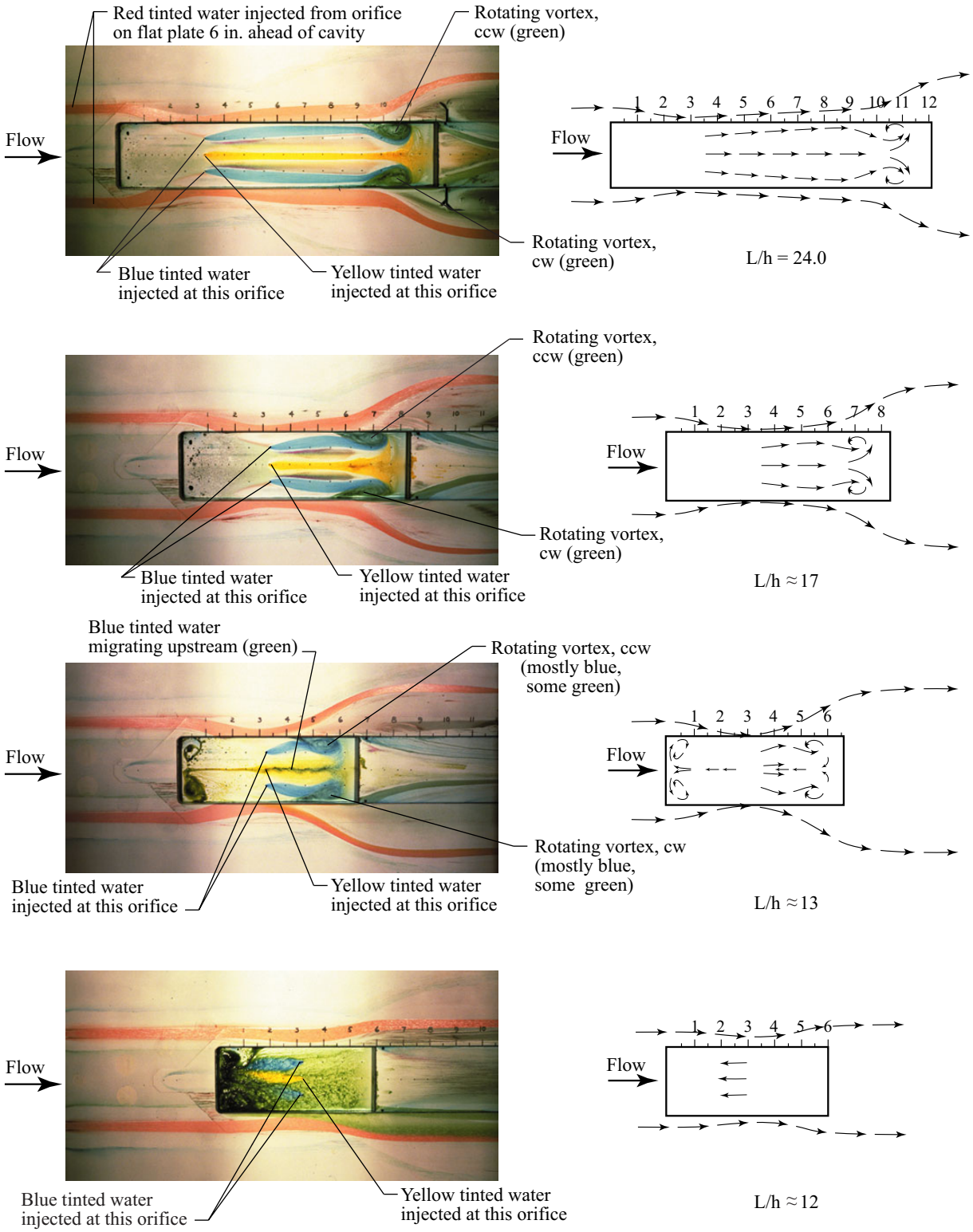

Figure 12. Visualization of surface flow fields on cavity floor at $M_\infty = 1.50$ using colored-water technique (ref. 148); cavity height = 0.5 in.

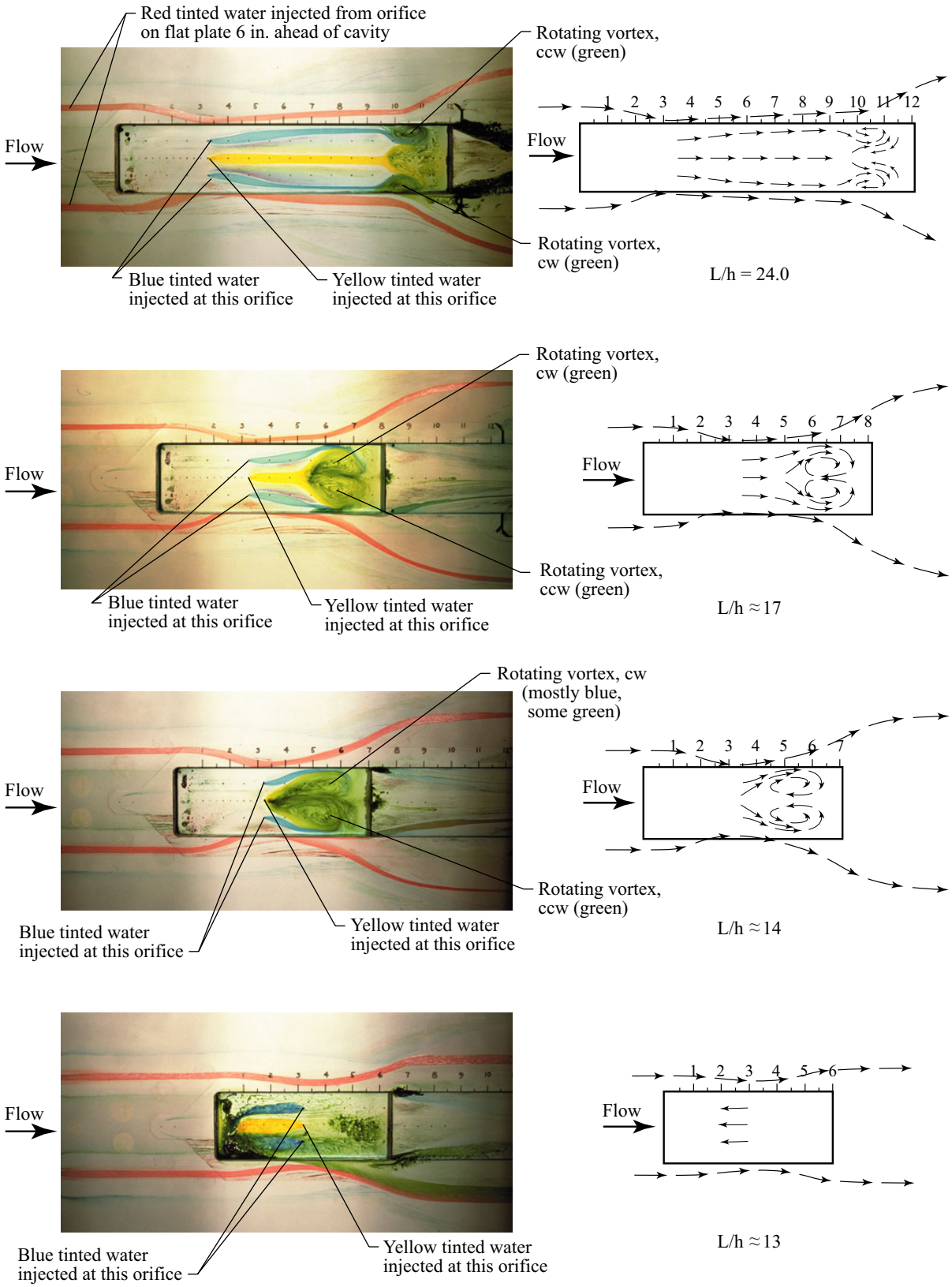

Figure 13. Visualization of surface flow fields on cavity floor at $M_\infty = 2.16$ using colored-water technique (ref. 148); cavity height = 0.5 in.

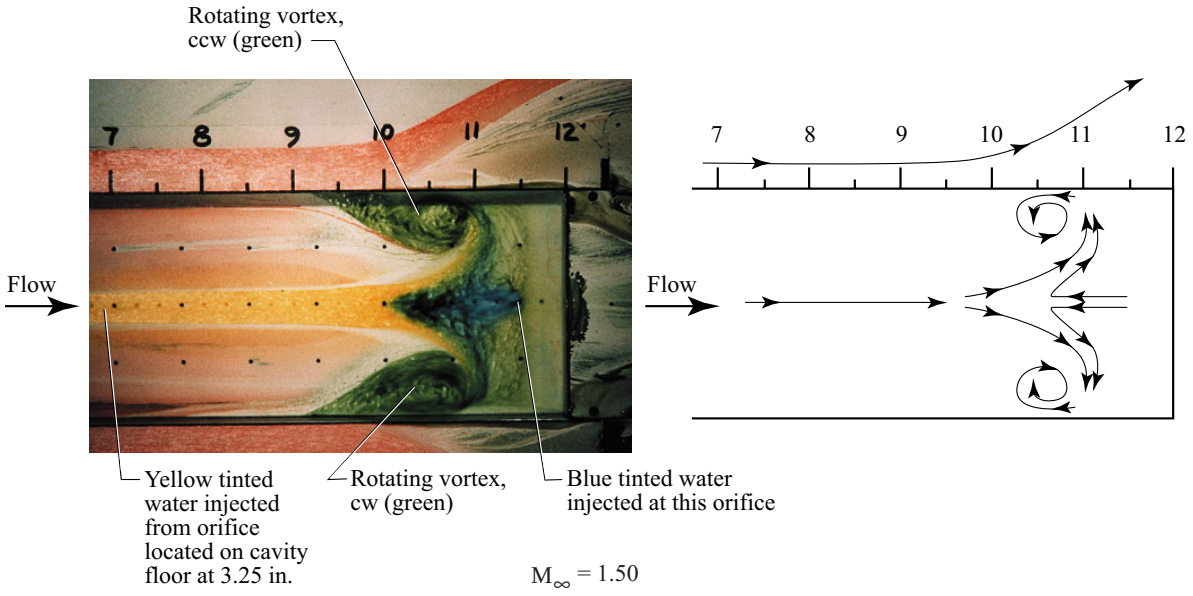

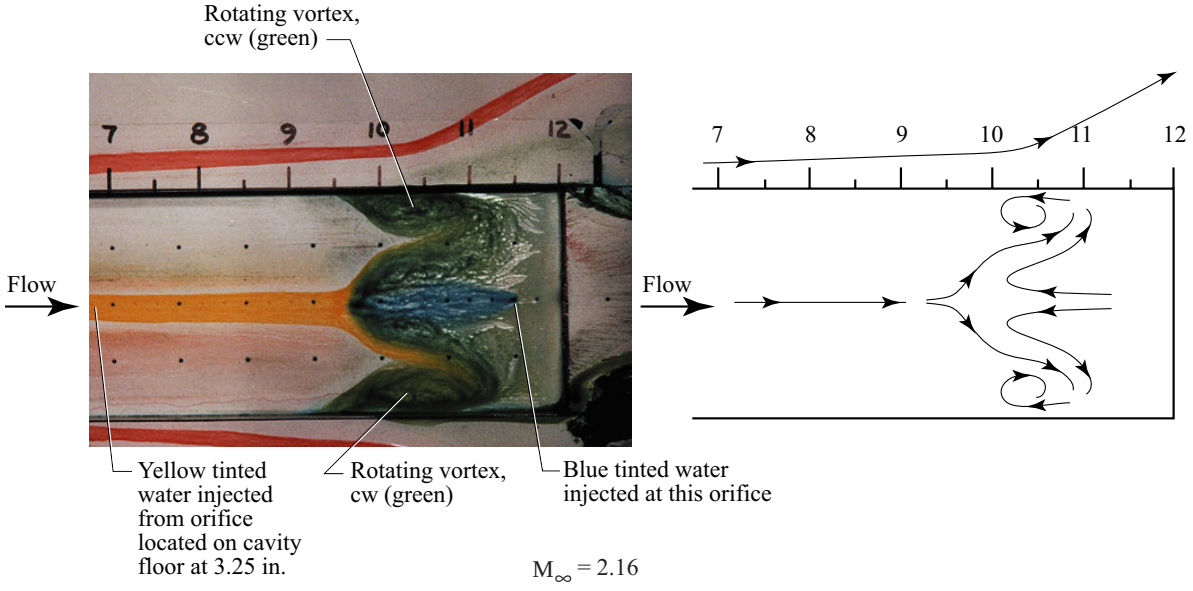

Figure 14. Visualization of cavity floor field at rear of cavity; L/h = 24.0, cavity height = 0.5 in.

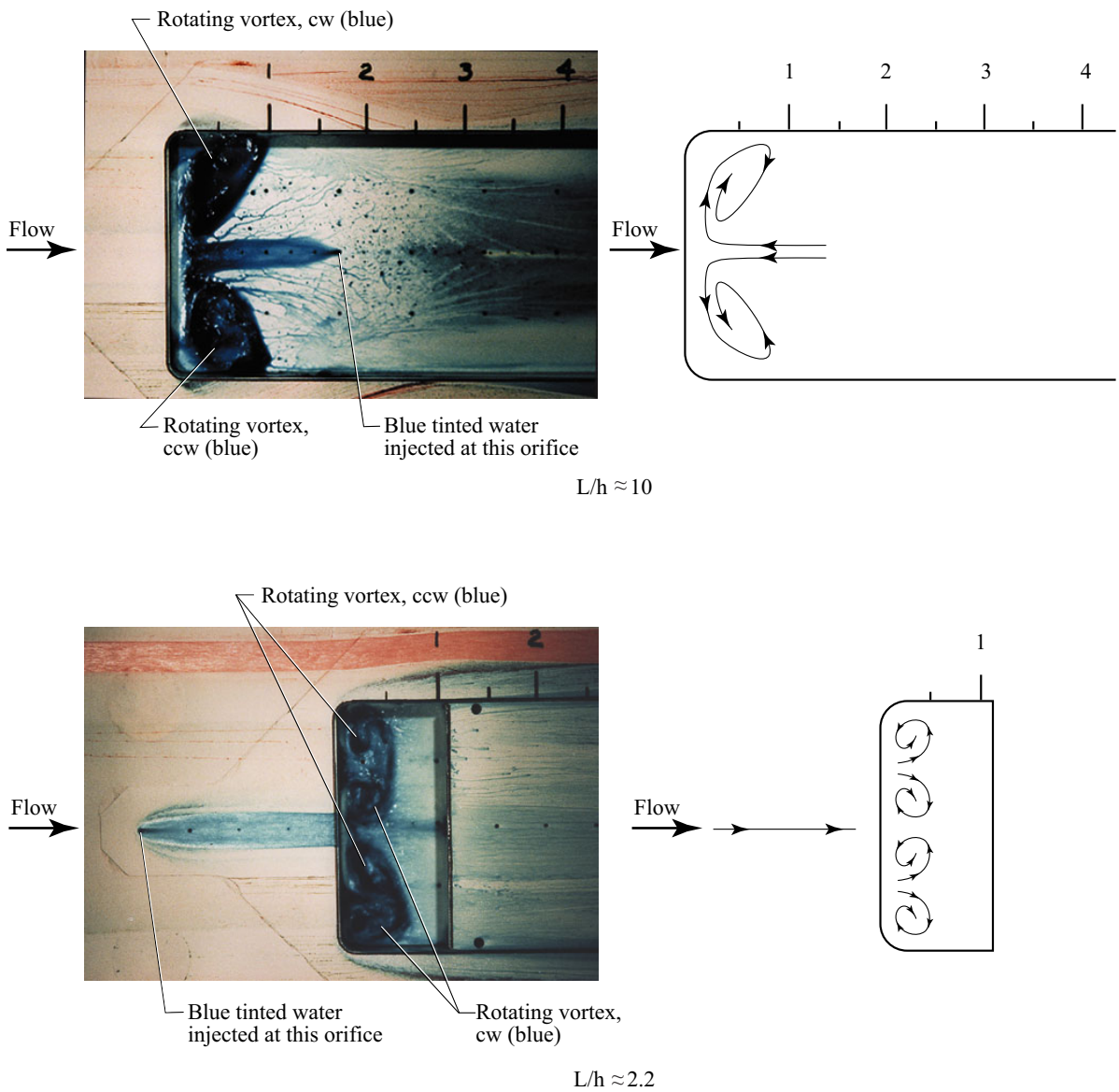

Figure 15. Visualization of cavity flow field at front of cavity at $M_\infty = 1.50$; cavity height = 0.5 in.

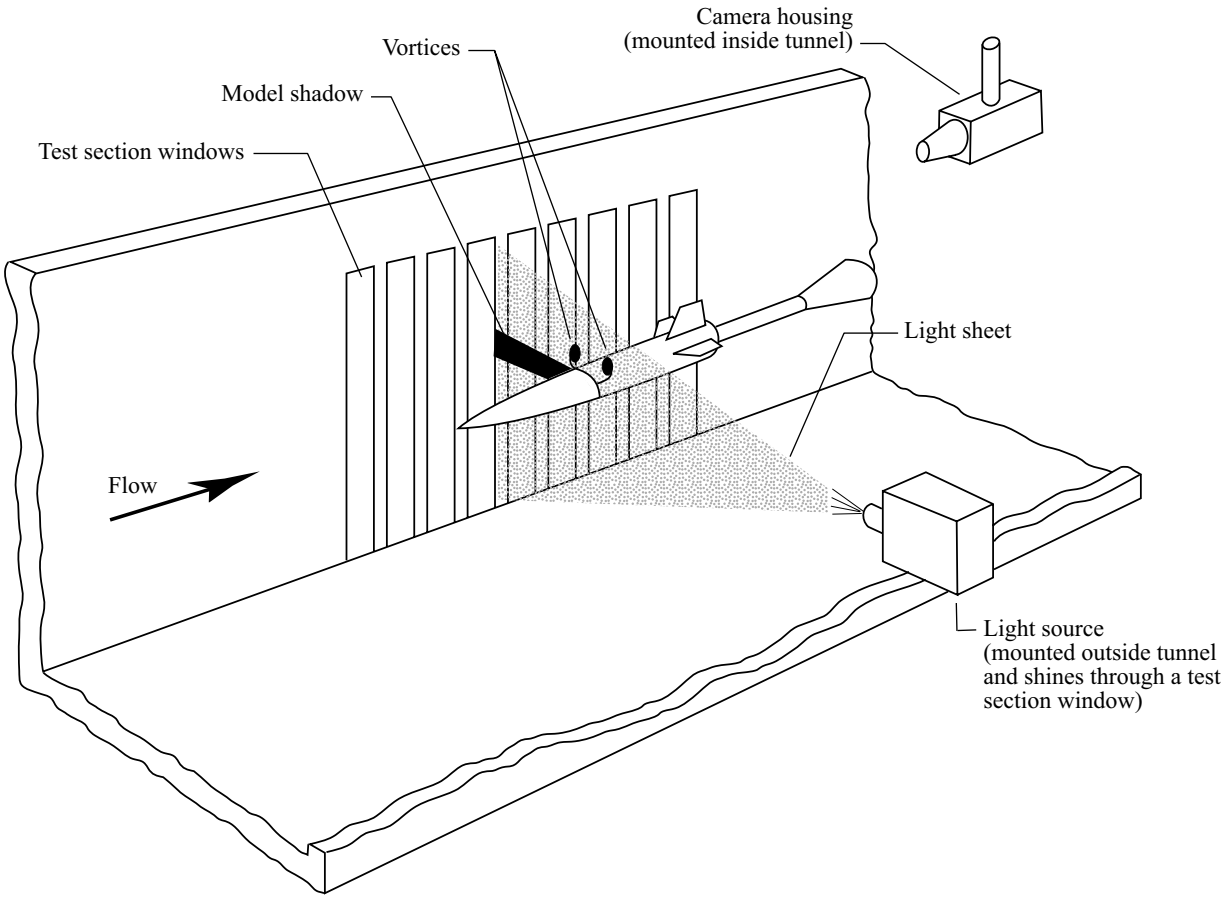

Figure 16. Vapor-screen apparatus setup in Langley UPWT (ref. 150).

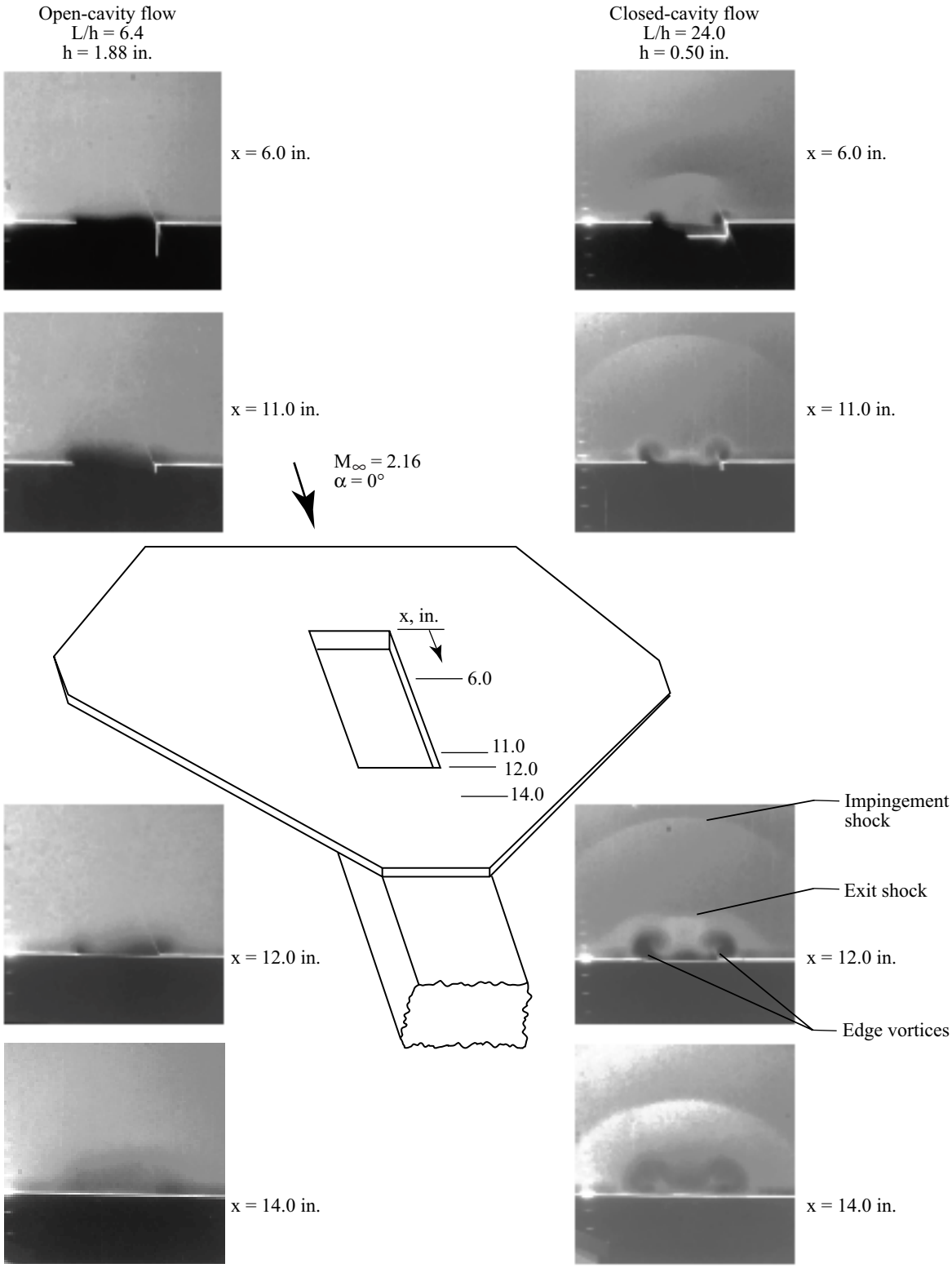

Figure 17. Vapor-screen photographs of open- and closed-cavity flow (ref. 146).

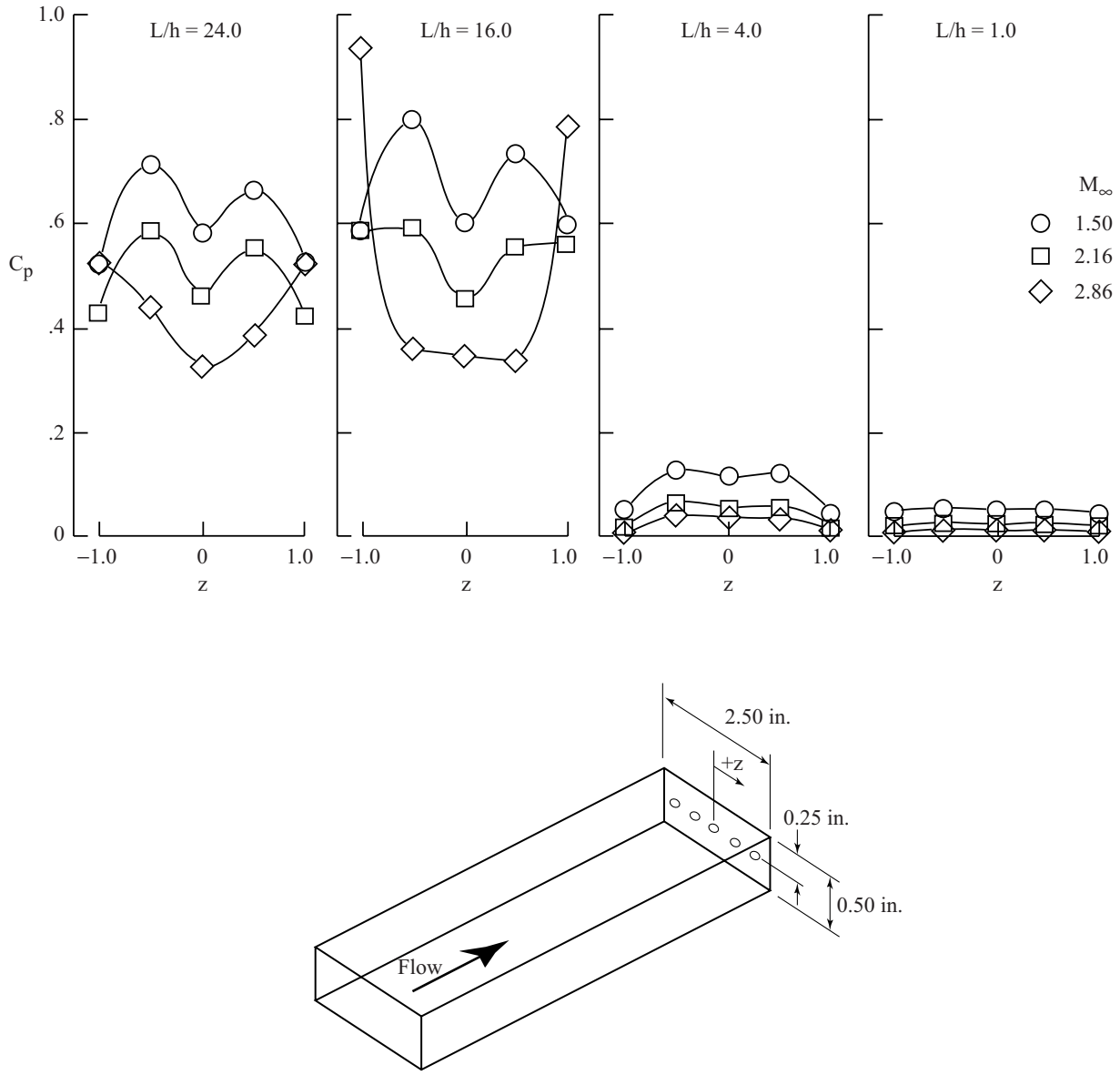

Figure 18. Lateral pressure distribution measured on cavity rear face (ref. 140); cavity width = 2.5 in.

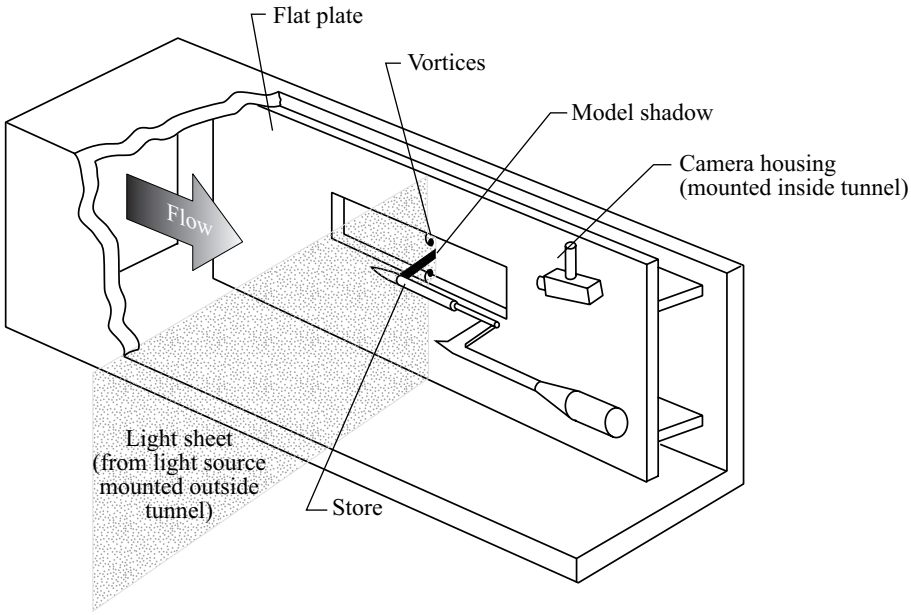

Figure 19. Vapor-screen setup for store separation tests in Langley UPWT (ref. 151).

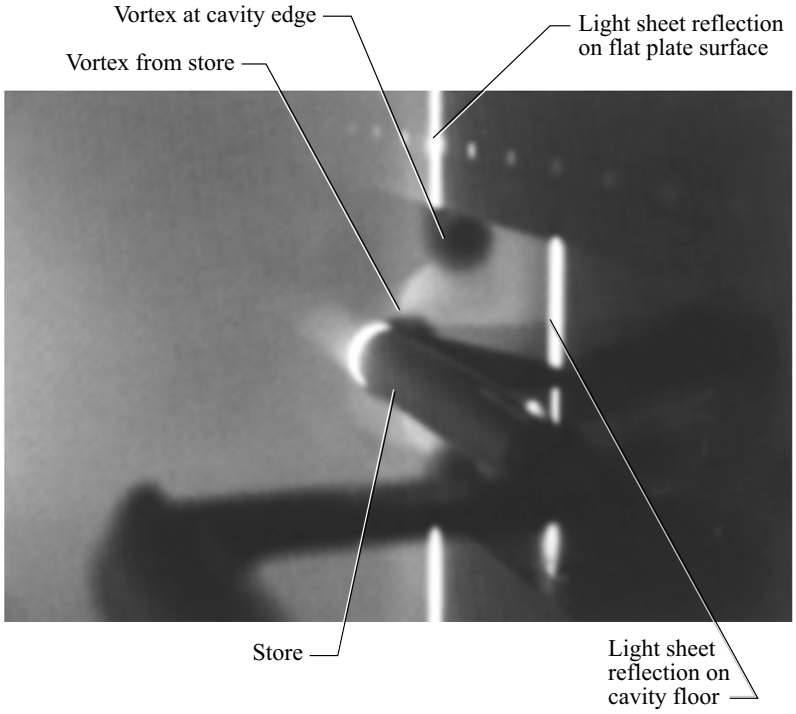

(a) Doors off.

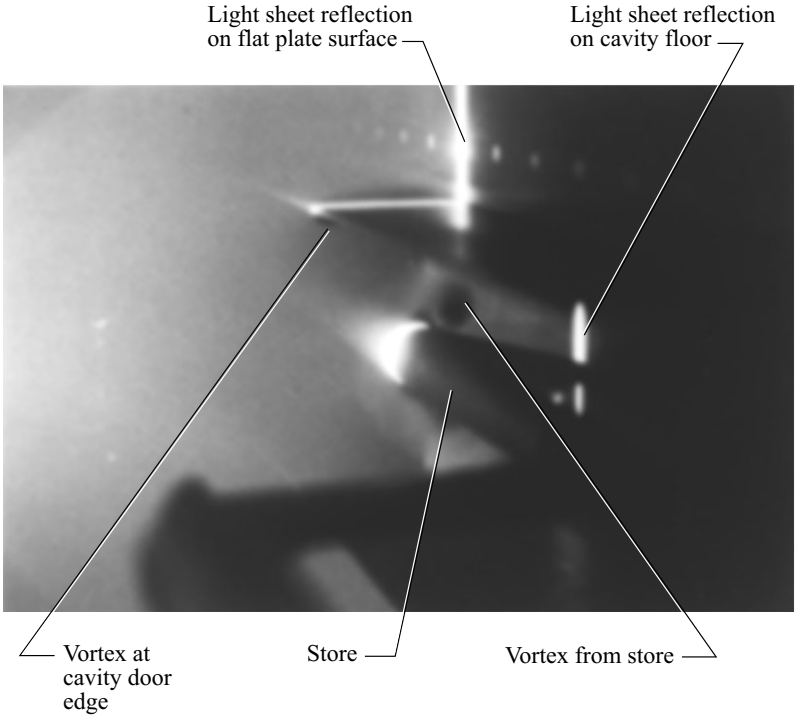

(b) Doors on.

Figure 20. Vapor-screen photographs of store in vicinity of cavity with and without doors at $M_\infty = 2.65$, $L/h = 12.07$ (ref. 151).

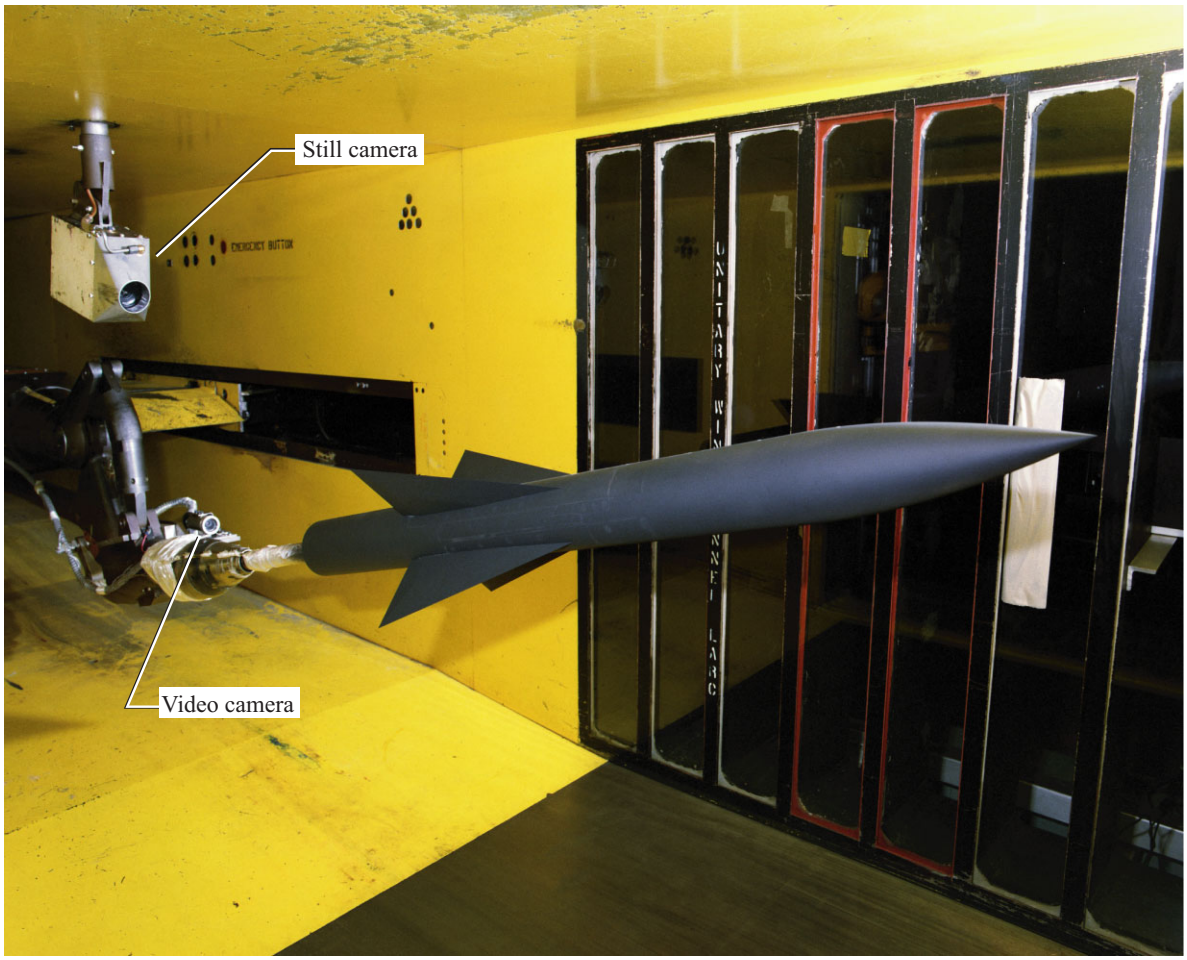

Figure 21. Photograph of wing-body missile model in Langley UPWT (ref. 152).

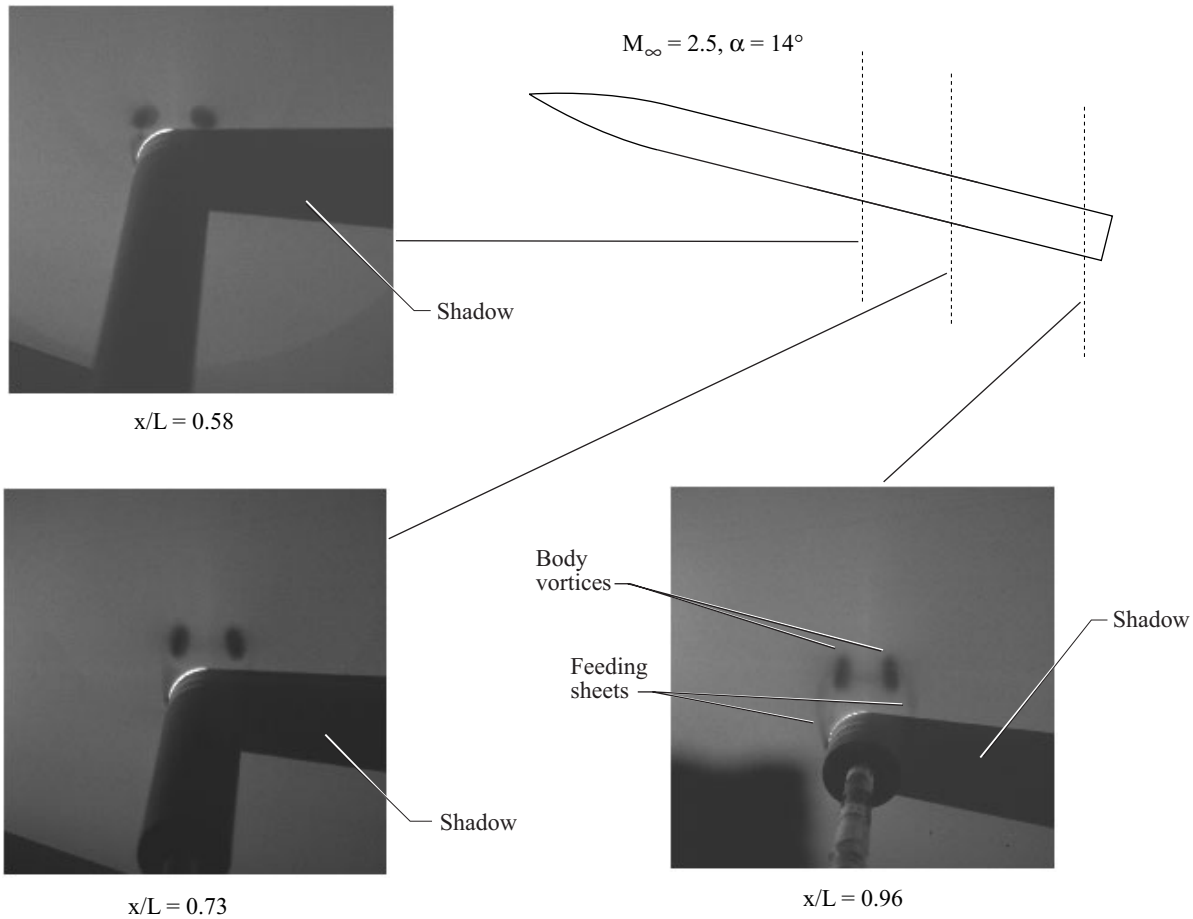

Figure 22. Vapor-screen photographs (views looking forward) showing vortex development on body alone at $M_\infty = 2.5$ and $\alpha = 14°$ (ref. 152).

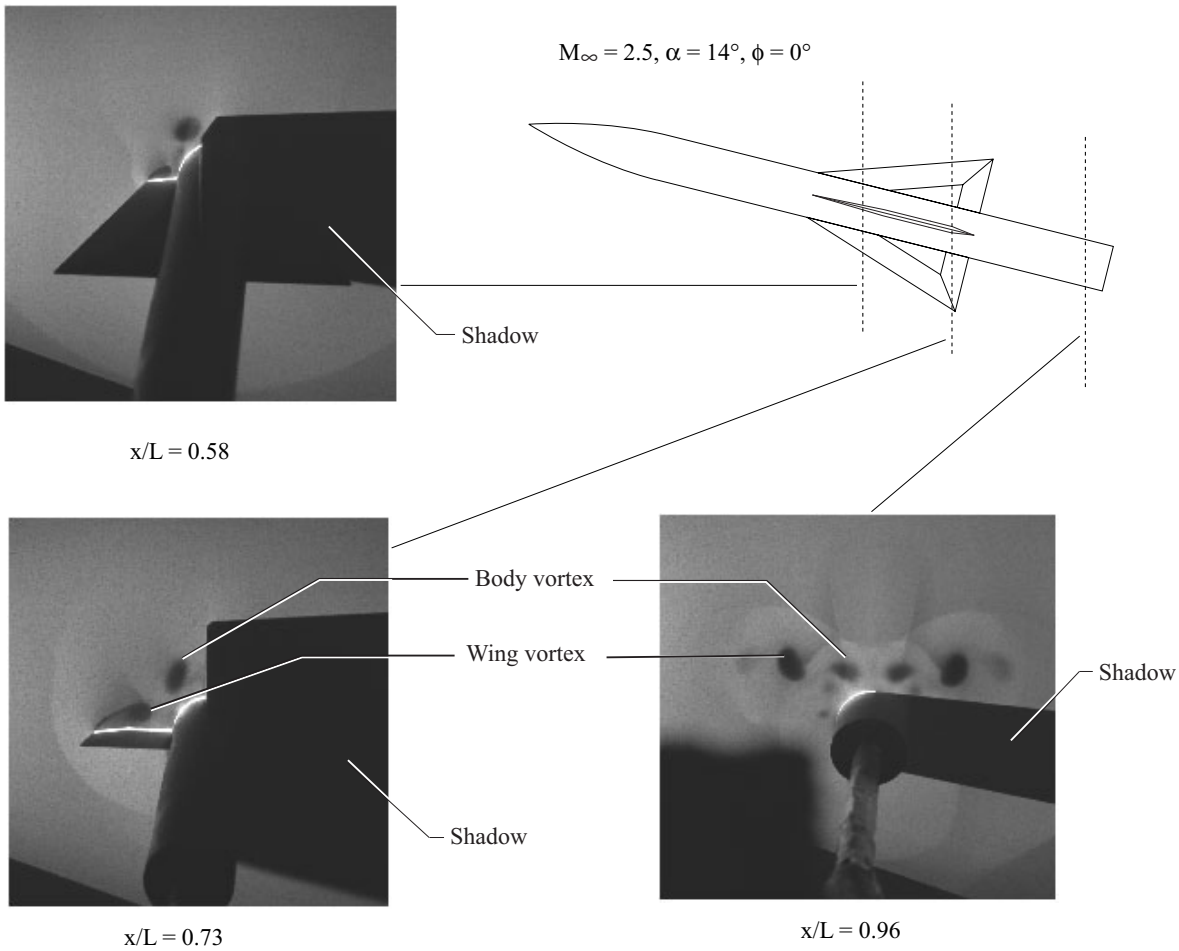

Figure 23. Vapor-screen photographs (views looking forward) showing vortex development on body-wing missile model at $M_\infty = 2.5$ and $\alpha = 14°$ (ref. 152).

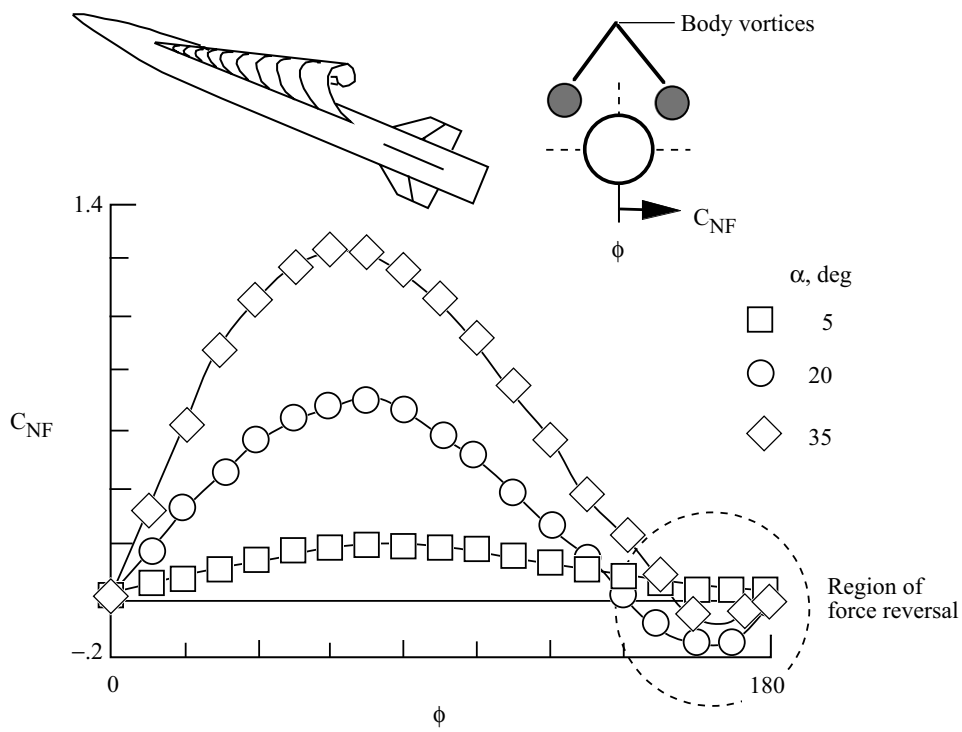

Figure 24. Plot of fin normal force coefficient as function of fin roll position at $M_\infty = 2.0$ (ref. 153).

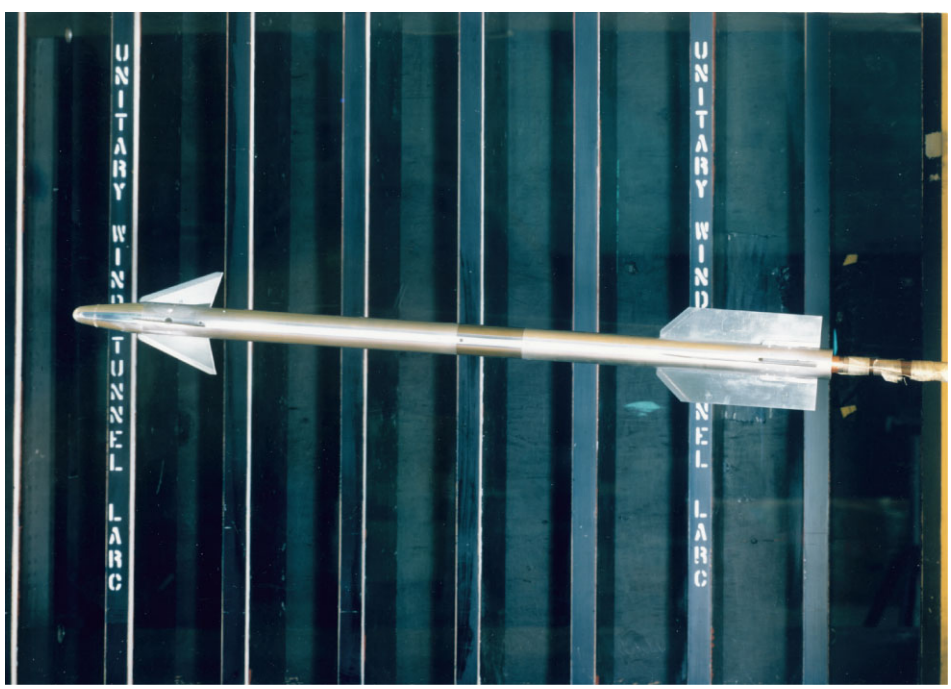

Figure 25. Photograph of variant of Sidewinder missile model in Langley UPWT (ref. 154).

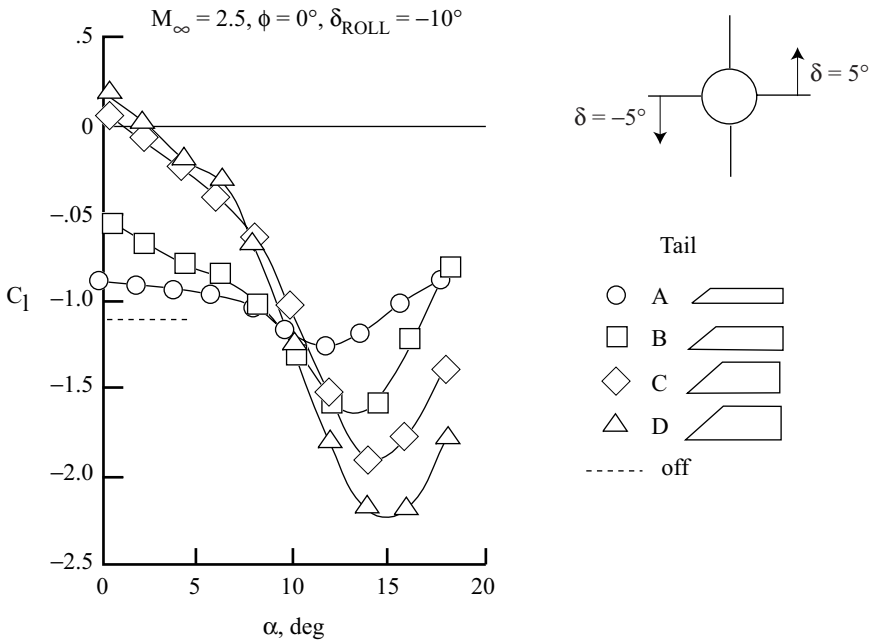

Figure 26. Effect of tail span on Sidewinder missile variant rolling moment at $M_\infty = 2.5$ (ref. 154).

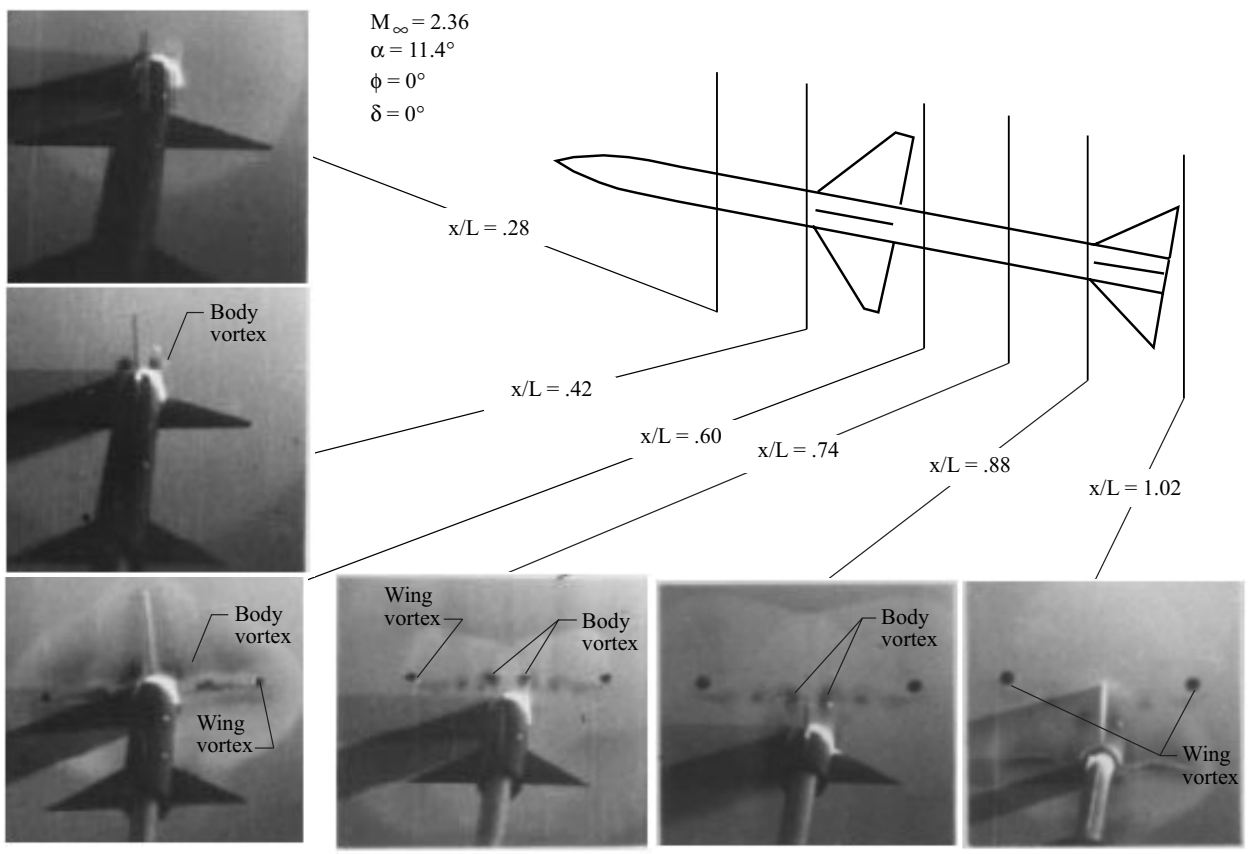

Figure 27. Vapor-screen photographs (views looking forward) showing vortex development on Sparrow missile at $M_\infty = 2.36$ and $\alpha = 11.4°$ (ref. 116).

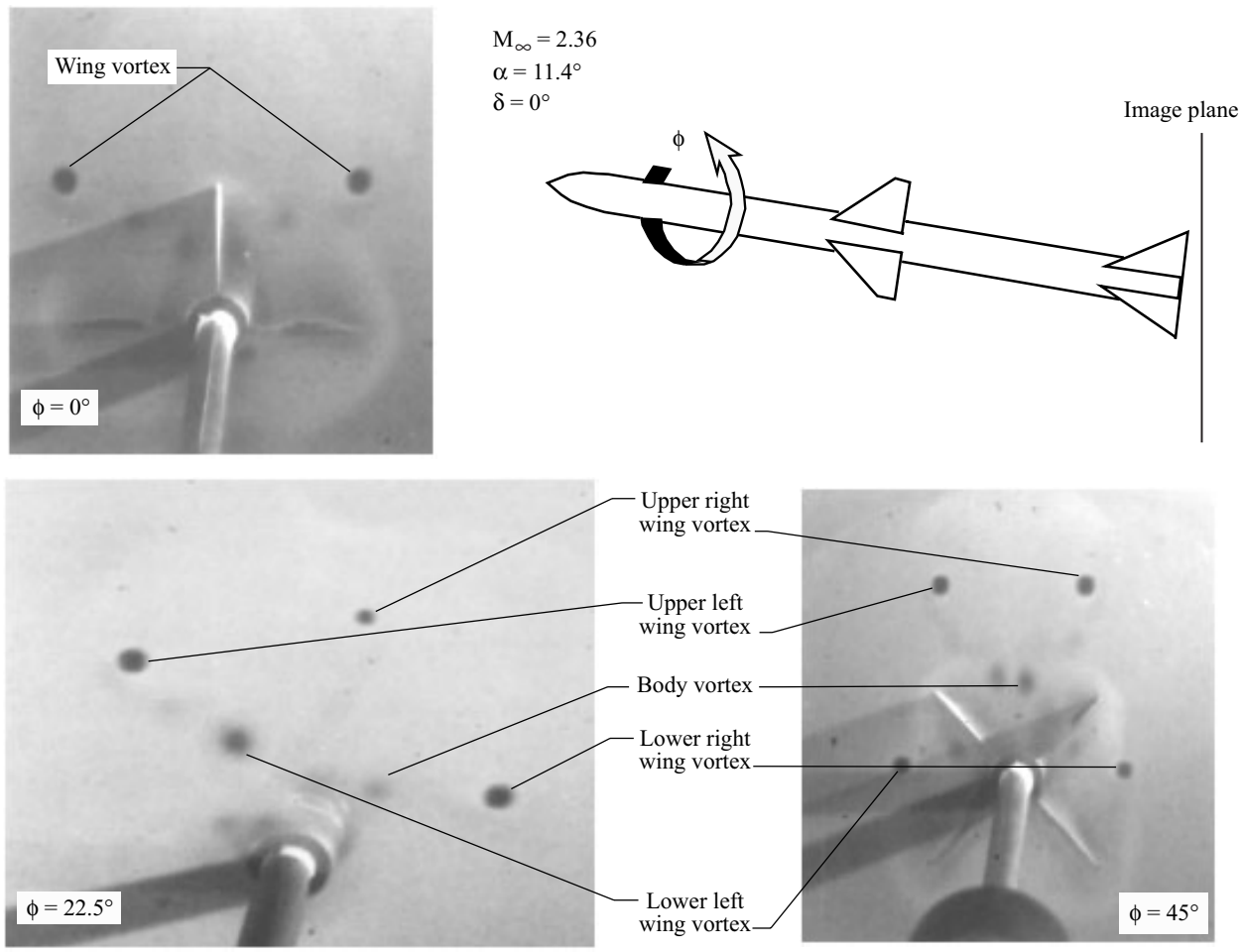

Figure 28. Vapor-screen photographs (views looking forward) showing effect of roll angle on vortex patterns for Sparrow missile at $M_\infty = 2.36$ and $\alpha = 11.4°$ (ref. 116).

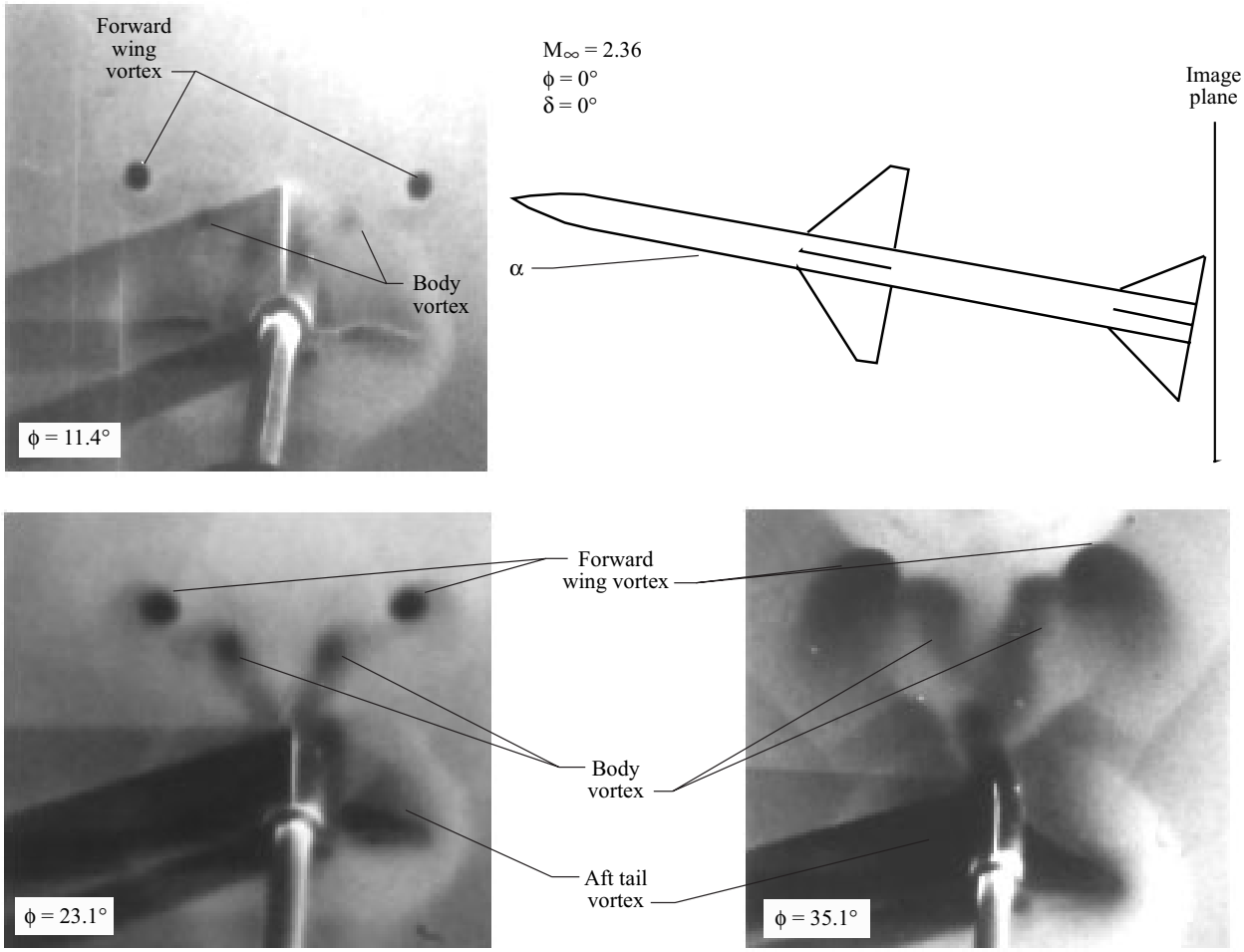

Figure 29. Vapor-screen photographs (views looking forward) showing effect of angle of attack on Sparrow missile vortex patterns at $M_\infty = 2.36$ and $\phi = 0°$ (ref. 116).

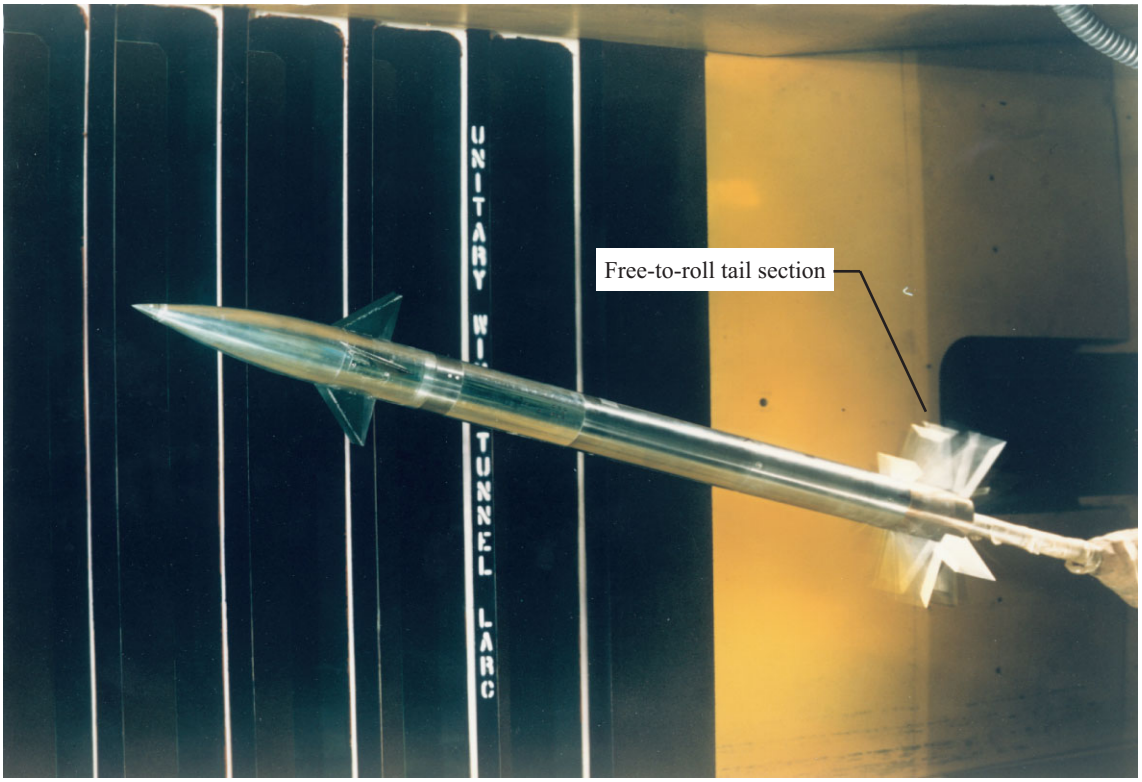

Figure 30. Photograph of Free Rolling Tail missile model in Langley UPWT (ref. 155).

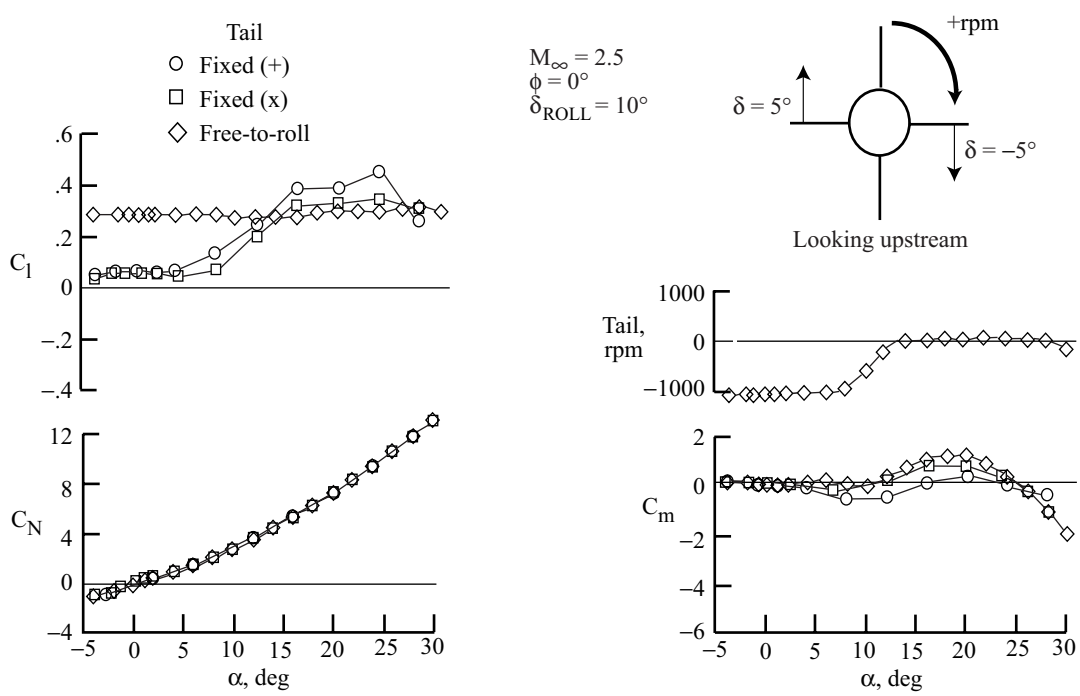

Figure 31. Effects of free-to-roll tail on roll control at $M_\infty = 2.5$ (ref. 155).

Figure 32. Photograph of sharp-nose 3-to-1 elliptical body model in Langley UPWT (ref. 117).

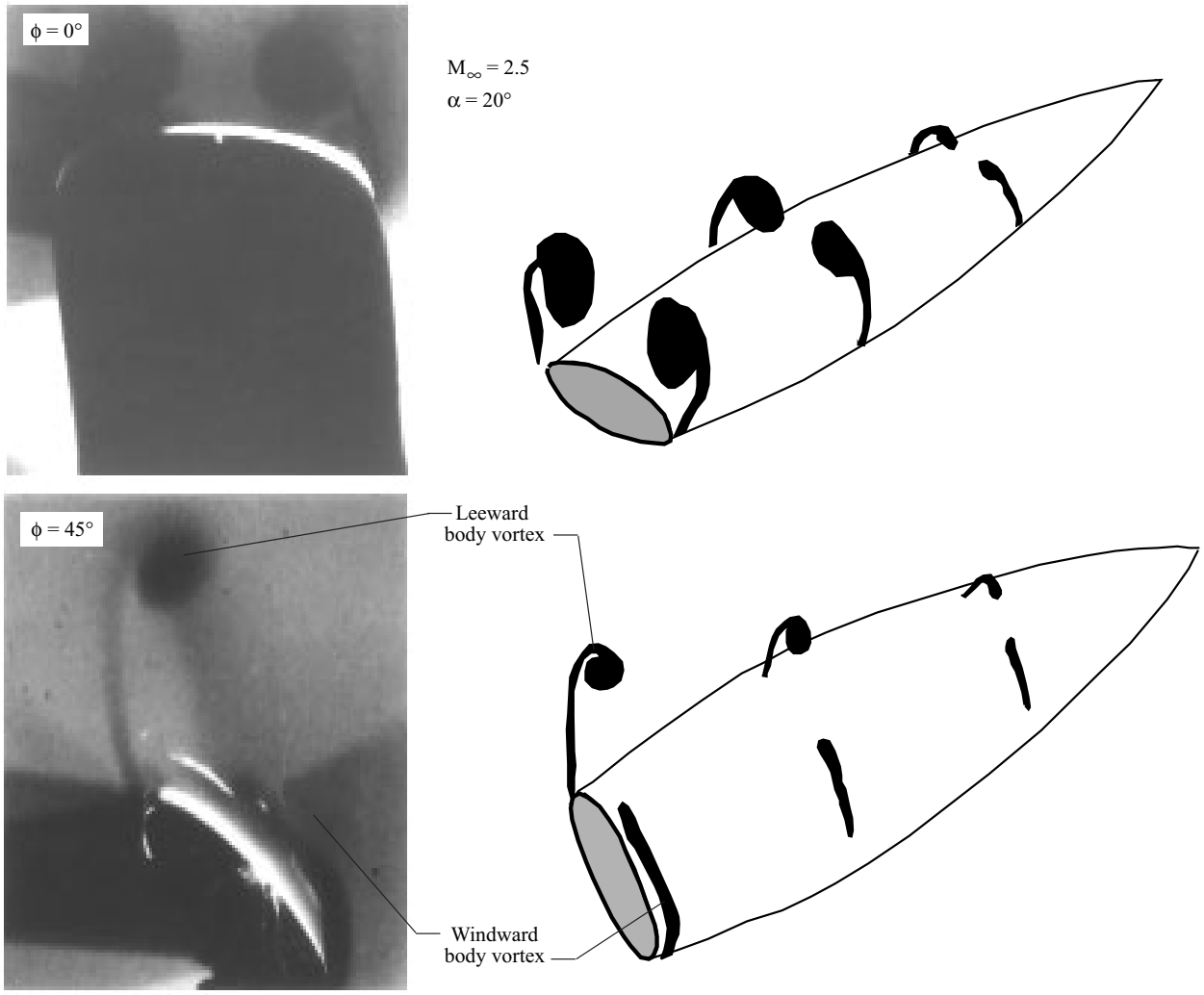

Figure 33. Vapor-screen photographs (views looking forward) showing effect of roll angle on vortex patterns for sharp-nose elliptical body at $M_\infty = 2.5$ and $\alpha = 20°$ (ref. 117).

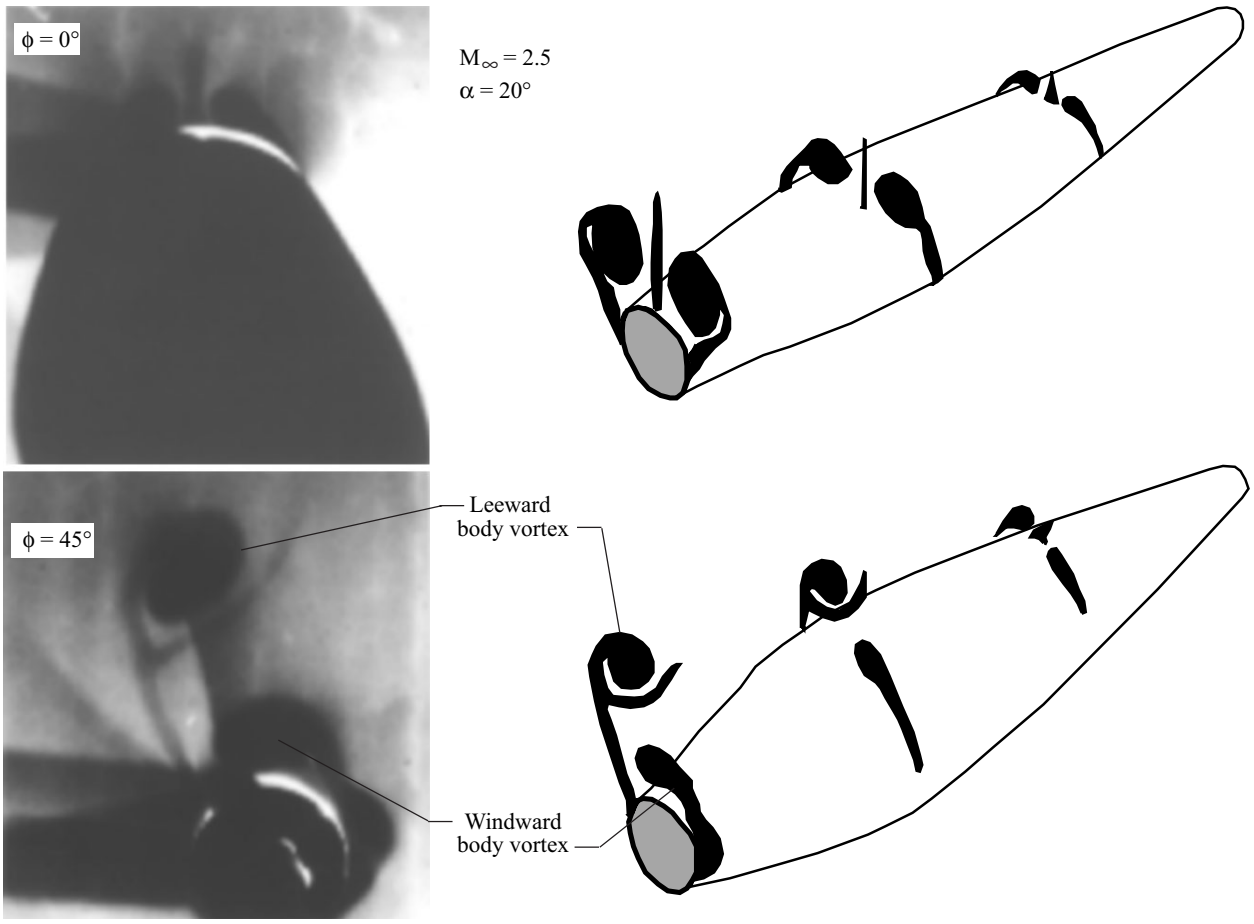

Figure 34. Vapor-screen photographs (views looking forward) showing effect of roll angle on vortex patterns for blunt-nose elliptical body at $M_\infty = 2.5$ and $\alpha = 20°$ (ref. 117).

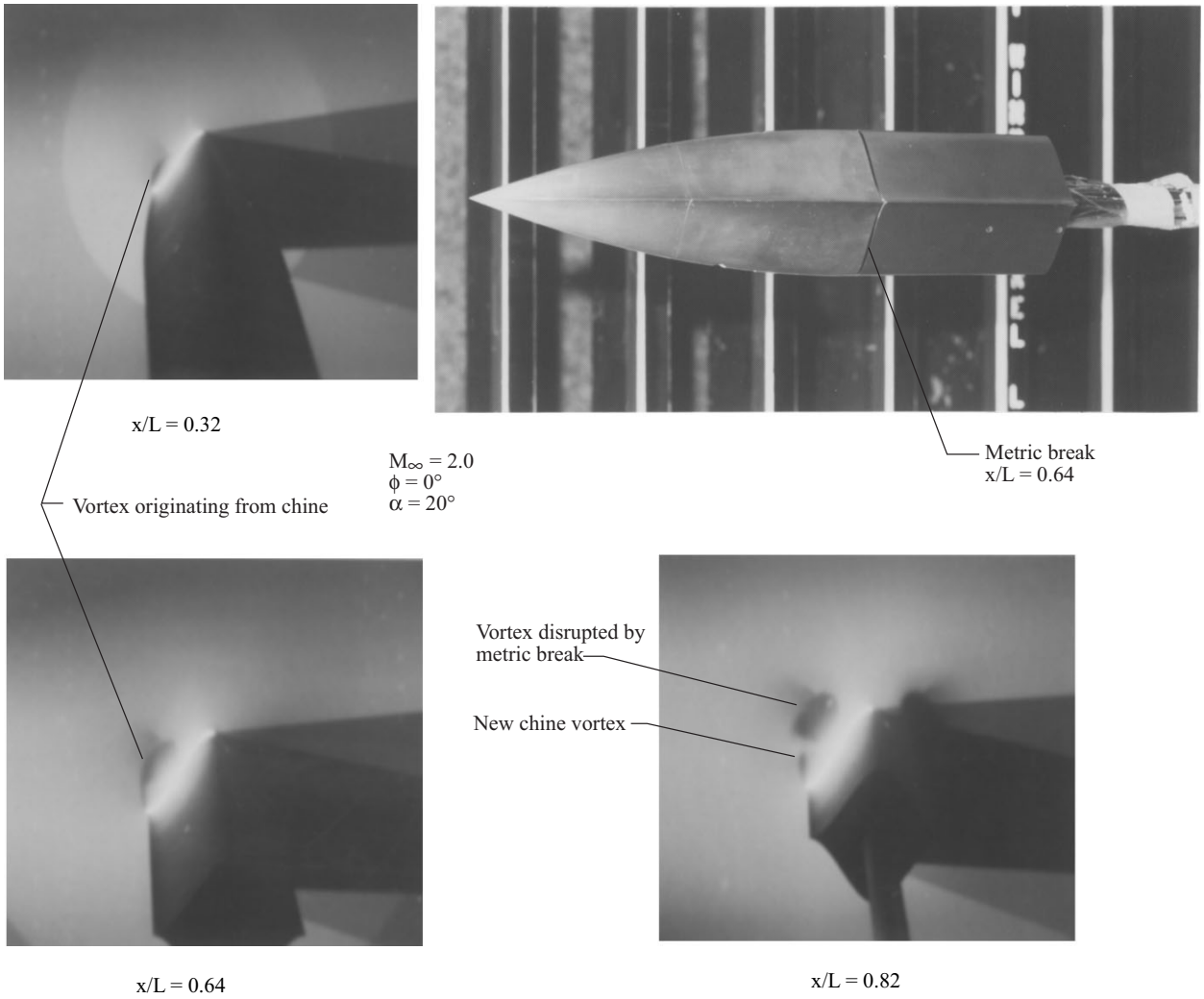

Figure 35. Vapor-screen photographs (views looking forward) showing vortex patterns on chined body at $M_\infty = 2.0$ and $\alpha = 20°$ (ref. 138).

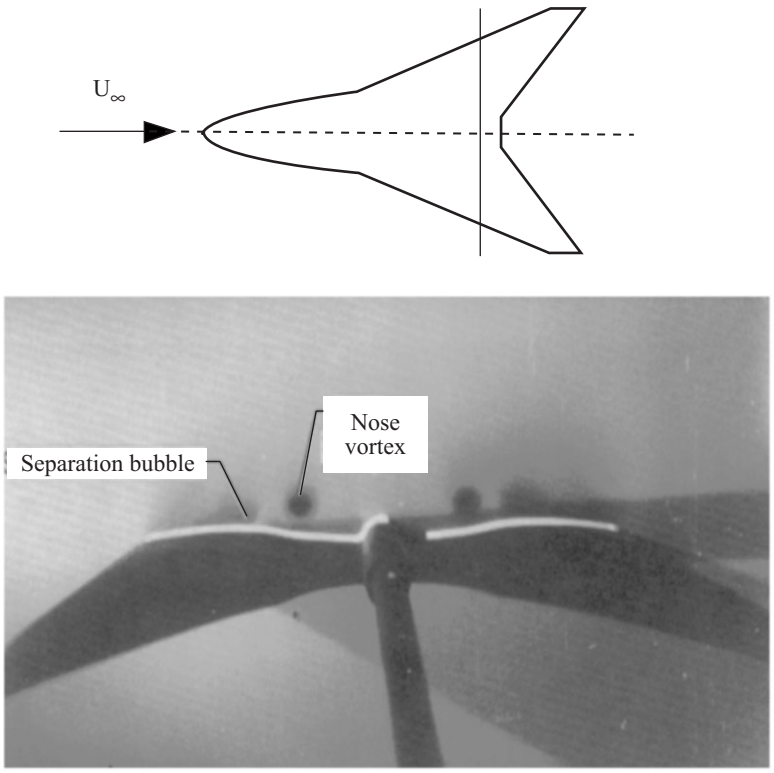

x/L = 0.76

Figure 36. Lee-side flow characteristics for ogee planform wing at Mach 2.4 and angle of attack of 5° (ref. 158).

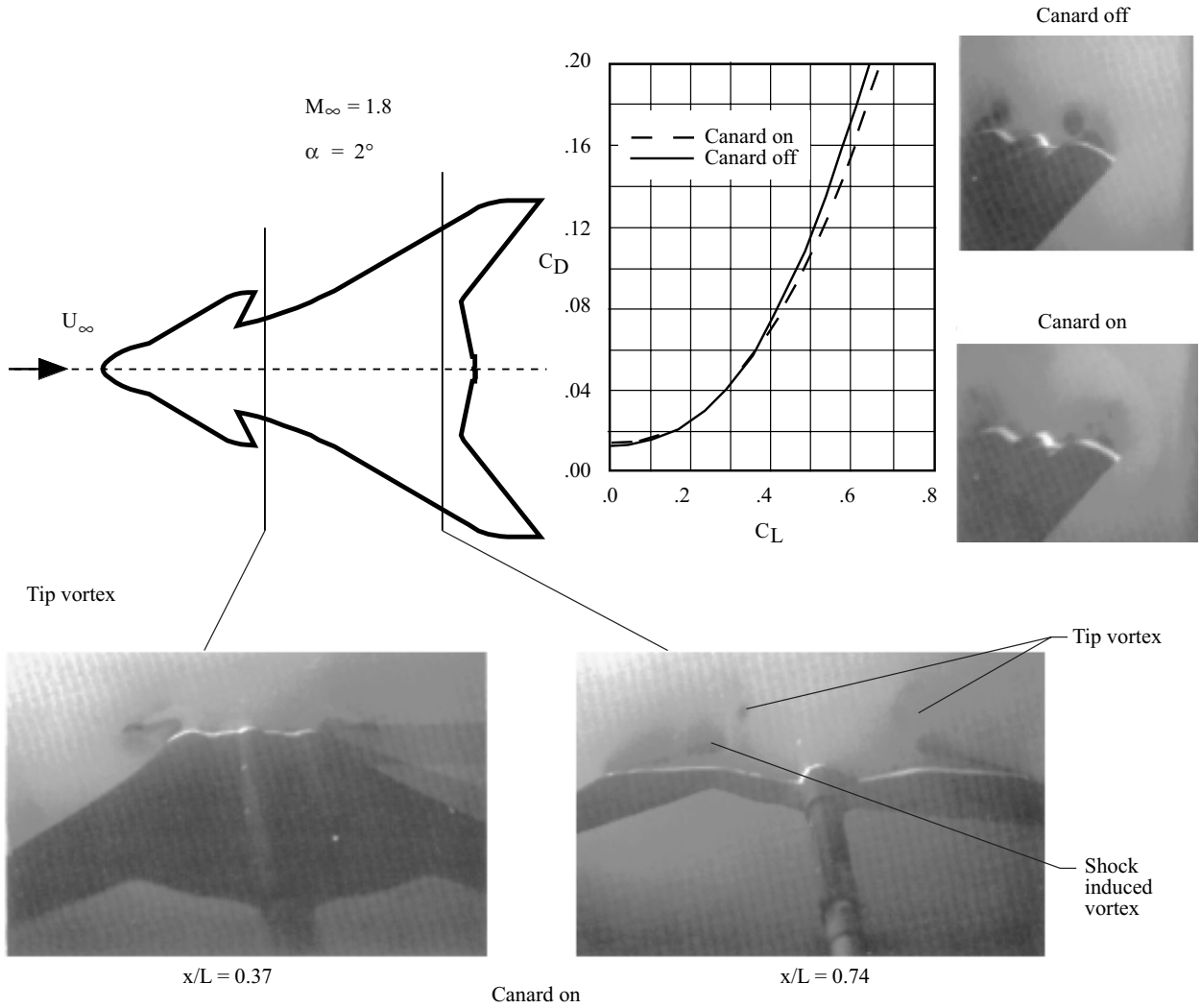

Figure 37. Lee-side flow characteristics for ogee planform wing with canard at Mach 1.8 and angle of attack of 12° (ref. 165).

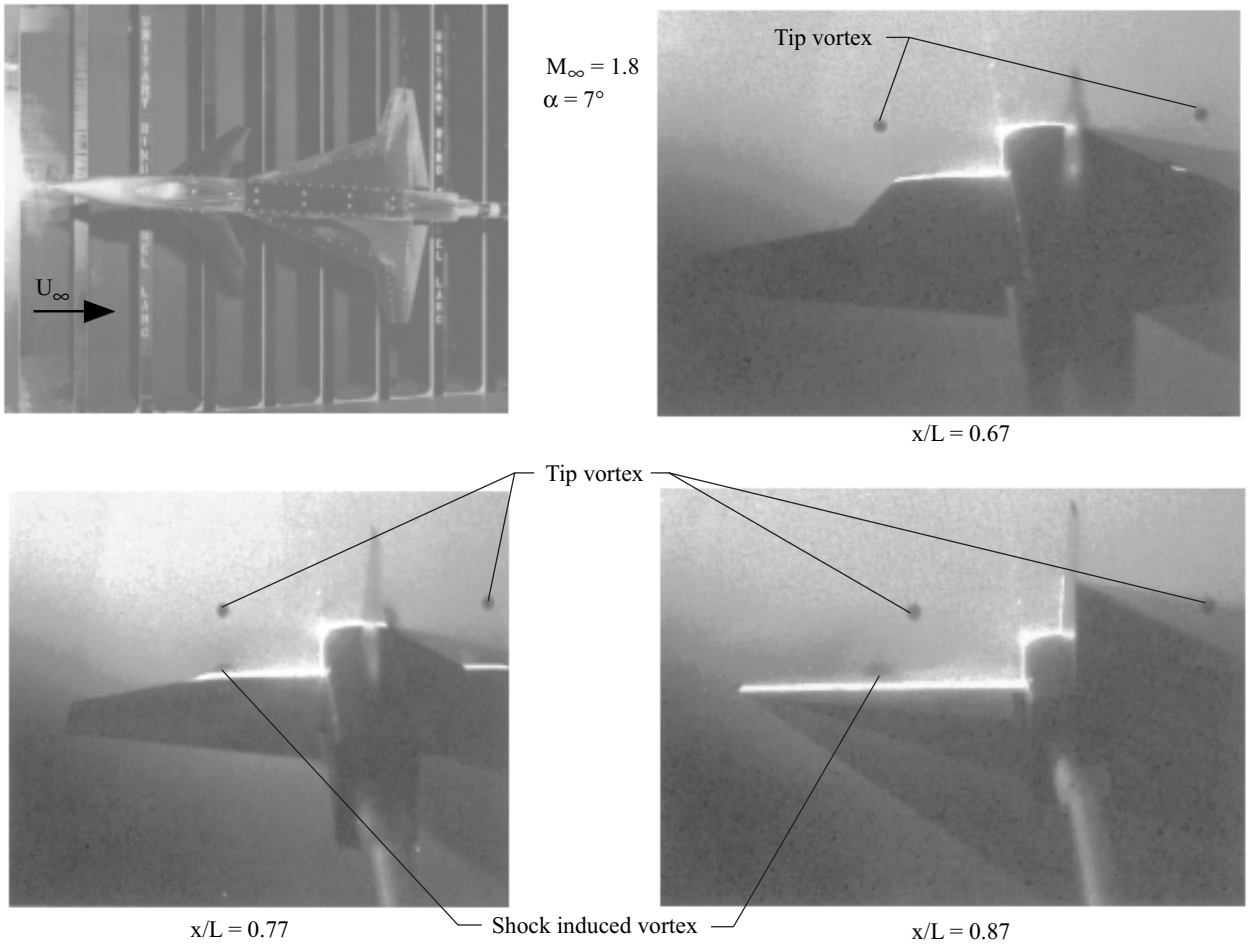

Figure 38. Lee-side flow characteristics for cranked delta planform wing with canard at Mach 1.8 and angle of attack of 7° (ref. 166).

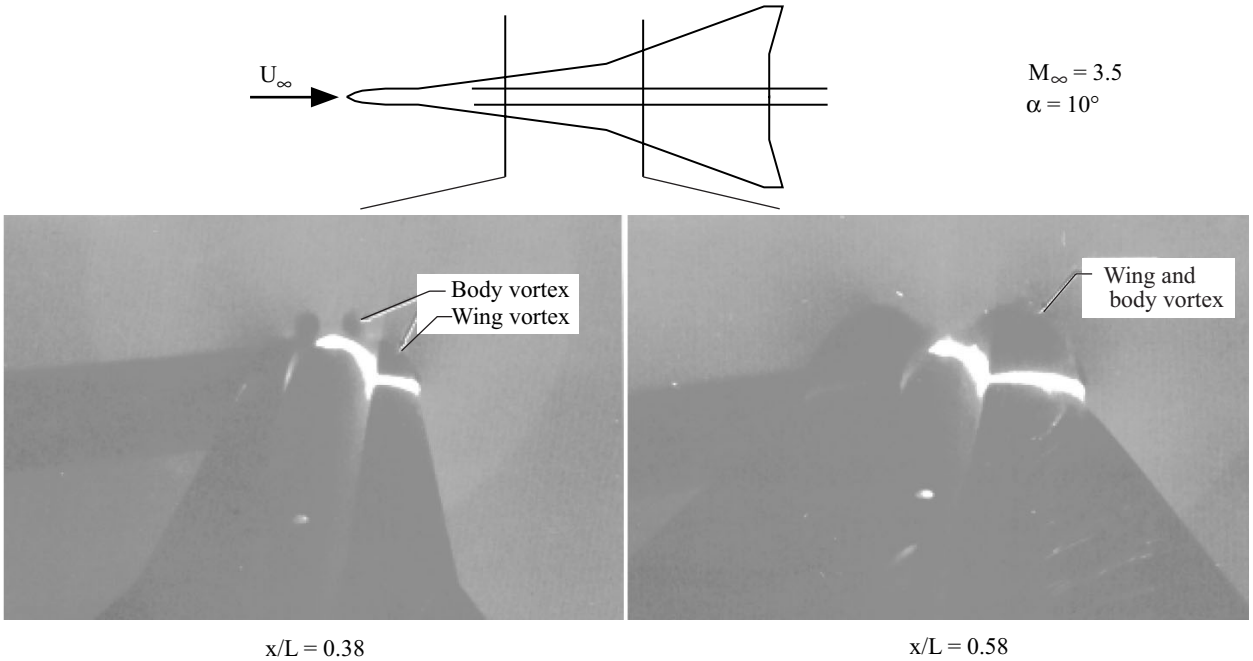

Figure 39. Lee-side flow characteristics for delta planform wing with strake and body at Mach 3.5 and angle of attack of 10° (ref. 160).

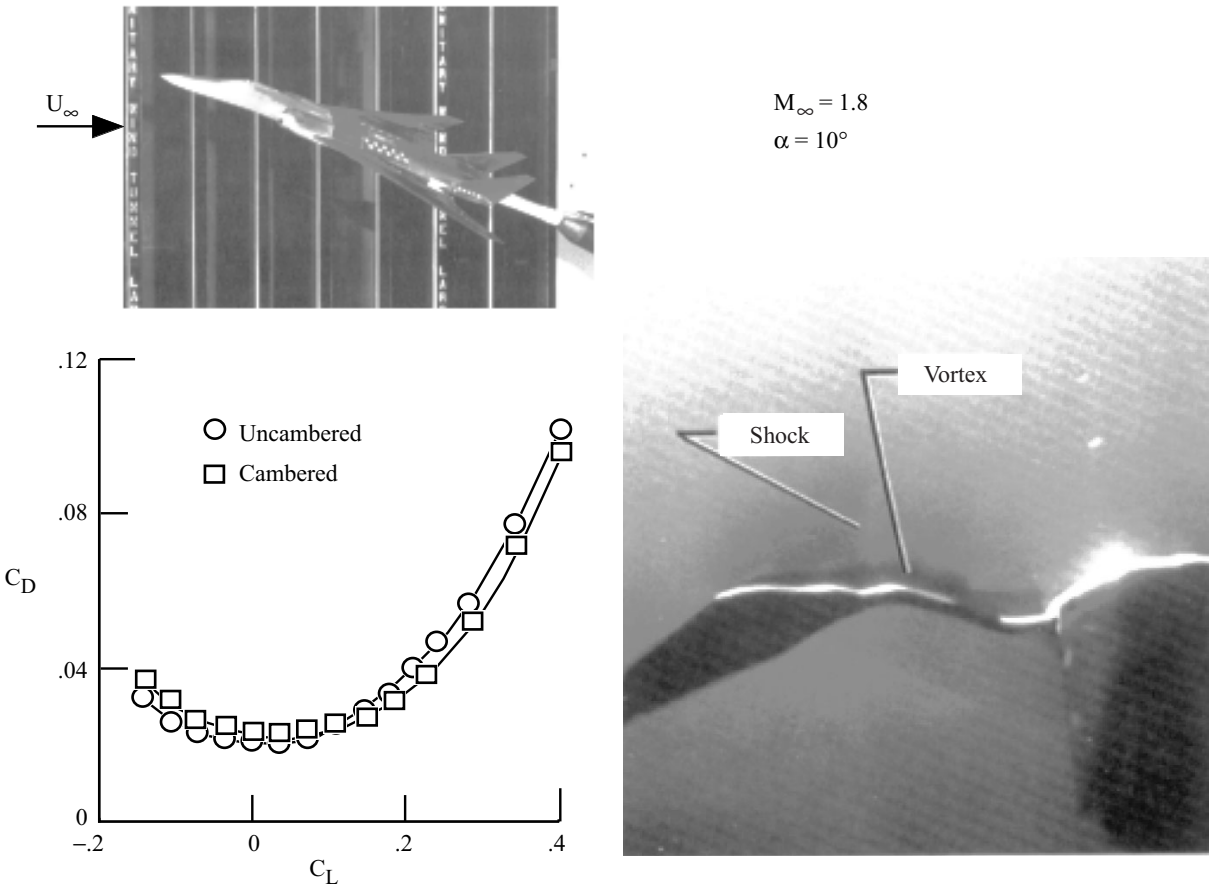

Figure 40. Lee-side flow characteristics for cranked arrow planform wing with body at Mach 1.8 and angle of attack of 10° (ref. 167).

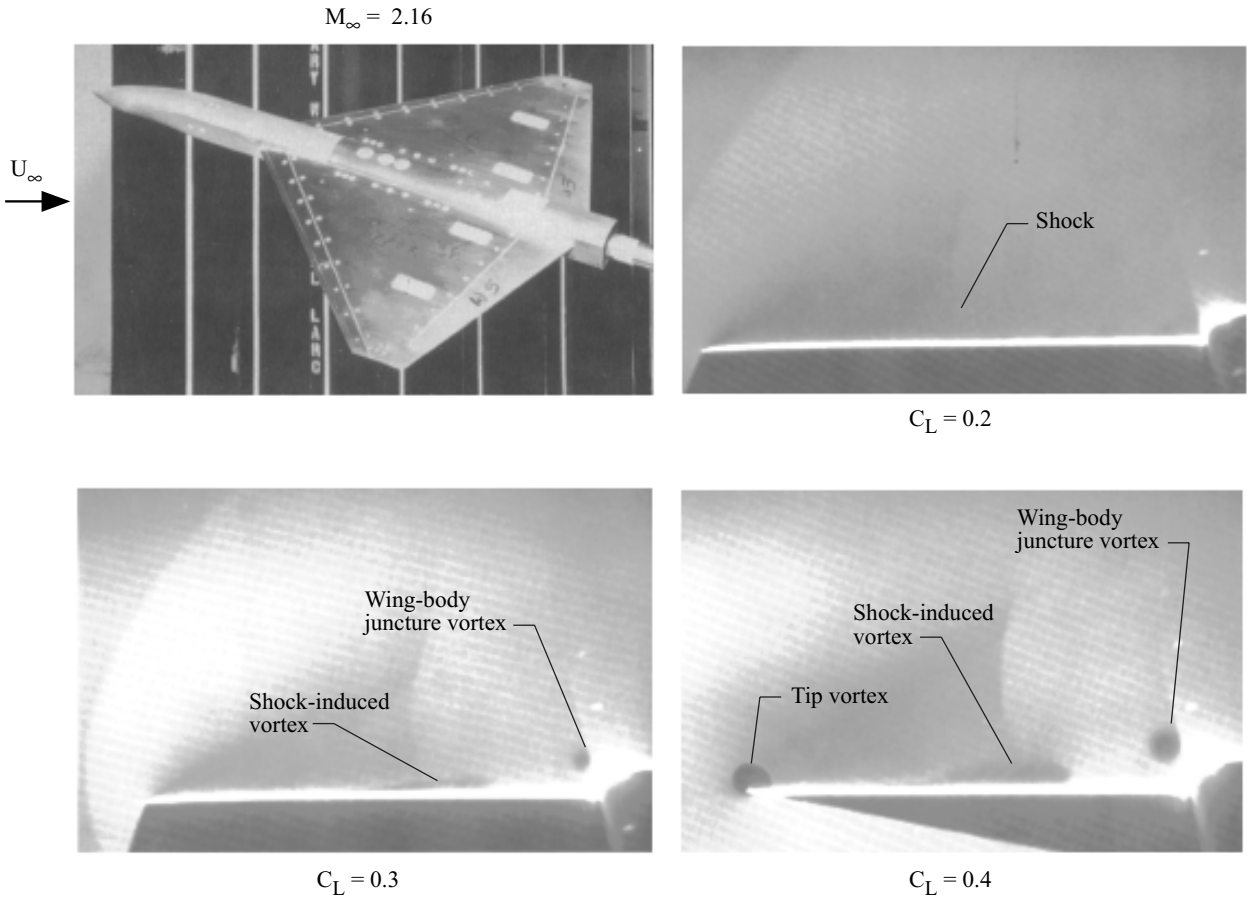

Figure 41. Lee-side characteristics for delta planform wing with body at Mach 2.16 (ref. 157).

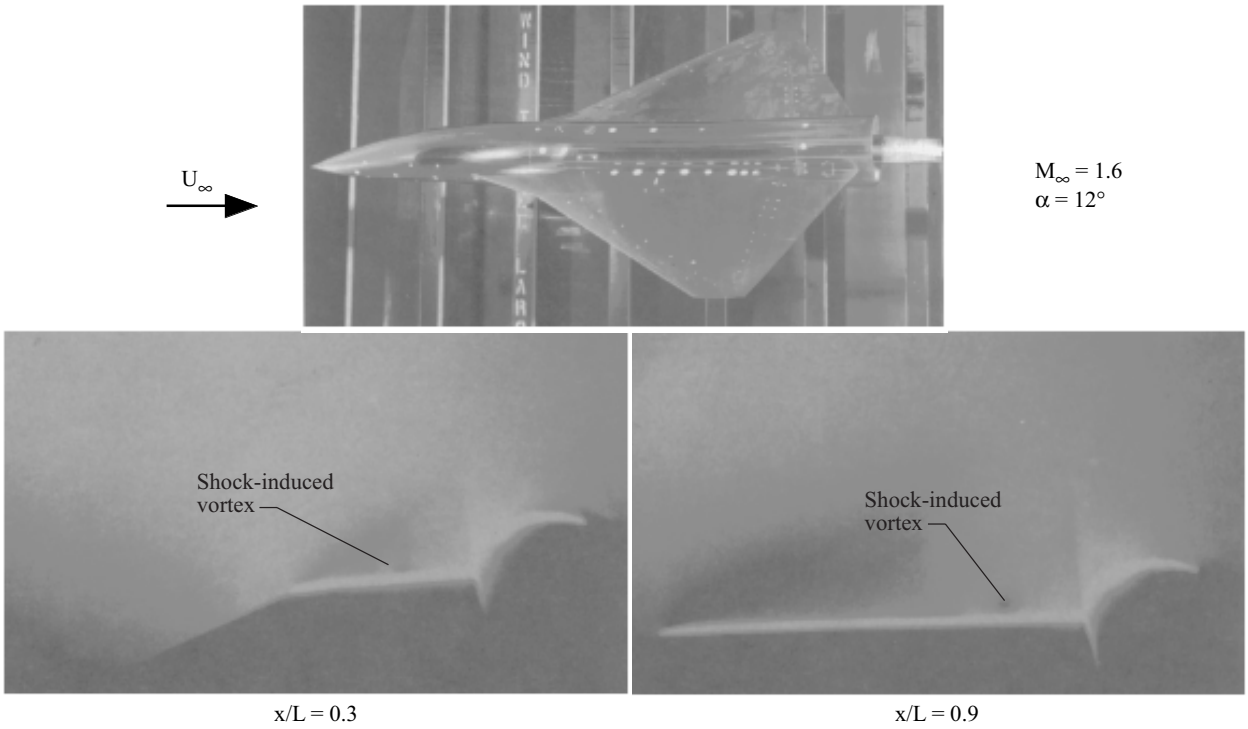

Figure 42. Lee-side flow characteristics for delta planform wing with body at Mach 1.6 and angle of attack of 12° (ref. 161).

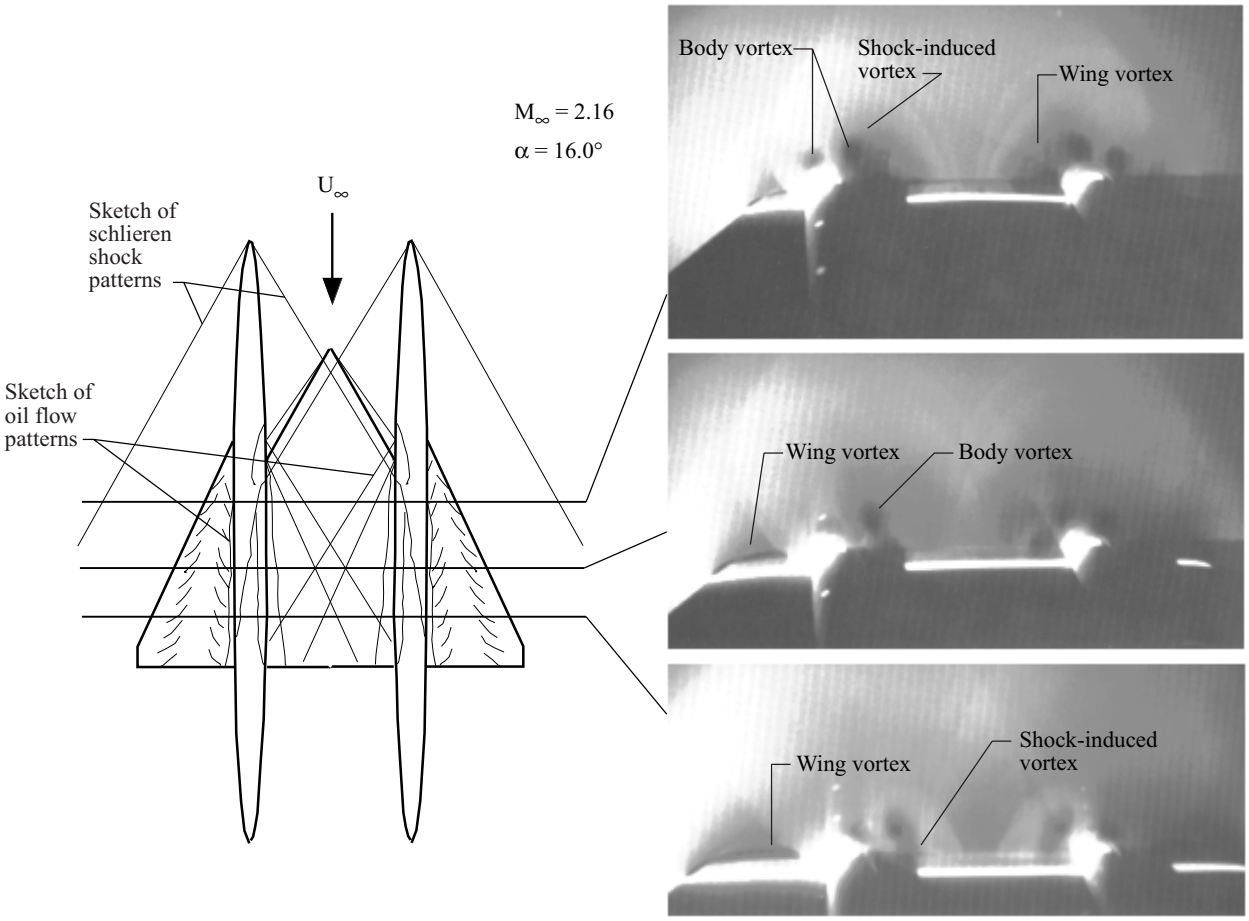

Figure 43. Lee-side flow characteristics for delta planform wing with multiple bodies at Mach 2.16 and angle of attack of 16° (ref. 163).

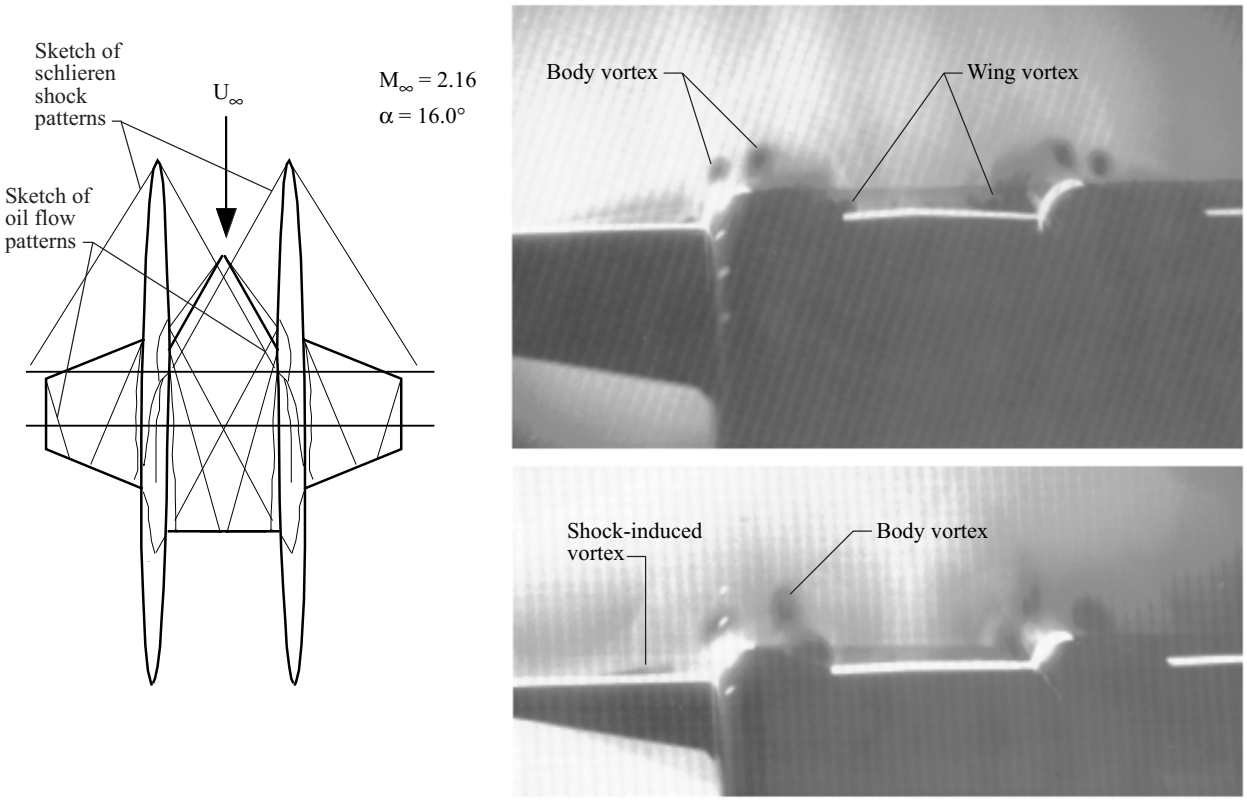

Figure 44. Lee-side flow characteristics for trapezoidal planform wing with multiple bodies at Mach 2.16 and angle of attack of 16° (ref. 163).

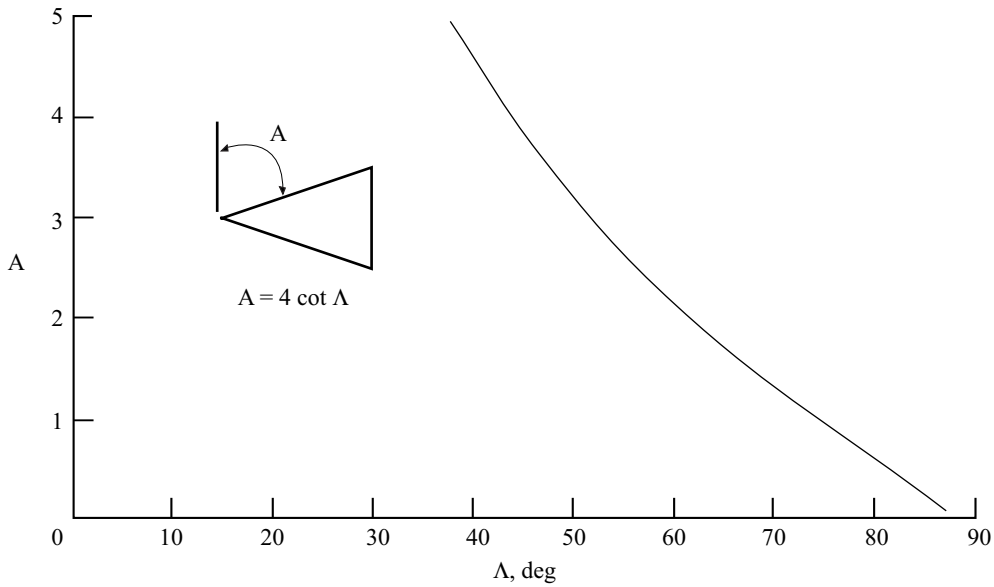

(a) Relationship between A and Λ for delta wings.

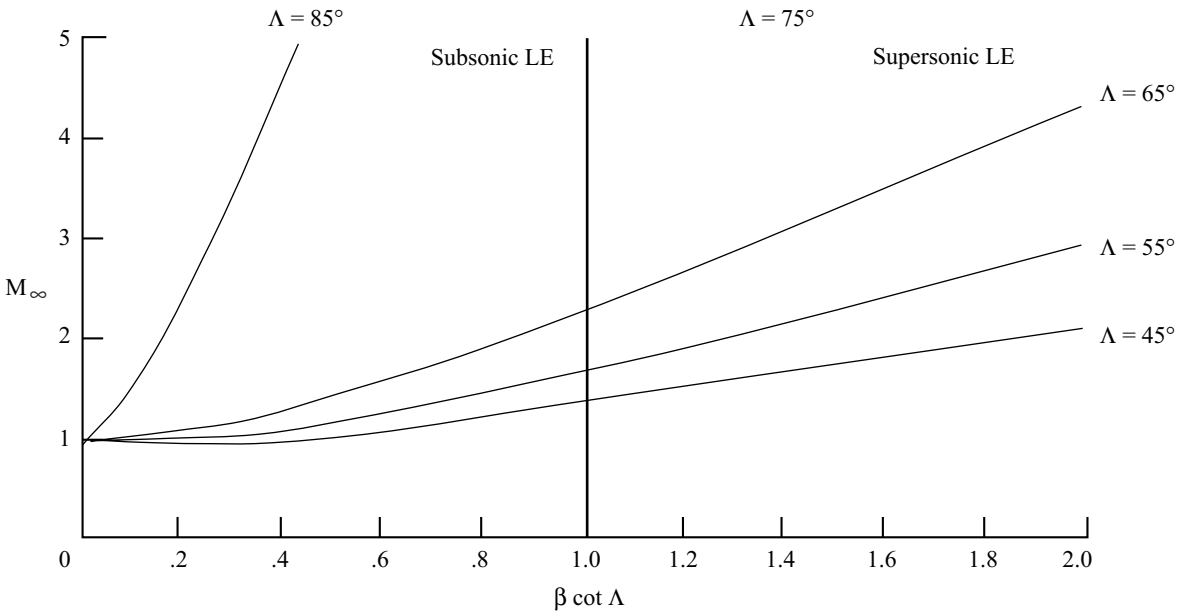

(b) Relationship between M_∞ and β cot Λ for delta wings.

Figure 45. Correlation parameters for delta wings (ref. 181).

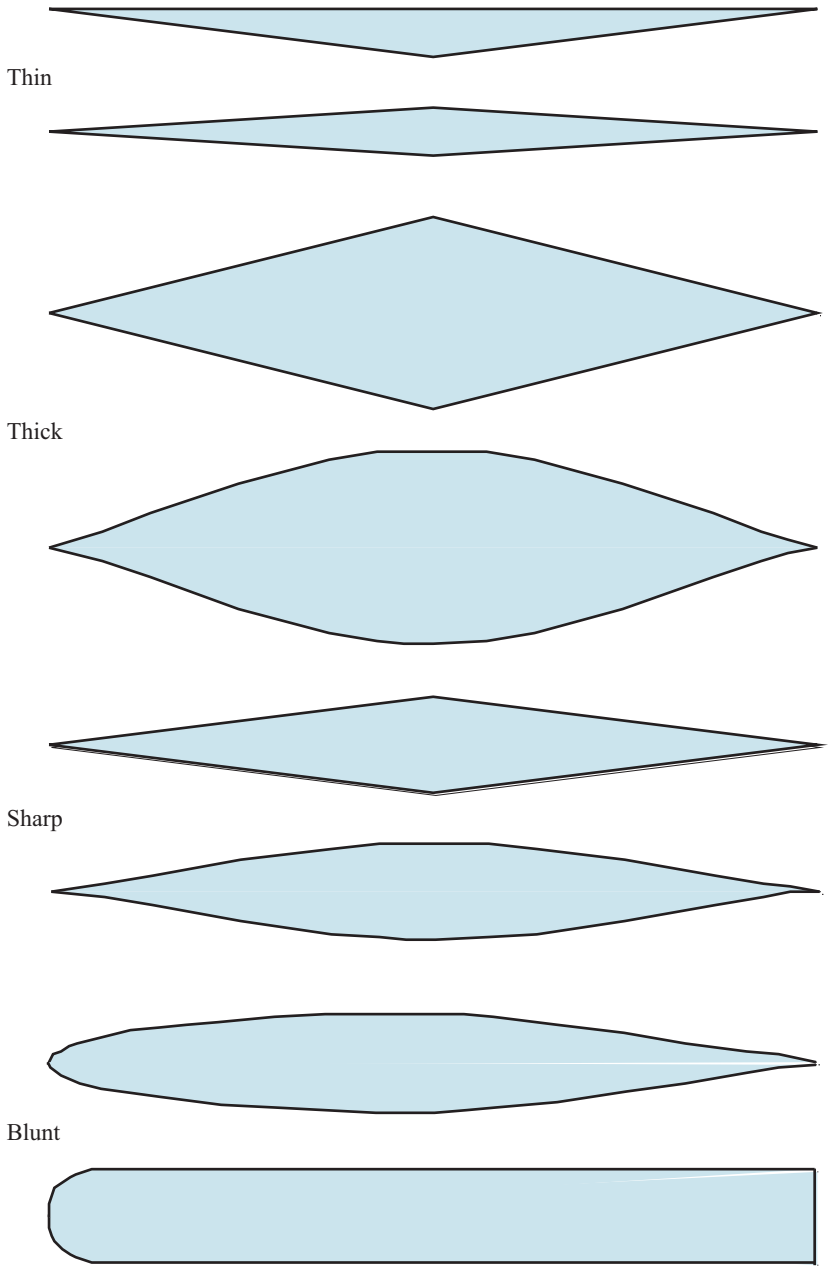

(a) Sketches of representative airfoils.

Figure 46. Lift characteristics of delta wings at supersonic speeds (ref. 181).

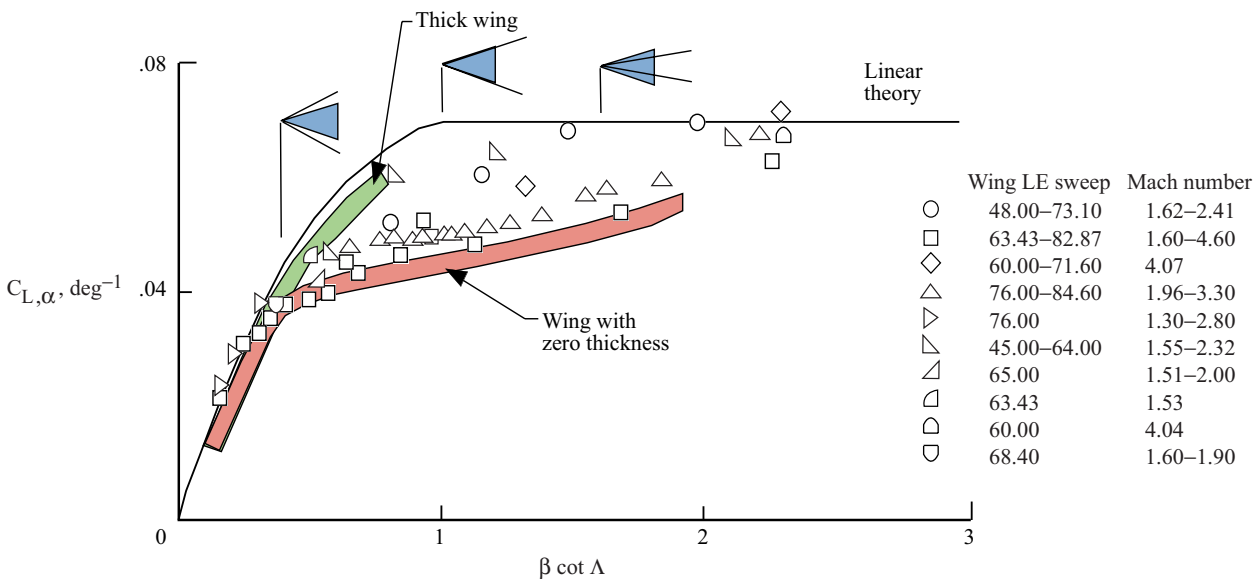

(b) Lift characteristics of sharp leading-edge delta wings with varying thicknesses.

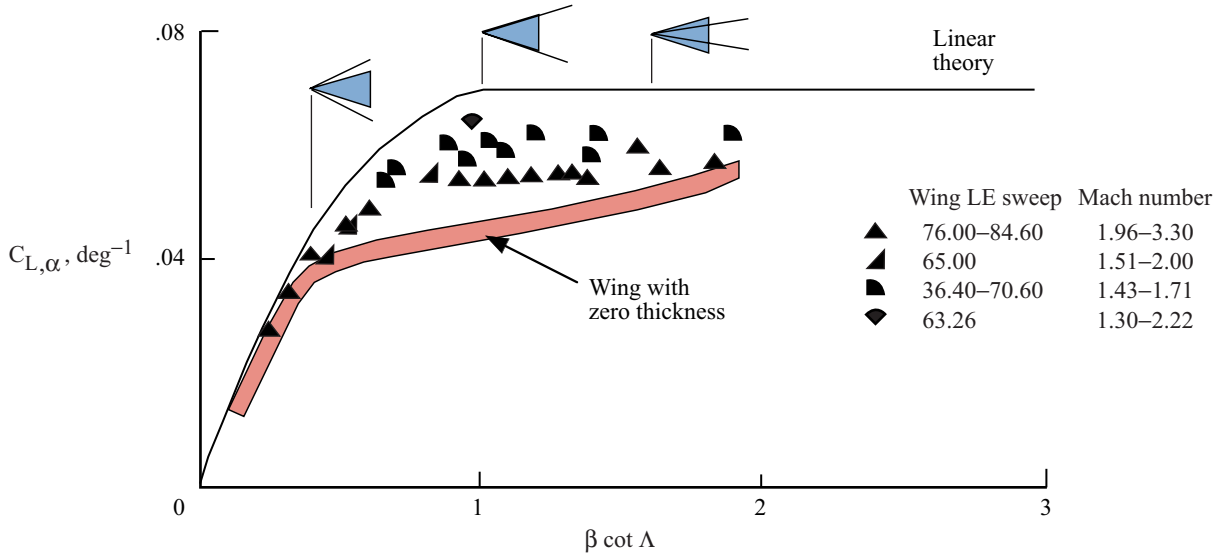

(c) Lift characteristics of thin delta wings with varying leading-edge bluntness.

Figure 46. Concluded.

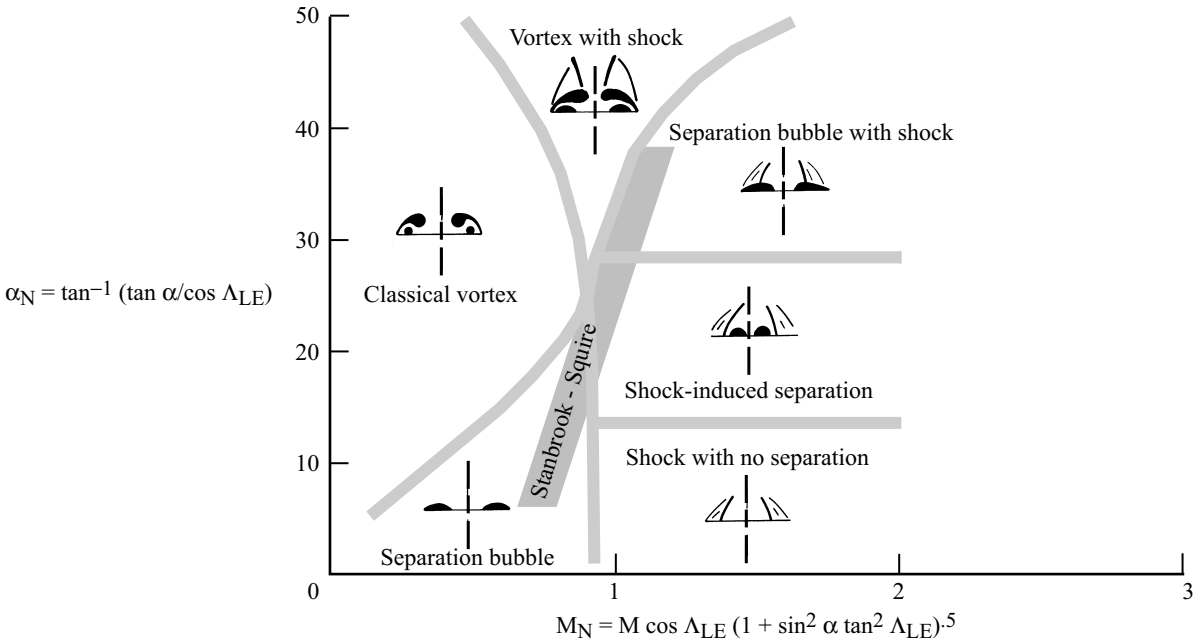

Figure 47. Sketch of Miller-Wood lee-side flow classification for delta wings at supersonic speeds (ref. 133).

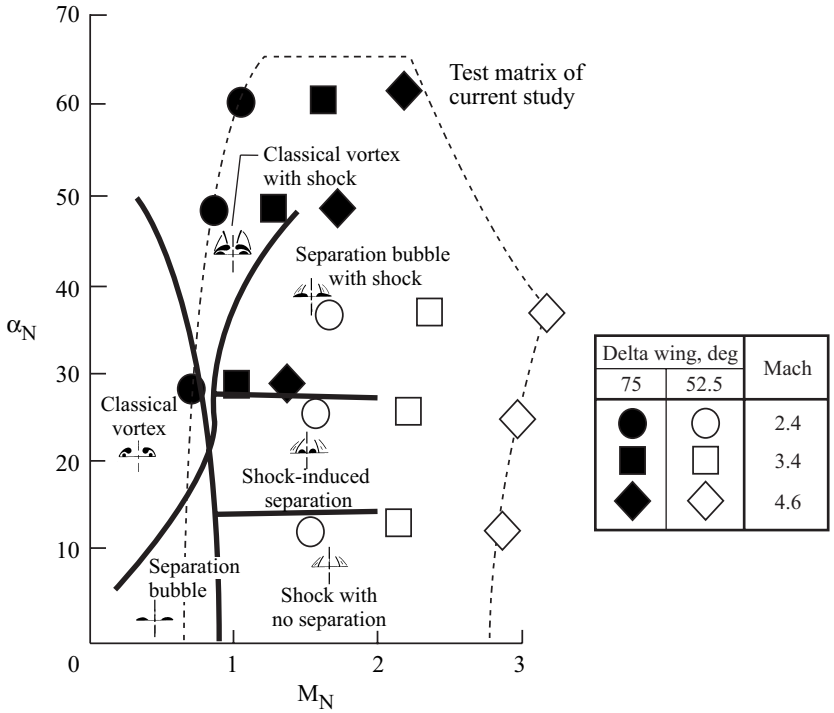

Figure 48. Sketch showing M_N and α_N conditions of test points.

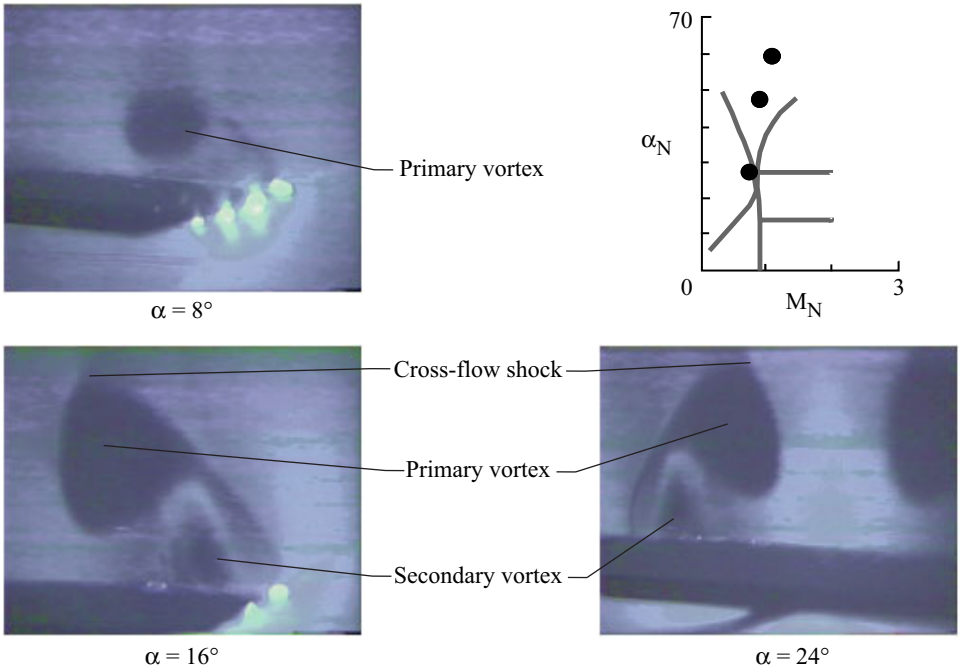

(a) $M_\infty = 2.4$.

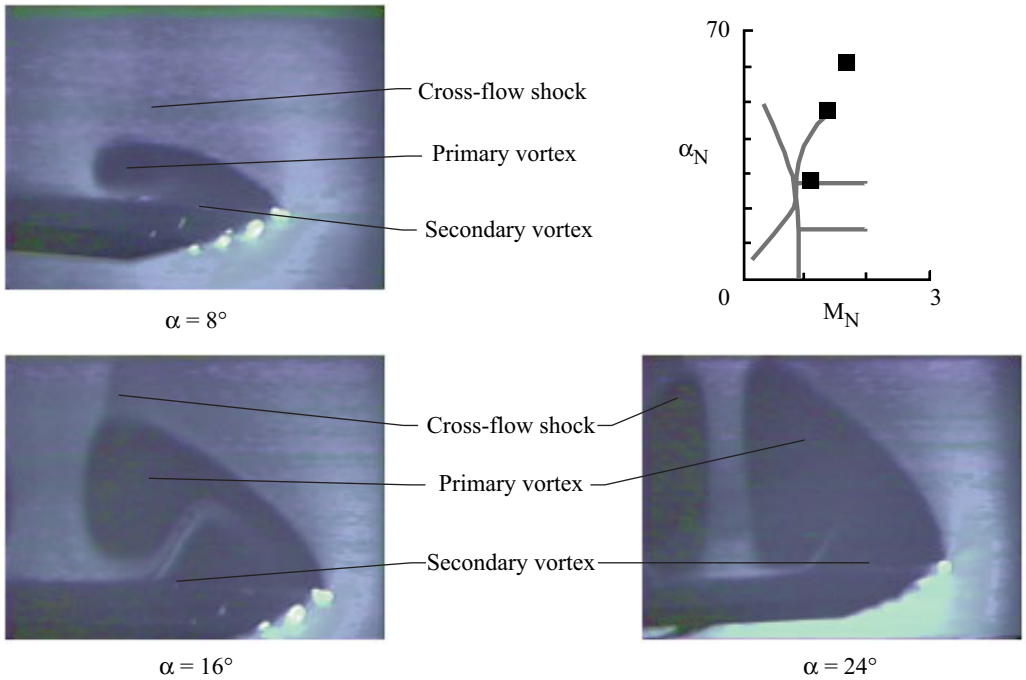

(b) $M_\infty = 3.4$.

Figure 49. Vapor-screen photographs of 75° delta wing model in Langley UPWT at α = 8°, 16°, and 24° (ref. 112).

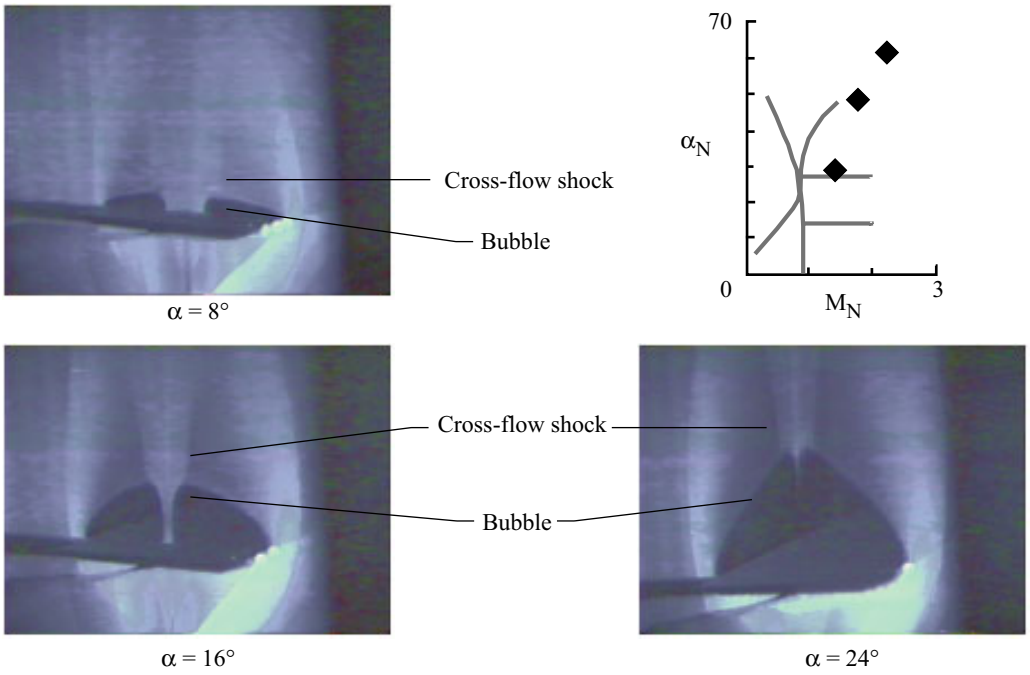

(c) $M_\infty = 4.6$.

Figure 49. Concluded.

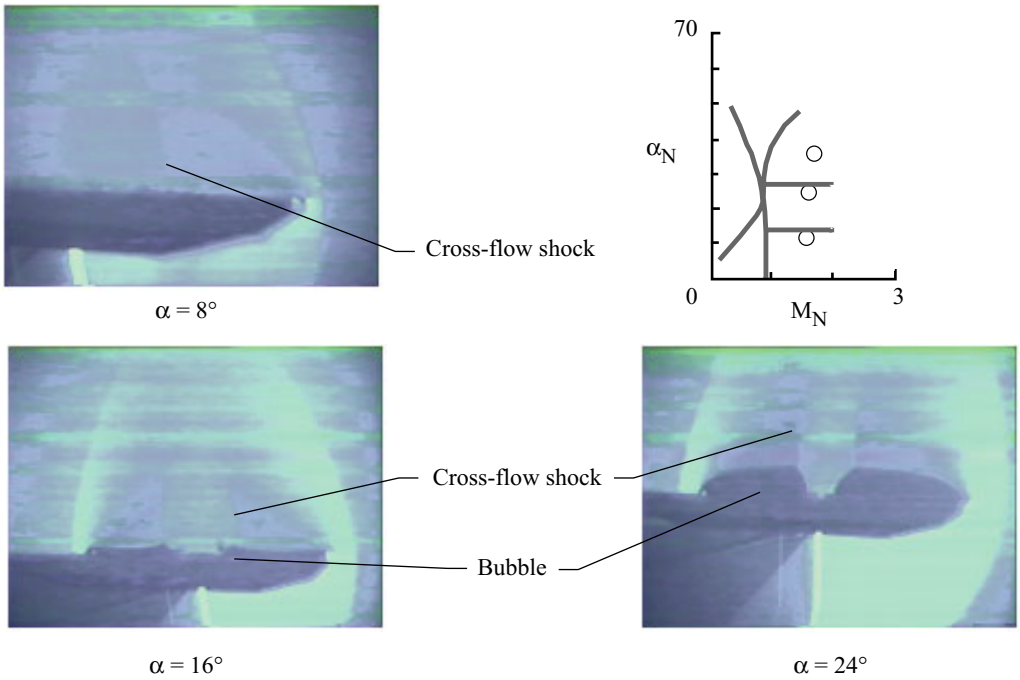

(a) $M_\infty = 2.4$.

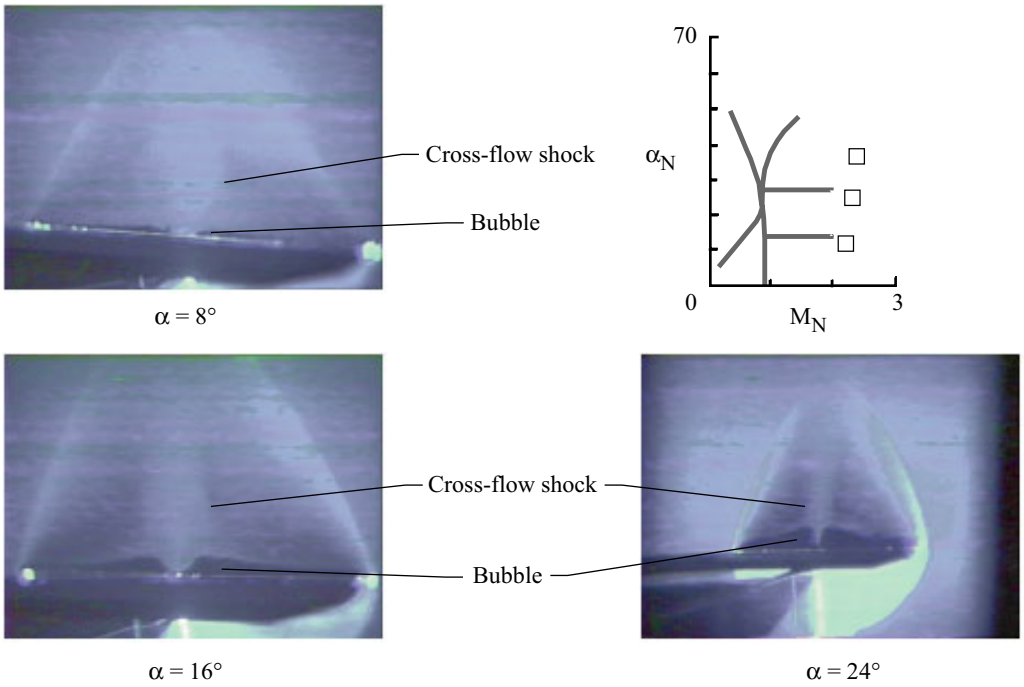

(b) $M_\infty = 3.4$.

Figure 50. Vapor-screen photographs of 52.5° delta wing model in Langley UPWT at α = 8°, 16°, and 24° (ref. 112).

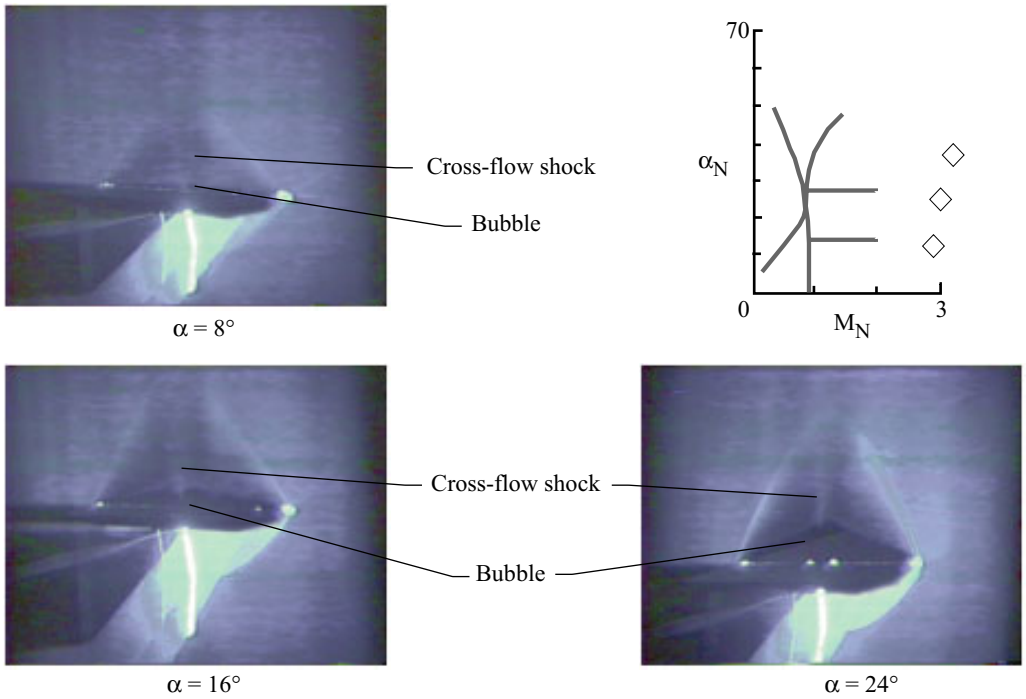

(c) $M_\infty = 4.6$.

Figure 50. Concluded.

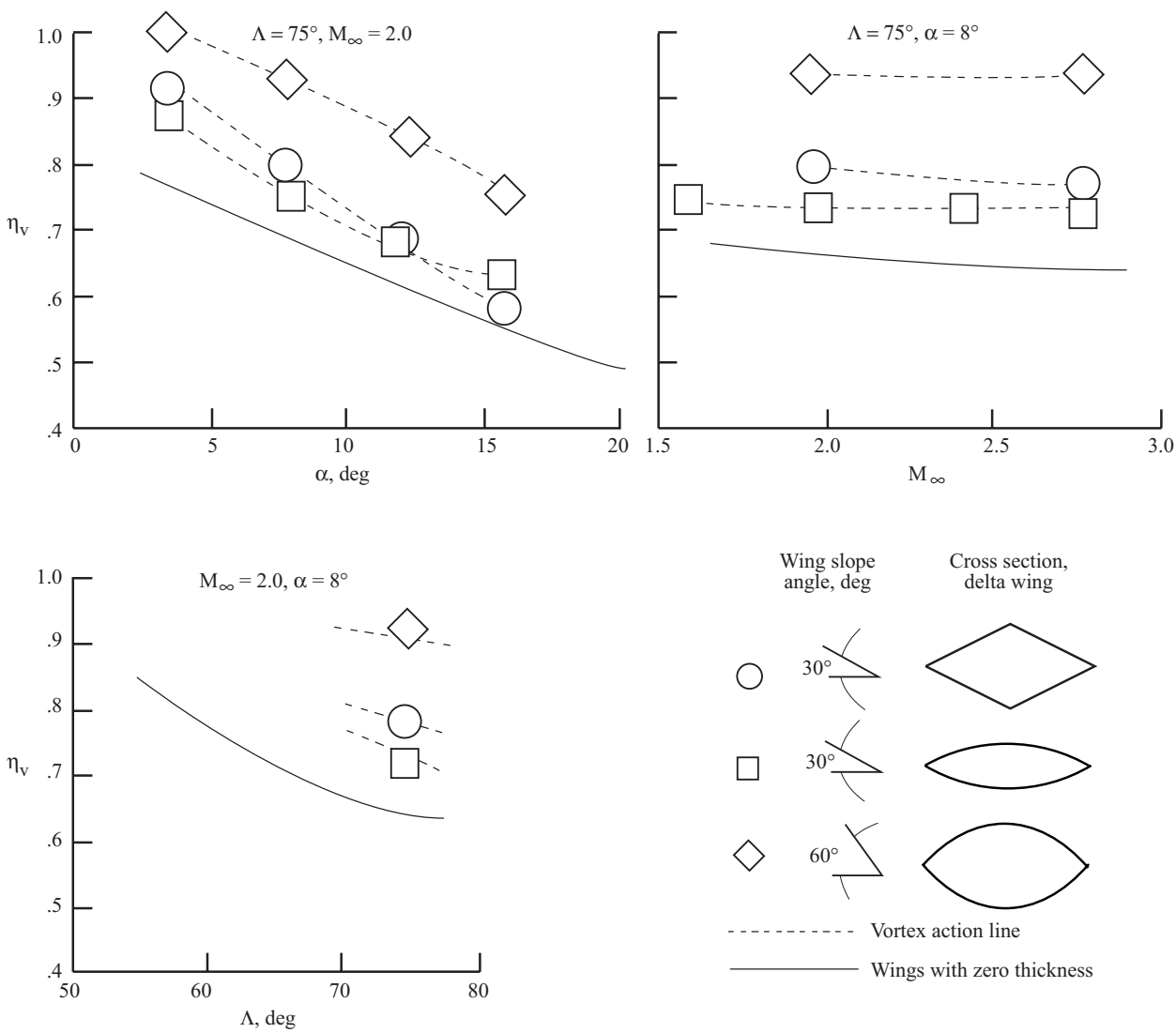

Figure 51. Location of vortex action line for thick delta wings at supersonic speeds (ref. 182).

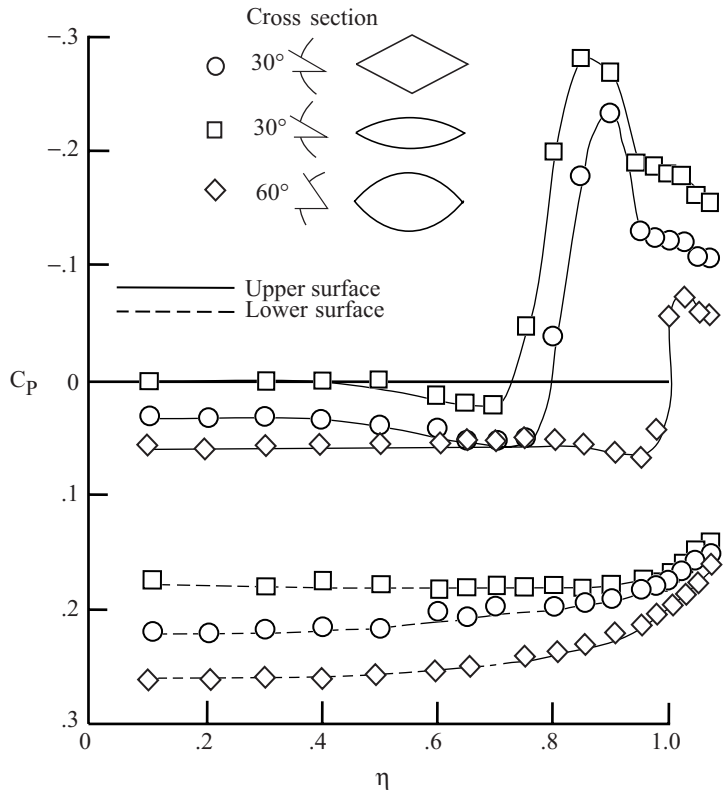

Figure 52. Effect of wing thickness on spanwise surface pressure distributions of thick delta wings at $M_\infty = 1.30$ and $\alpha = 8°$ (ref. 182).

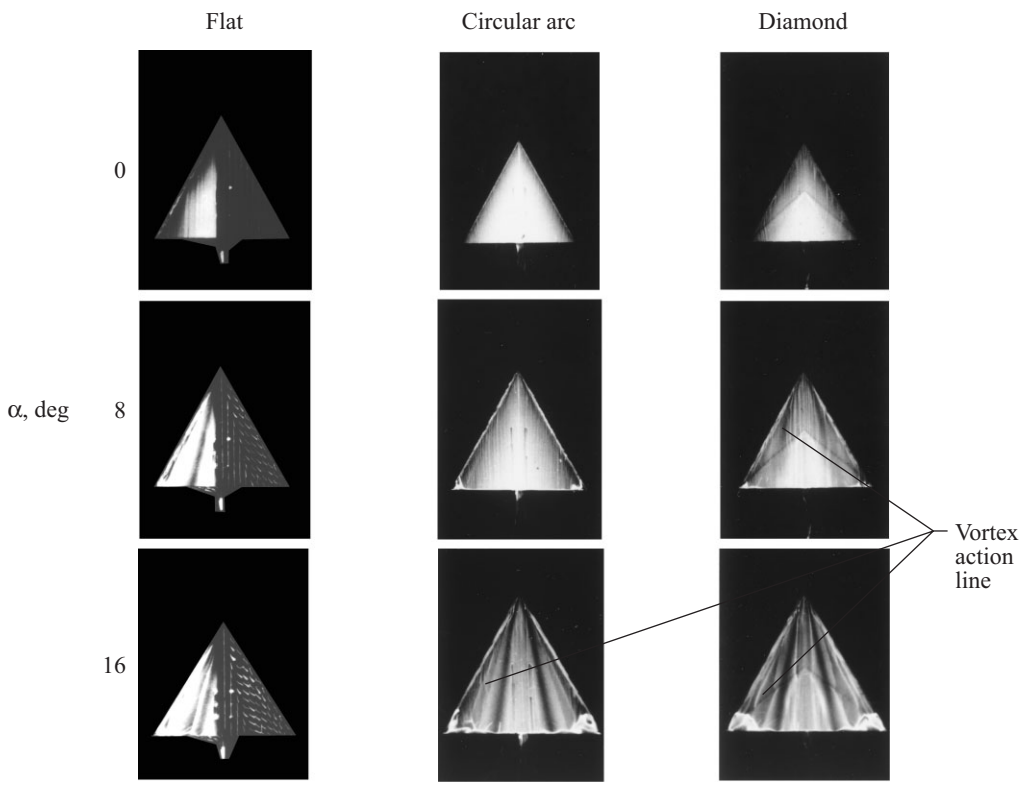

Figure 53. Effect of airfoil shape and angle of attack on upper surface flow characteristics of thick delta wings at $M_\infty = 1.70$ and $\Lambda = 60°$ (ref. 138).

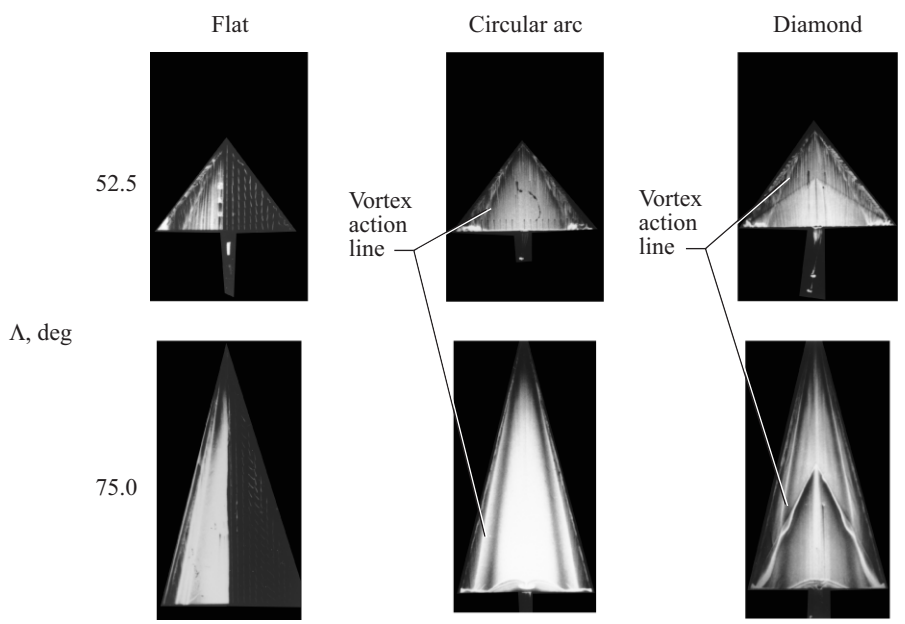

Figure 54. Effect of airfoil shape and leading edge on upper surface flow characteristics of thick delta wings at $M_\infty = 1.70$ and $\alpha = 8°$ (ref. 138).

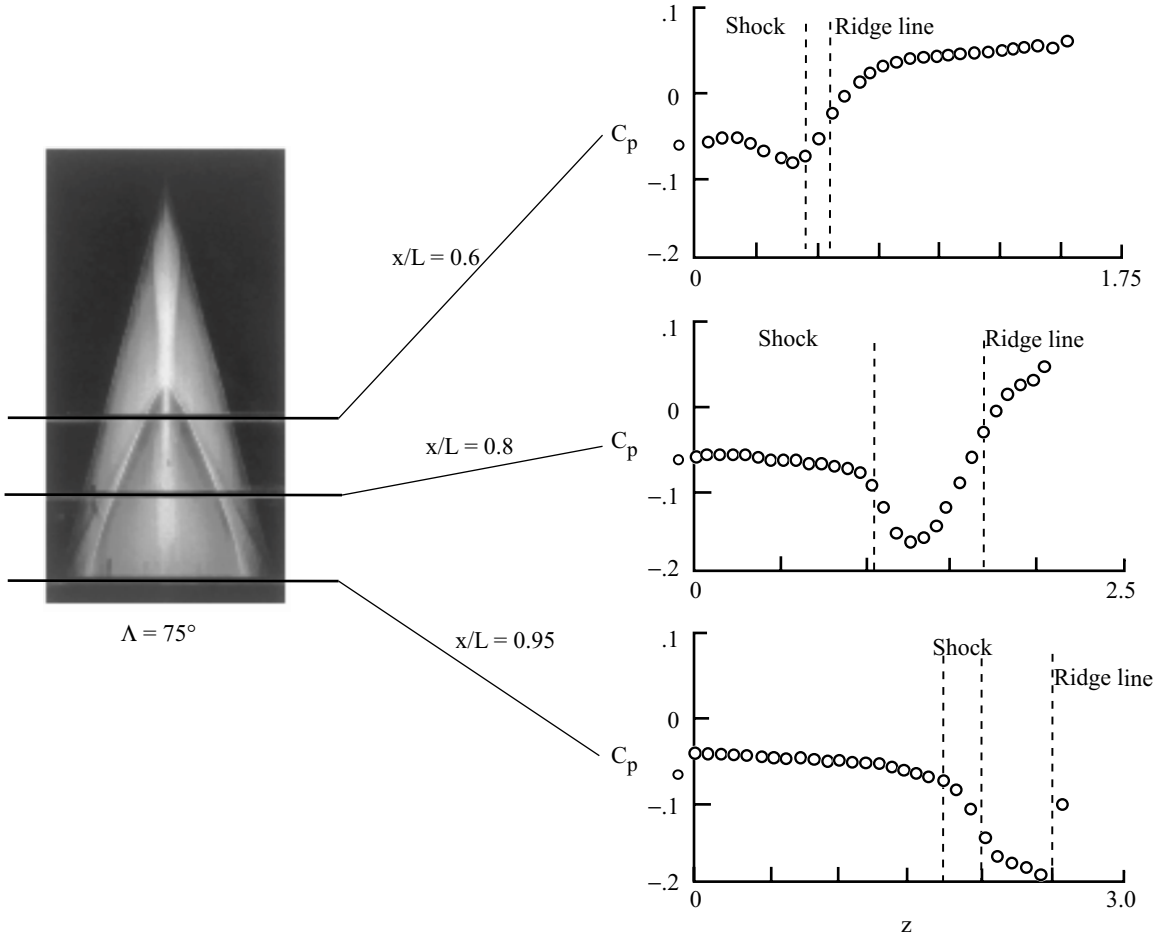

Figure 55. Effect of airfoil shape on upper surface flow characteristics of a 75° swept delta wing with diamond airfoil at $M_\infty = 2.00$ and $\alpha = 0°$ (ref. 138).

$S = 302.29\ in^2$

$b = 18.00$ in.

$c = 22.39$ in.

$\delta_F = 0°$, 5°, and 15°

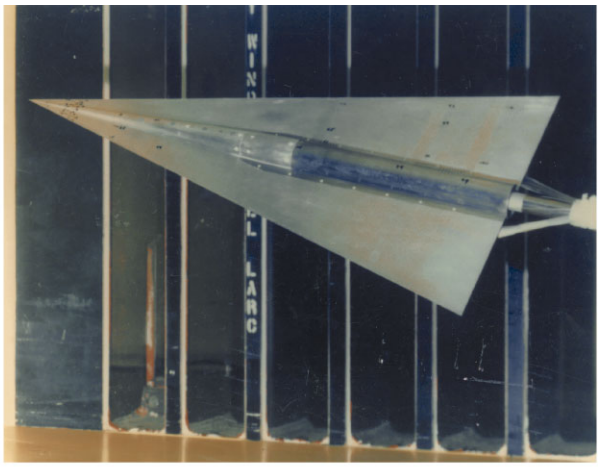

75° delta
$\delta_F = 0°$

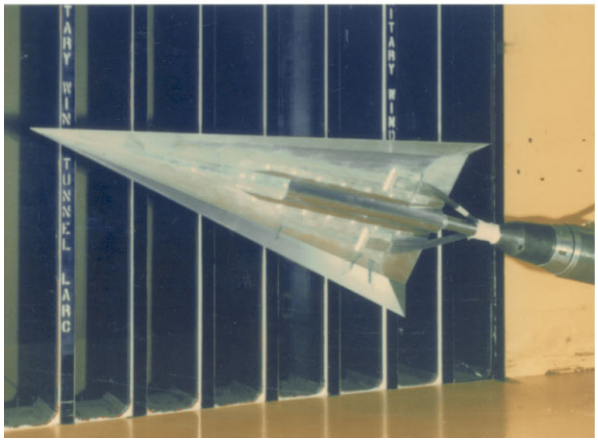

75° delta (lower surface)
$\delta_F = 10°$

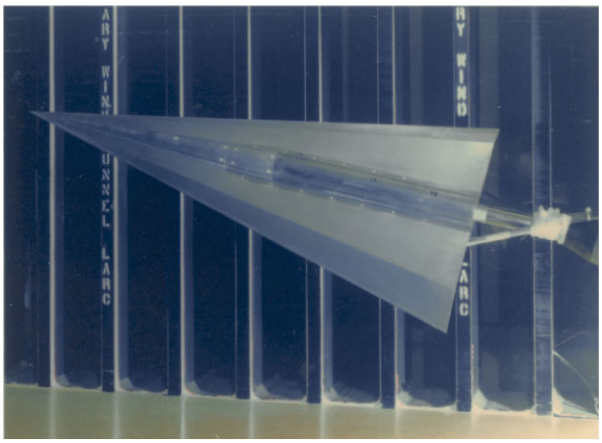

75° delta (upper surface)
$\delta_F = 10°$

Figure 56. Photograph of 75° swept delta wing model with leading-edge flaps installed in Langley UPWT (ref. 110).

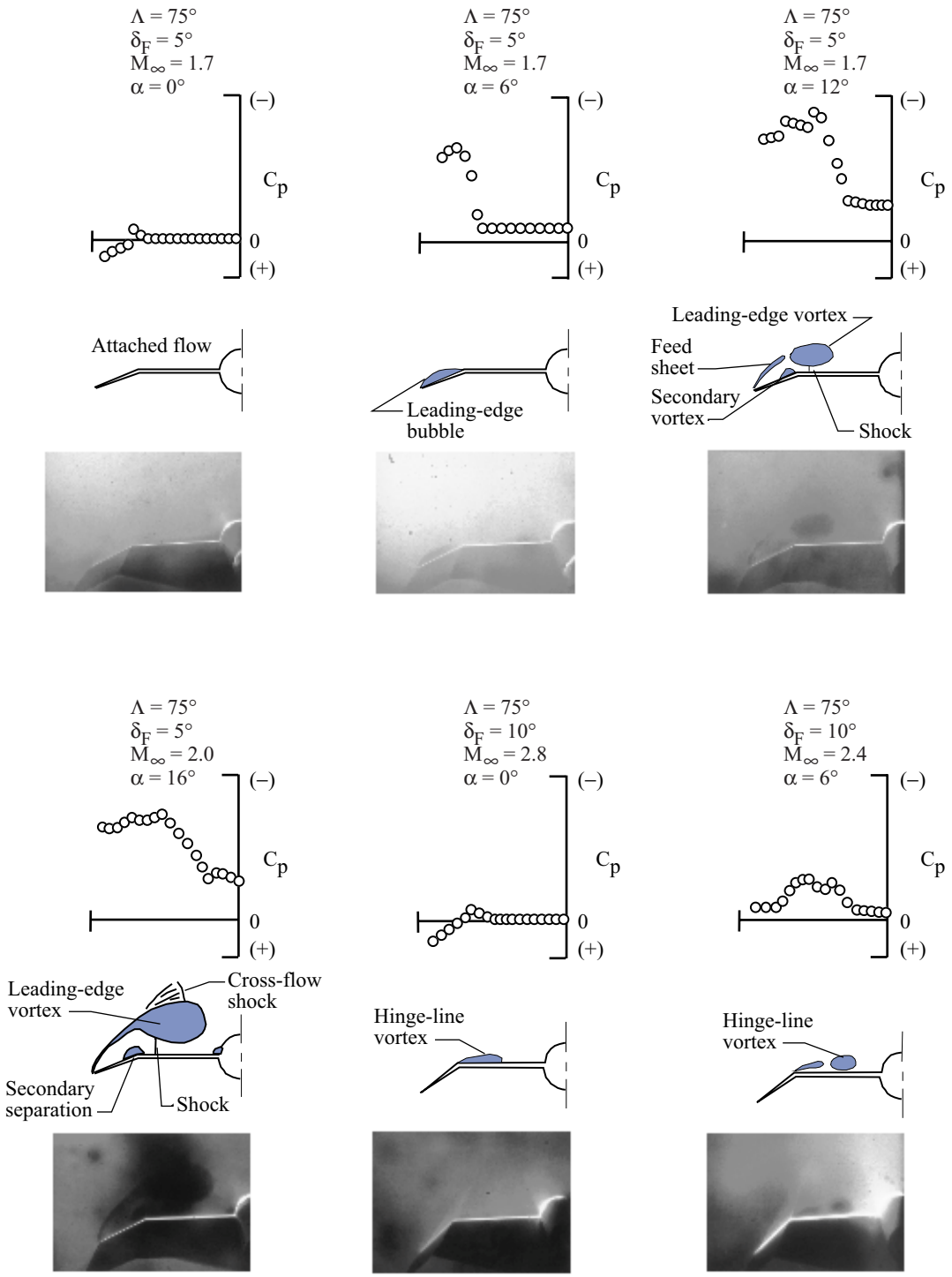

Figure 57. Wing upper surface pressure distributions and vapor-screen photographs of lee-side flow characteristics for single-feature flow types observed on 75° swept delta wing with leading-edge flaps (ref. 110).

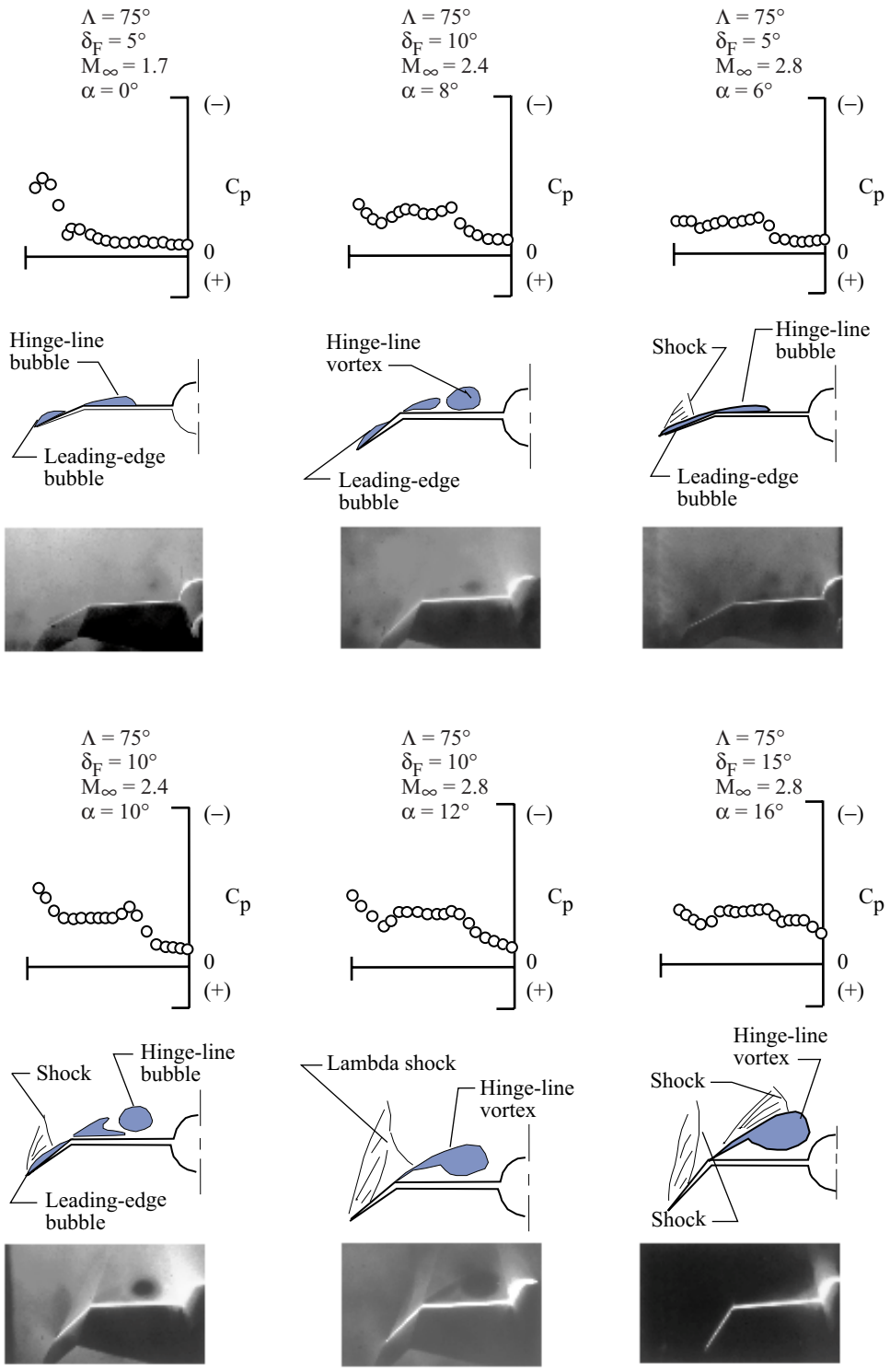

Figure 58. Wing upper surface pressure distributions and vapor-screen photographs of lee-side flow characteristics for double-feature flow types observed on 75° delta wing with leading-edge flaps (ref. 110).

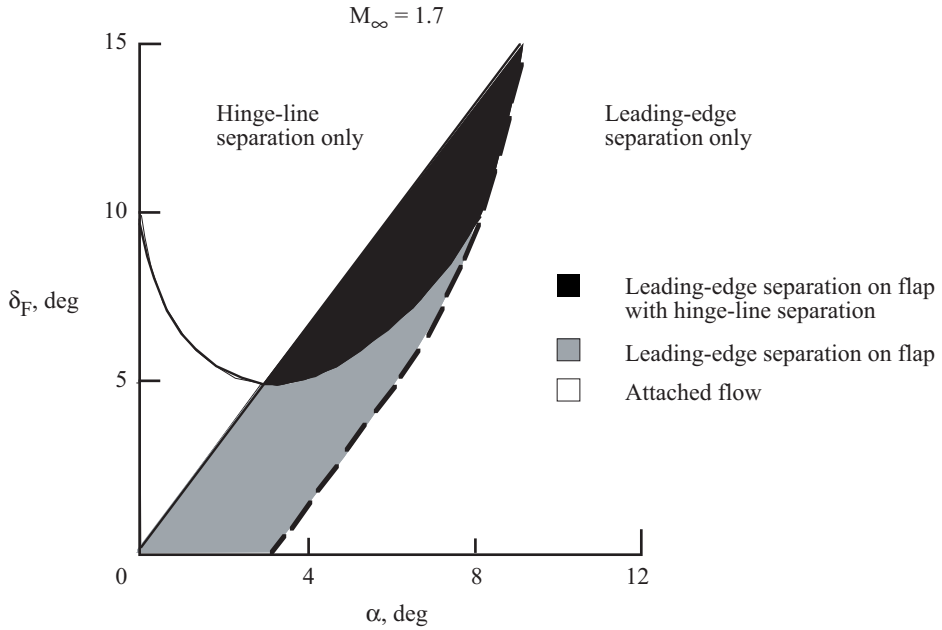

Figure 59. Assessment of vortex flap effectiveness at supersonic speeds (ref. 110).

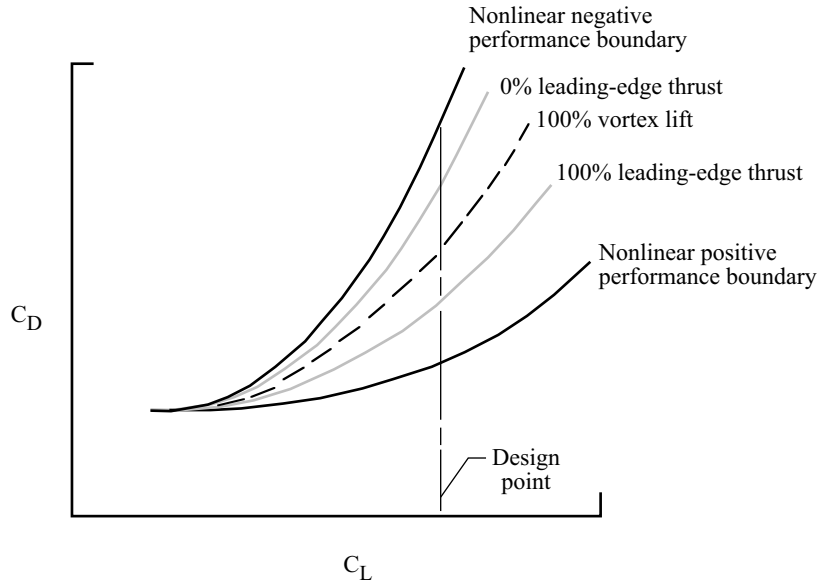

Figure 60. Notational sketch of linear-theory and nonlinear aerodynamic performance boundary (ref. 182).

Region	Geometry	Pressure	Drag
A	Positive slope	High	High
B	Positive slope	Low	Low
C	Negative slope	Low	High
D	Negative slope	High	Low

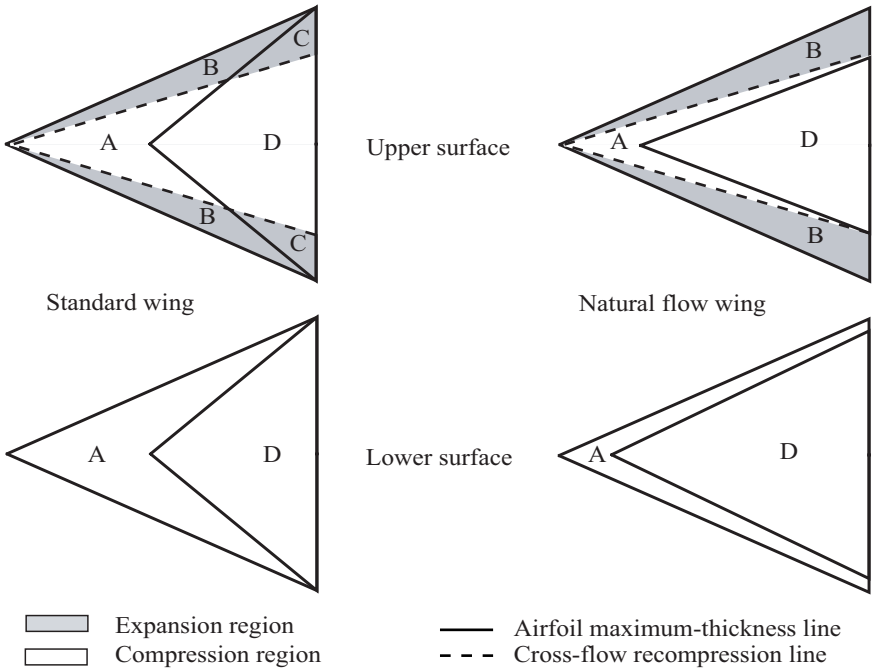

Figure 61. Schematic of natural flow wing design approach (ref. 182).

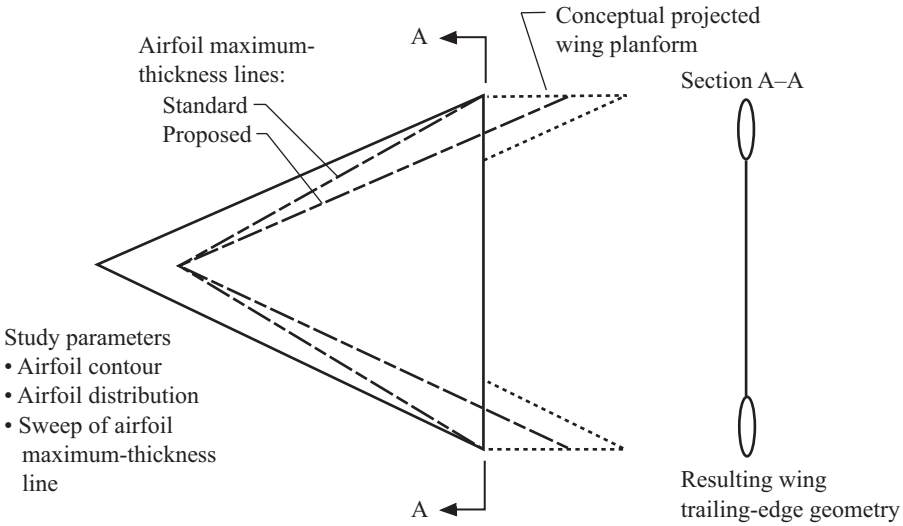

Figure 62. Near-conical maximum-thickness location and resulting geometry for natural flow design approach (ref. 182).

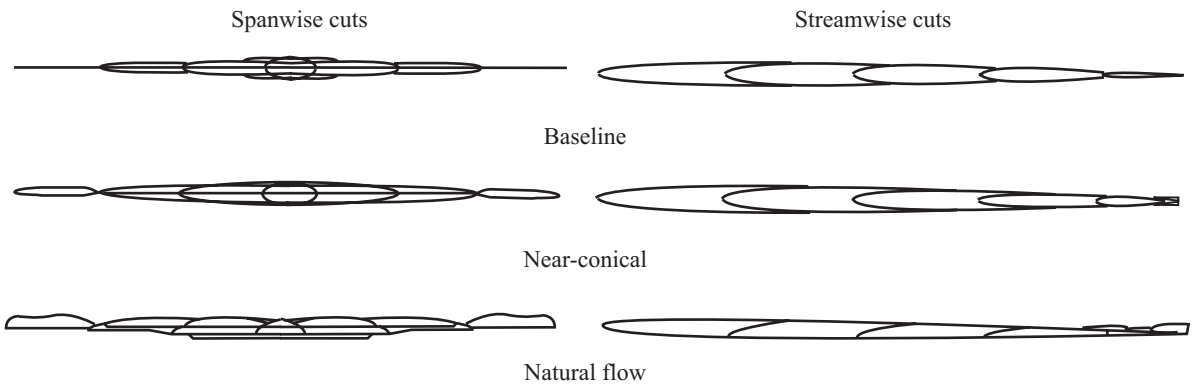

(a) Spanwise and streamwise cuts.

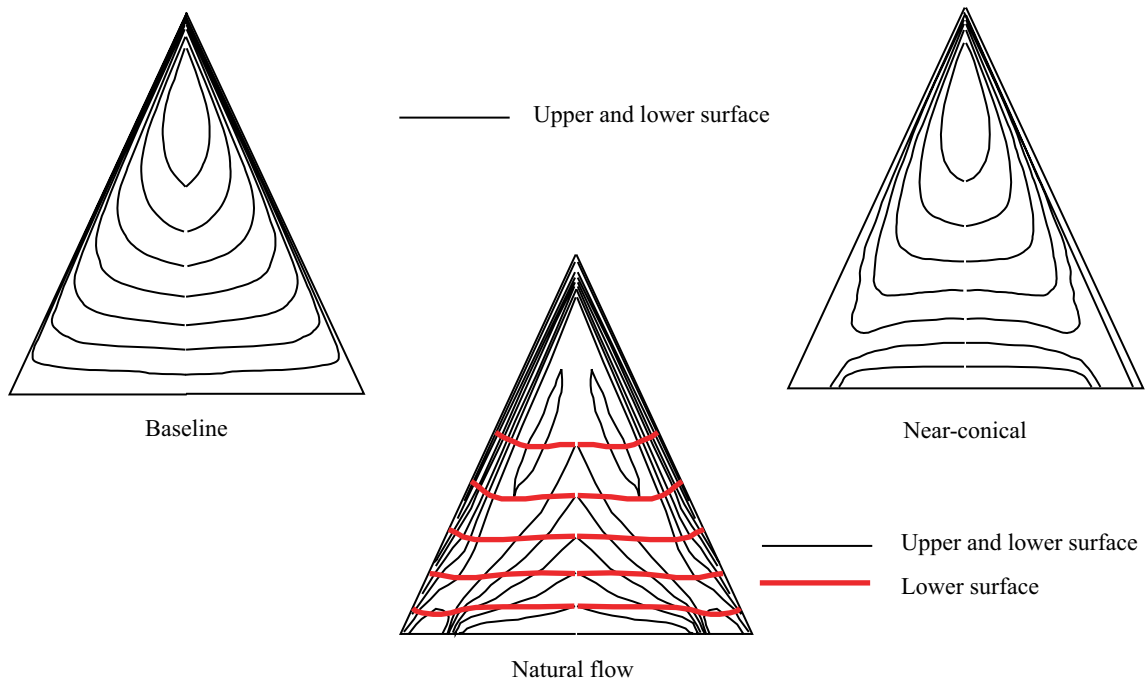

(b) Elevation cuts.

Figure 63. Geometric details of baseline, near-conical, and natural flow 65° delta wing models (ref. 182).

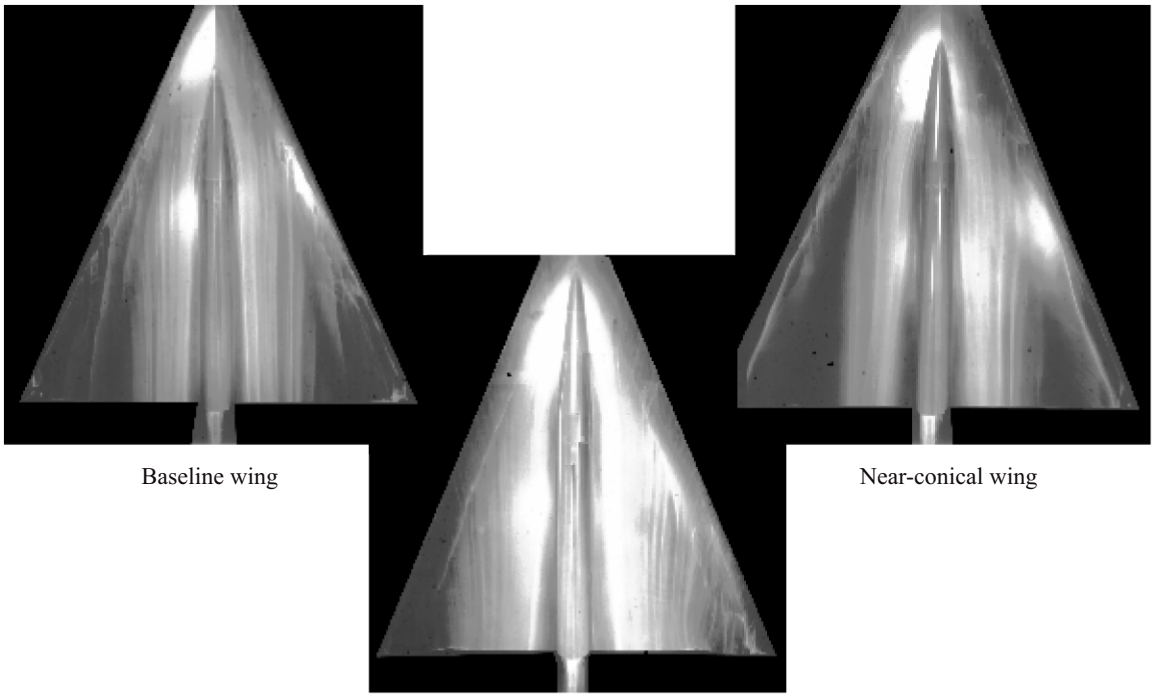

Figure 64. Oil-flow photographs of lee-side flow characteristics for the baseline, near-conical, and natural flow 65° delta wing models at $M_\infty = 1.62$ and $\alpha = 8°$ (ref. 182).

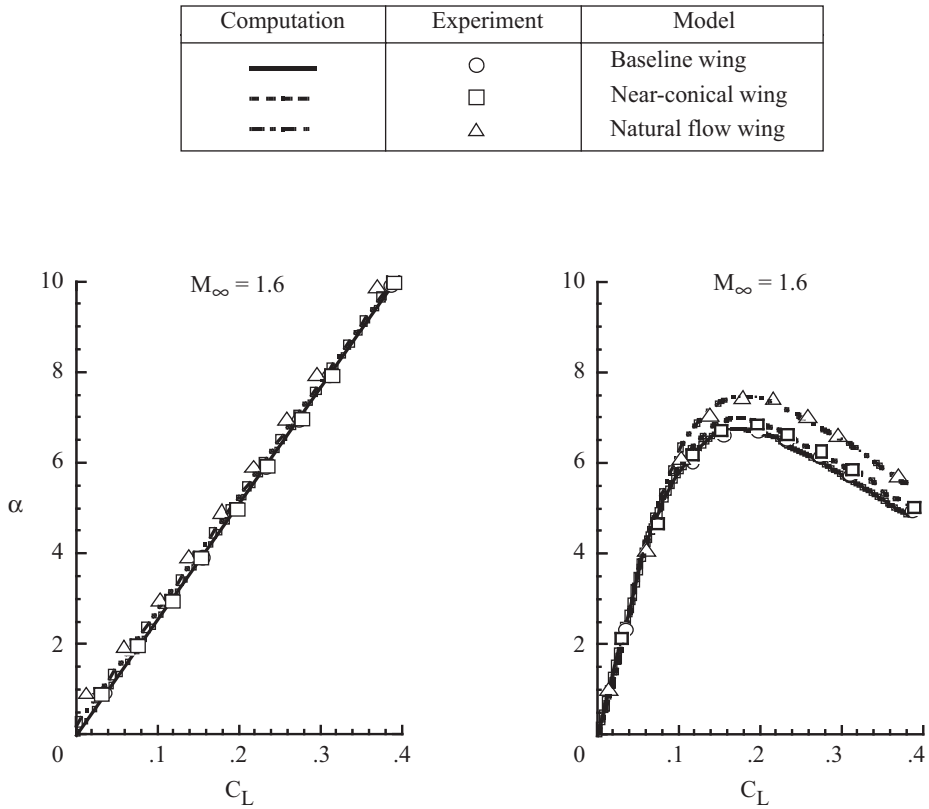

Figure 65. Plot of lift and lift-to-drag ratio characteristics for baseline, near-conical, and natural flow 65° delta wing models (ref. 182).

REPORT DOCUMENTATION PAGE

Form Approved
OMB No. 0704-0188

The public reporting burden for this collection of information is estimated to average 1 hour per response, including the time for reviewing instructions, searching existing data sources, gathering and maintaining the data needed, and completing and reviewing the collection of information. Send comments regarding this burden estimate or any other aspect of this collection of information, including suggestions for reducing this burden, to Department of Defense, Washington Headquarters Services, Directorate for Information Operations and Reports (0704-0188), 1215 Jefferson Davis Highway, Suite 1204, Arlington, VA 22202-4302. Respondents should be aware that notwithstanding any other provision of law, no person shall be subject to any penalty for failing to comply with a collection of information if it does not display a currently valid OMB control number.
PLEASE DO NOT RETURN YOUR FORM TO THE ABOVE ADDRESS.

1. REPORT DATE *(DD-MM-YYYY)*
01- 03 - 2003

2. REPORT TYPE
Technical Publication

3. DATES COVERED *(From - To)*

4. TITLE AND SUBTITLE
Vortex Flows at Supersonic Speeds

5a. CONTRACT NUMBER

5b. GRANT NUMBER

5c. PROGRAM ELEMENT NUMBER

6. AUTHOR(S)
Wood, Richard M.; Wilcox, Floyd J., Jr.; Bauer, Steven X. S.; and Allen, Jerry M.

5d. PROJECT NUMBER

5e. TASK NUMBER

5f. WORK UNIT NUMBER
706-51-21-10

7. PERFORMING ORGANIZATION NAME(S) AND ADDRESS(ES)
NASA Langley Research Center
Hampton, VA 23681-2199

8. PERFORMING ORGANIZATION REPORT NUMBER
L-18008

9. SPONSORING/MONITORING AGENCY NAME(S) AND ADDRESS(ES)
National Aeronautics and Space Administration
Washington, DC 20546-0001

10. SPONSOR/MONITOR'S ACRONYM(S)
NASA

11. SPONSOR/MONITOR'S REPORT NUMBER(S)
NASA/TP-2003-211950

12. DISTRIBUTION/AVAILABILITY STATEMENT
Unclassified - Unlimited
Subject Category 02
Availability: NASA CASI (301) 621-0390 Distribution: Standard

13. SUPPLEMENTARY NOTES
Wood, Wilcox, Bauer, and Allen, Langley Research Center
An electronic version can be found at http://techreports.larc.nasa.gov/ltrs/ or http://techreports.larc.nasa.gov/cgi-bin/NTRS

14. ABSTRACT

A review of research conducted at the National Aeronautics and Space Administration (NASA) Langley Research Center (LaRC) into high-speed vortex flows during the 1970s, 1980s, and 1990s is presented. The data are for flat plates, cavities, bodies, missiles, wings, and aircraft with Mach numbers of 1.5 to 4.6. Data are presented to show the types of vortex structures that occur at supersonic speeds and the impact of these flow structures on vehicle performance and control. The data show the presence of both small- and large-scale vortex structures for a variety of vehicles, from missiles to transports. For cavities, the data show very complex multiple vortex structures exist at all combinations of cavity depth to length ratios and Mach number. The data for missiles show the existence of very strong interference effects between body and/or fin vortices. Data are shown that highlight the effect of leading-edge sweep, leading-edge bluntness, wing thickness, location of maximum thickness, and camber on the aerodynamics of and flow over delta wings. Finally, a discussion of a design approach for wings that use vortex flows for improved aerodynamic performance at supersonic speeds is presented.

15. SUBJECT TERMS
Vortex flows; Supersonic aerodynamics; Wings; Missiles; Cavities; Flow visualization; Aerodynamic design; NASA Langley; Unitary Plan Wind Tunnel

16. SECURITY CLASSIFICATION OF:			17. LIMITATION OF ABSTRACT	18. NUMBER OF PAGES	19a. NAME OF RESPONSIBLE PERSON
a. REPORT	b. ABSTRACT	c. THIS PAGE			STI Help Desk (email: help@sti.nasa.gov)
U	U	U	UU	100	19b. TELEPHONE NUMBER *(Include area code)* (301) 621-0390